Acoustics in burner-stabilised flames

Document Version:
Publisher's PDF, also known as Version of Record (includes final page, issue and volume numbers)

Please check the document version of this publication:

• A submitted manuscript is the version of the article upon submission and before peer-review. There can be important differences between the submitted version and the official published version of record. People interested in the research are advised to contact the author for the final version of the publication, or visit the DOI to the publisher's website.
• The final author version and the galley proof are versions of the publication after peer review.
• The final published version features the final layout of the paper including the volume, issue and page numbers.

Link to publication

Acoustics in

Burner-Stabilised Flames

PROEFSCHRIFT

ter verkrijging van de graad van doctor aan de
Technische Universiteit Eindhoven, op gezag van de
Rector Magnificus, prof.dr. M. Rem, voor een
commissie aangewezen door het College voor
Promoties in het openbaar te verdedigen op
woensdag 29 augustus 2001 om 16.00 uur

door

Ronald Rook

geboren te Groningen

Dit proefschrift is goedgekeurd door de promotoren:

prof.dr. L.P.H. de Goey
en
prof.dr.ir. A.A. van Steenhoven

Contents

Nomenclature

symbol	description	units
$\mathcal{A}$	response mass burning velocity	-
A	surface	m^2
c	speed of sound	m/s
c	concentration	mole/m^3
c_p	specific heat capacity at constant pressure	J/(kg K)
$c_{p,i}$	partial specific heat capacity at constant pressure	J/(kg K)
c_v	specific heat capacity at constant volume	J/(kg K)
d	diameter perforation	m
$D, D_{i\text{m}}$	diffusion coefficients	m^2/s
E	total specific internal energy	J/kg
E	acoustic energy production	W/s
E_a	activation energy	J/mole
e	specific internal energy	J/kg
f	frequency	1/s
$\boldsymbol{g}$	gravitational acceleration	m/s^2
H	total specific enthalpy	J/kg
h	specific enthalpy	J/kg
h_i	partial specific enthalpy	J/kg
J	specific enthalpy	J/kg
K	flame stretch rate	1/s
L_outlet	outlet length	m
$\boldsymbol{n}$	normal vector	-
Q_rel	heat release	J/(m^2s)
Q_bur	heat loss to burner	J/(m^2s)
m	mass burning rate	kg/(m^2s)
$\bar{M}$	mean molar mass	kg/mole
$\mathcal{M}_i$	symbol species i	
M_i	molar mass	kg/mole

p	pitch perforation	m
p	pressure	Pa
p_{atm}	atmospheric pressure	Pa
$\boldsymbol{q}$	heat flux	J/(m^{2}s)
R	gas constant	J/(kg K)
R_{univ}	universal gas constant	J/(mole K)
S	specific surface	m^2/m^3
s	specific entropy	J/(kg K)
s_i	element production rate	mole/(m^{3}s)
s_{L}	burning velocity	m/s
T, T_{g}	gas temperature	K
T_{a}	activation temperature	K
T_{ad}	adiabatic flame temperature	K
T_{iso}	isotherm	K
T_{s}	temperature solid	K
T_{surf}	surface temperature	K
T_{surr}	temperature surroundings	K
t	time coordinate	s
$\boldsymbol{U}_i$	diffusion velocity vector	m/s
$\boldsymbol{u}$	velocity vector	m/s
u_{f}	flame velocity	m/s
$\mathcal{V}$	response outlet velocity	-
W	acoustic energy flux	W
w	width metal strip	m
$\boldsymbol{x}$	spatial coordinate	m
x_{f}	stand-off distance	m
X_i	mole fraction	-
Y_i	mass fraction	-
X_{g}	measure of blockage flame holder	kg/(m^{2}s)
Z	acoustic impedance	kg/(m^{2}s)
Z	effective Zeldovich number	-
Z_{g}	impedance of a flame holder	kg/(m^{2}s)
α	heat transfer coefficient	W/(m^{2}K)
γ	specific heat ratio	-
ΔH	combustion enthalpy	J/kg
δ	flame thickness	m
δ	height difference isotherms	m
δT_{iso}	isotherm distance	m
ϵ	small parameter	-

ρ	density	kg/m^3
ρ_i	partial density	kg/m^3
$\dot{\rho}_i$	reaction rate	kg/(m^{3}s)
Θ	dimensionless activation energy	-
λ	heat conductivity	J/(m s K)
λ	air factor	-
μ	dynamic viscosity	kg/(m s)
ν	kinematic viscosity	m^2/s
ν	stoichiometric coefficient	-
ξ	spatial coordinate	m
$\bar{\bar{\boldsymbol{\tau}}}$	stress tensor	kg/(m s^2)
τ	time coordinate	s
ϕ	fuel equivalence ratio	-
ϕ	porosity	-
ϕ	mass flow rate	kg/(m^{2}s)
ψ	density weighted spatial coordinate	m
ψ_{f}	density weighted stand-off distance	m
ω	frequency	rad/s
Fr	Froude number	-
He	Helmholtz number	-
Le	Lewis number	-
Ma	Mach number	-
Re	Reynolds number	-
Pe	Péclet number	-
Pr	Prandtl number	-
Ze	Zeldovich number	-

Chapter 1

General introduction

This thesis crosses a wide variety of disciplines. Combustion and numerical simulations are explored disciplines and their terminology is well-established. New is the field of acoustics and new concepts are introduced in this thesis. In acoustics, the concepts noise, sound or sound waves, acoustic oscillations or acoustic waves are used arbitrarily. Each concept defines pressure perturbations to a steady state pressure in a gaseous medium. These perturbations propagate at the speed of sound, which is a quantity that depends on the composition of the medium.

Acoustic theories make a distinction between linear and nonlinear acoustics. Linear acoustics deal with small amplitude perturbations so that general flow equations can be linearised. In a stagnant medium these perturbations involve a displacement of fluid particles. To justify a linearisation of the flow equations, the fluid particle displacement should be small compared to the characteristic length scale in the geometry considered. High-frequency waves or waves that travel over long distances are part of nonlinear acoustics.

The geometries are often closed systems and due to reflections, standing waves, or modes, are common. In linear acoustics, these modes are unstable in the case that a source of sound is present in that system. In general, the amplitude of a standing wave is bounded by nonlinear effects, arising from sources and viscous effects that are dependent on the amplitude. In other cases, the propagating waves are distorted in such a way that shock formation may occur.

The framework of this thesis, which is described in the next section, is limited to linear acoustics in a closed geometry, the central-heating boiler, and tries to unravel the problems manufacturers of boilers have to cope with.

1.1   Stability of heating devices

In many practical applications heat is supplied to a gas flow. Examples are rockets, gas turbines, afterburners of jet engines and, present in almost every Dutch house, the central-heating boiler. The stability of these devices has been subject to research for many years,

see Candel [5], Culick [7] and Putnam [42].

Since modern central-heating boilers often are closed systems equipped with fully premixed burners, they are susceptible to self-sustained oscillations that can be observed as humming and whistling noises. It appears that in practical applications the stability of these boilers is determined by a large number of parameters such as, the position of the burner in the duct system, the volume of the heat exchanger, the length of the duct, the load of the burner, etc. Since some of these parameters may vary from installation to installation, it is difficult to suppress instabilities under all circumstances. As a result, manufacturers are often forced to use ad hoc solutions which might be effective in one situation but do not in others.

Although the problem of humming burners is known for many years, its solution is far from easy. Manufacturers are frequently limited by high demands, such as high efficiency, comfort and low emissions. Consequently, there is a higher risk that the design becomes unstable. A few years ago the Gasunie Research and the association of boiler manufactures VFK have started an investigation on the practicability of central-heating boilers. In the framework of these investigations, a number of projects was set up and financed by Novem, Gasunie and EnergyNed/Gastec. The result shows that general applicable solutions are not available. The circumstances in which instabilities occur are depending on both the acoustic behaviour of the boiler system and the influence of the flame working as a heat supplier in that system. Instead of drawing up guidelines for suppressing instabilities, TNO-TPD developed a simulation model to predict the instability of a boiler within certain margins to study the effects of design changes on these instabilities. In these predictions the net production of acoustic energy is determined and a vital part is the quality of the description of the interaction between burner/flame system and the acoustics in the boiler.

The call for an accurate description of this interaction was the reason to launch a project, under the name of 'Center for Noise in Boilers', in which the Eindhoven University of Technology participates. This thesis is a contribution to this project and provides models for an accurate description of the interaction between the burner/flame and acoustics. As a start and introduction to the field, the well-known problem of acoustic instabilities is elaborated further by means of the Rijke tube problem in the next section and the steps which were taken in this thesis are presented in section 1.3.

1.2   Thermoacoustics

The phenomenon of self-sustained oscillation in a heating device belongs to the field of thermoacoustics which deals with the interaction between heat and sound. Thermoacoustics describe how pressure waves can be generated by a fluctuating heat release in an acoustic medium like a gas-mixture. The heat-driven acoustic oscillations can roughly be divided into two main categories, viz. the convection/conduction-driven oscillations and the combustion-driven oscillations.

Well-known examples from the first category are the Sondhauss tube [53] and the Rijke
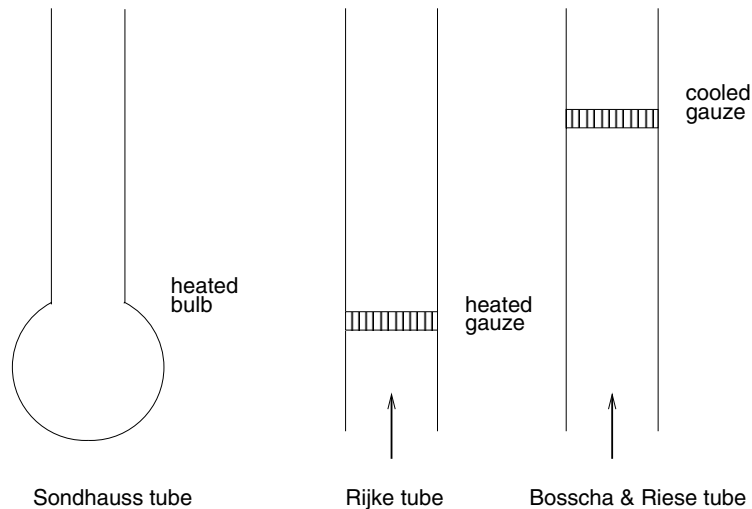
Figure 1.1: Three heat-driven oscillation devices

tube [47] and its 'inverse' the Bosscha & Riese configuration [2] (see figure 1.1). One of the first to describe an example of a combustion-driven oscillation was Higgins [22] who reported the 'singing flame' in 1777. He showed that he could produce sound by placing a hydrogen diffusion flame inside a closed or open-ended tube.

Lord Rayleigh [45] was the first to give an explanation for the development of heat-driven oscillations. Quoted:

> "If heat be periodically communicated to, and abstracted from, a mass of air vibrating (for example) in a cylinder bounded by a piston, the effect produced will depend upon the phase of the vibration at which the transfer takes place. If heat be given to the air at the moment of greatest condensation, or taken from it at the moment of greatest rarefaction, the vibration is encouraged. On the other hand, if heat be given at the moment of greatest expansion, or abstracted at the moment of greatest condensation, the vibration is discouraged."

In other words: acoustic oscillations gain energy when heat is added to a gas at the moment of greatest compression or when heat is extracted from the gas at the moment of greatest expansion. Damping occurs if the heat is removed at the moment of greatest compression or added at the moment of greatest expansion.

In 1954, Putnam & Dennis [43] put Lord Rayleigh's hypothesis for a heat-driven oscillation into a formula. They stated that acoustic energy is produced when the following inequality is satisfied:

$$\int_0^T p'(t)q'(t)\mathrm{d}t > 0, \tag{1.1}$$

where p is the pressure, q the heat release, T denotes the time of one period of a cycle and symbols with $'$ denote the fluctuating quantities.
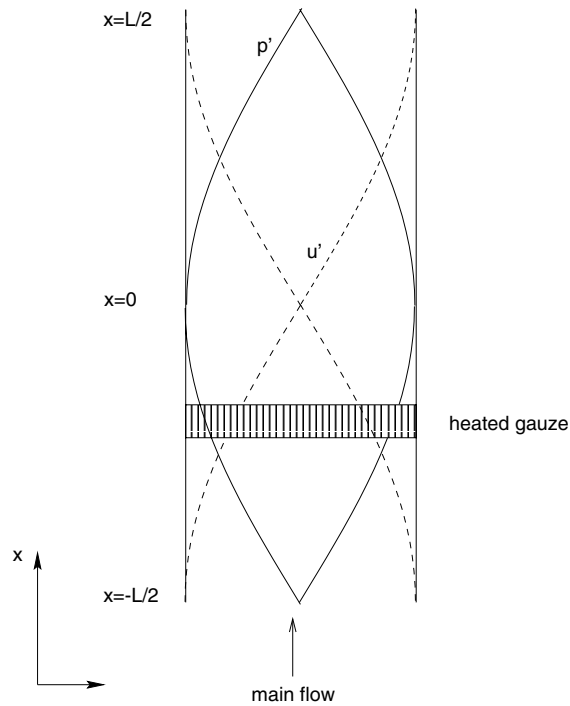
Figure 1.2: Rijke tube of length L with distributions of the pressure p' and the velocity fluctuations u' for the fundamental mode.

To satisfy this inequality, a coupling must exist between the pressure wave and the heat source. If the phase difference between the heat and the pressure oscillations is within ninety degrees, acoustic energy will be produced. A phase difference larger than ninety degrees will cause acoustic damping. In this case the integral equation (1.1) is negative. A difference in phase of exactly ninety degrees results in zero energy gain of the acoustic oscillation, which corresponds to the integral in equation (1.1) being zero.

A clear illustration of the role of the Rayleigh criterion can be given by describing the Rijke tube, which is the classical example to explain the thermoacoustic oscillations.

The Rijke tube is a vertical tube which is open at both ends with a heated gauze placed inside the lower-half of the tube. This heated gauze causes an upward air flow due to free convection. The fundamental mode in the tube has pressure nodes at the tube ends and a pressure anti-node at the centre. Conversely, the velocity wave has a node at the centre and anti-nodes at each end. Higher modes than the fundamental one are not considered. They are weaker because of increased acoustic losses.

Figure 1.2 shows the Rijke tube configuration and the profile of the amplitude of the pressure fluctuations $p'(x,t)$ and the velocity fluctuations $u'(x,t)$ in the tube for the fundamental mode. The difference in phase between the pressure and the velocity waves is exactly ninety degrees, which is determined by the linearised Bernoulli's equation.

The fluctuations in the amount of heat $q'(x,t)$ transferred to the gas by the gauze is proportional to the velocity fluctuations $u'(x,t)$. If the heat transfer would instantaneously
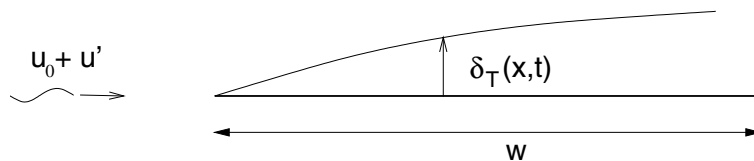
Figure 1.3: Memory effect of the boundary layer near the gauze.

react on the velocity wave, then the heat transfer fluctuations would be ninety degrees out of phase with the pressure wave. According to the Rayleigh criterion (1.1), this phasing would not drive nor damp oscillations.

However, the Rijke tube configuration of Figure 1.2 does effectively produce acoustic energy. The reason is that the heat release follows the velocity with a certain time delay τ. This delay is due to the memory effects of the boundary layer near the gauze which is explained in the following.

In the mean flow direction in the tube, the heated gauze can be viewed upon as strips of metal with width w and temperature T_w. Along the strips viscous and thermal boundary layers will develop. The thickness of the thermal boundary layer is δ_{T} as shown in figure 1.3. We assume that the boundary layers are thin with respect to the length of the strip. For small fluctuations u' of a uniform flow around an average value u_0 the fluctuations in the heat transfer coefficient can be calculated as described by Schlichting [50]. We approximate the velocity and temperature fields by linear profiles in direction normal to the strip. Such an approximation is only valid for low frequencies and small perturbations. Then the heat transfer q at the wall is inversely proportional to the boundary layer thickness: $q \propto 1/\delta_{\mathrm{T}}$. The viscous and thermal boundary layer thickness satisfy the Von Karman equations [50], which are equations found from an integral formulation of the conservation laws using the boundary layer approximation. In this approximation the boundary layers develop starting at the far upstream side of the strip where its fluctuating part δ'_{T} is transported downstream. It can be demonstrated that the perturbations in δ_{T} move along the strip with a velocity $\frac{2}{3}u_0$, which implies that there is a delay of the heat transfer fluctuations q' with respect to perturbations u' of the mean flow. According to the Rayleigh criterion, this time delay might produce acoustic energy, which causes the Rijke tube to be excited at its fundamental frequency.

Figure 1.4 shows the velocity, the pressure and the heat release fluctuations as a function of time at the position of the heated gauze in the lower-half of the Rijke tube. The hatched area in figure 1.4 indicates that the integral in equation (1.1) is positive, corresponding to acoustic energy production.

Note that if the heated gauze is placed in the upper-half of the tube, the thermoacoustic oscillations will be damped instead. The difference is that in the lower-half of the tube the phase of the velocity wave lies ninety degrees ahead of the phase of the pressure wave, whereas in the upper-half of the tube it lies ninety degrees behind. In the upper-half, the delay of the heat release fluctuations on the velocity wave results in the phase shift between the pressure and the heat release fluctuations to be larger than ninety degrees,

Figure 1.4: The velocity u', the pressure p' and the heat release fluctuations q' as a function of time at the position of the heated gauze in the lower-half of the Rijke tube (a), the hatched area represents the contributions to the integral in equation (1.1) (b).
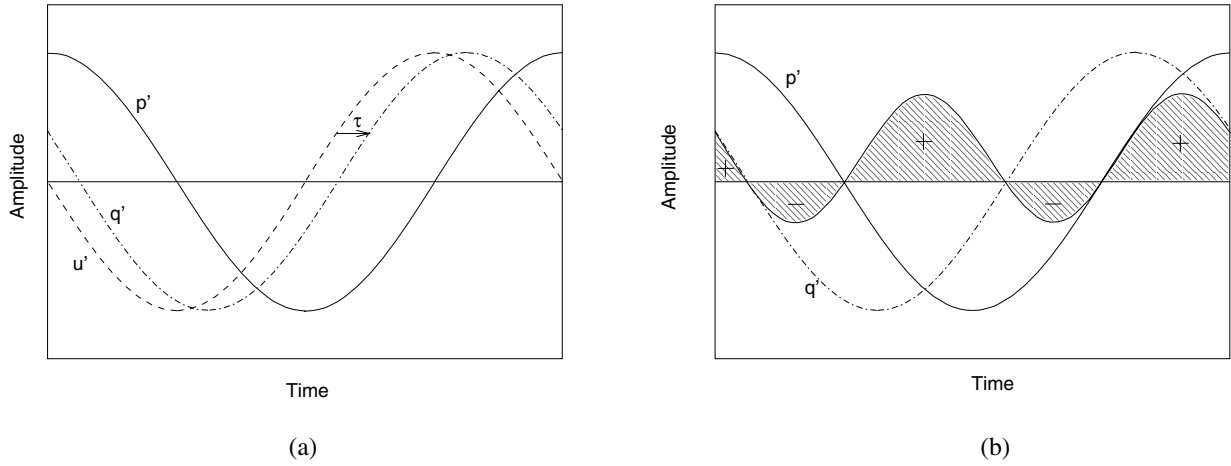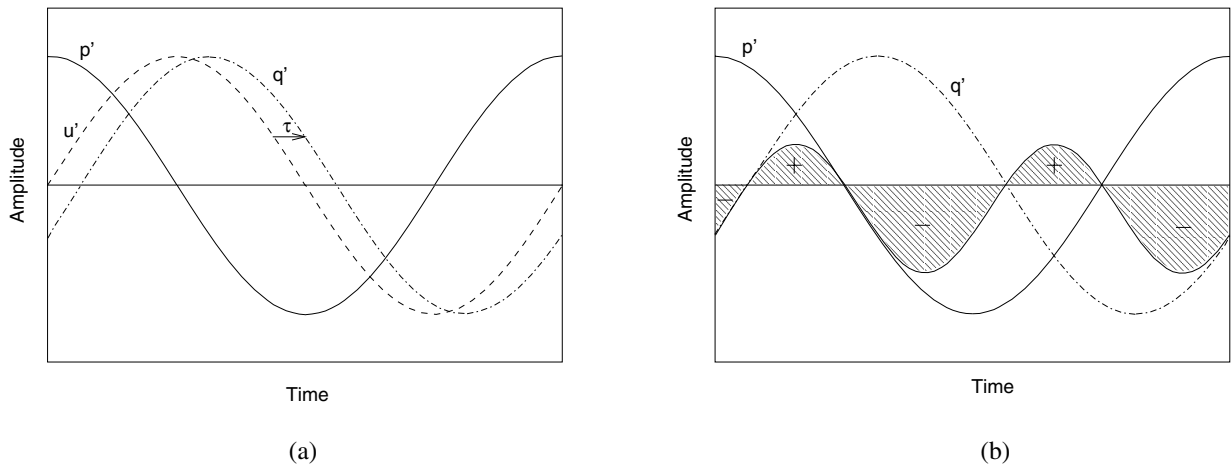

Figure 1.5: The velocity $u'(x, t)$, the pressure $p'(x, t)$ and the heat release fluctuations q' as a function of time at the position of the heated gauze in the upper-half of the Rijke tube (a), the hatched area represents the contributions to the integral in equation (1.1) (b).

which causes acoustic damping. As illustrated in figure 1.5 then a negative integral results in acoustic damping.

The problem investigated in this thesis is one of the second category: the combustion-driven oscillations. To follow the example of the Rijke tube we basically have to look for a similar delay in the response of the heat transfer fluctuation generated by the burner/flame to the velocity fluctuations. The total heat transfer in burner-stabilised flames is the difference in heat released by the reactions occurring in the flame and heat that is lost to the burner. The flame consumes mass at a rate that is in general not equal to the mass flow rate. This mass burning rate is proportional to the temperature of the flame. As in the Rijke tube problem the temperature (or enthalpy) fluctuations and mass flow propagate at different velocities. In cold flows, enthalpy fluctuations travel with the gas velocity which is less than the propagation speed of the mass flow fluctuations (proportional to the speed of sound). Enthalpy fluctuations occur at the burner when the flame moves. These fluctuations propagate towards the flame and result in temperature fluctuations, which cause fluctuations in the mass burning rate. The delay allows us to apply the Rayleigh criterion to the combustion-driven oscillation and predict whether a flame sustains oscillations, like in the Rijke tube problem.

1.3 How to read this thesis

This thesis covers a theoretical and numerical investigation of the acoustic behaviour of one- and two-dimensional burner-stabilised lean methane/air flames placed inside a central-heating boiler. The main objective is to obtain a function that accurately describes the transfer of sound waves by a burner-stabilised flame. This problem is solved by dividing it into sub-problems by using a number of length and time scales. Two length scales can easily be distinguished: an acoustic length scale that measures the distance sound waves travel and the typical length scale of a flame.

The length scale of the flame considered is much smaller than the acoustic length scale, so the speed at which sound waves travel through such small areas can be considered as infinitely high. Therefore, on the flame scales the wave is independent of the spatial coordinates. The frequency of the sound wave is an important time scale. The model for the chemical processes can be simplified by considering the time scale in which the reactions take place. If the sound wave frequency is low enough, the reactions can considered to be quasi-stationary and the very complex chemistry models with many reactions and species can be replaced by reduced chemical models such as one-step chemical models. Note that high frequency waves may violate the infinite speed of sound assumption. This thesis considers low frequency sound waves only, because in practice, problems in central-heating boilers occur at relatively low frequencies, typically $< 10^3$ Hz.

In acoustics, sound waves are low amplitude waves, which allow linearisation of the flow equations. We must carefully use this assumption in the simulations of flame, since chemical processes in a flame are far from linear. Furthermore, the relatively small dimen-
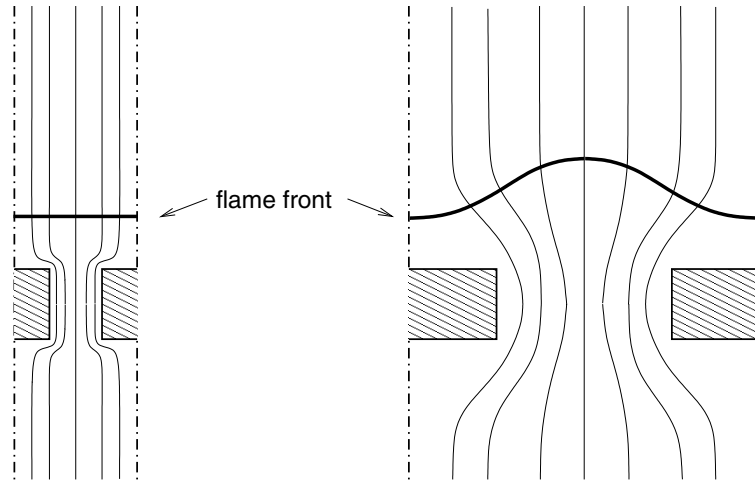
Figure 1.6: Streamlines in flames that are stabilised on a perforated plate. Dash-dotted lines are symmetry lines.

sions in central-heating boiler configurations allow us to model sound waves as plane (one-dimensional) waves.

In central-heating boilers, flames mostly are stabilised on plates, which are porous or perforated with small holes. On a local scale, the flow through these burners is complex (see figure 1.6). However, it has been shown for the steady-state case that if the diameter of the perforations is small enough, the flame itself can be approximated as being one-dimensional [52]. It is expected that this limit is also found in the acoustic response of the so-called surface burners, which are often used in central-heating boilers nowadays. Beside the objective of validating this limiting behaviour, the theory behind the precise form of the response of such flames is investigated. One of the burner configurations that is very close to that one-dimensional limit is the ceramic foam burner [3]. This configuration is used in the theoretical approach as well. In the derived analytical models, another assumption can be made using the large activation energy approximation, so that all reactions take place in an infinitely thin reaction layer. By using these assumptions it is possible to derive an analytical model for the acoustic flame response, which can be used as a transfer function of the burner/flame in the central-heating boiler.

This thesis starts with a detailed model describing the flow and transport equations for reacting flows. This model, which predicts the full linear (acoustic) and nonlinear behaviour of the reacting flow, is discussed in chapter 2. In this chapter, the equations are formulated in case of large waves lengths, relatively to the burner/flame dimensions. From an acoustic point of view, the combustion zone is considered to be a 'black box'. This black box is used to couple the acoustical quantities on both sides of the flame. A useful technique in acoustics, which describes the acoustics of complete systems, is the transfer matrix method. This technique is discussed at the end of chapter 2. Chapter 3 covers the numerical methods that are used to solve the reacting flow equations, describing the acoustics of the burner-stabilised flame. The content of the black box is revealed in a

following numerical and theoretical analysis. In chapter 4 the acoustic behaviour of a pure one-dimensional flame is studied and in chapter 5 the two-dimensional effects of the finite diameter of the holes in a perforated plate burner are studied. Finally, in chapter 6, the results obtained from the theoretical studies on the acoustical behaviour of one-dimensional burners are used for the determination of instabilities in a simplified boiler system.

Notation

This thesis is a numerical as well as a physical investigation, and uses notations from both fields. Vectors (and vector functions) in a physical sense are written in bold-faced type characters (e.g. the velocity vector $\boldsymbol{u}$ and the spatial coordinates $\boldsymbol{x}$). In the numerical investigation the vector notation is used to denote the collection of (vector) variables defined on grid points. These type of vectors are boldfaced and underlined (e.g. $\underline{\boldsymbol{u}}$ for the velocity vector $\boldsymbol{u}$). Note that matrices are normal type characters and (physical) tensors are double over-lined bold characters (e.g. $\bar{\bar{\boldsymbol{\tau}}}$ for the stress tensor).

Chapter 2

Acoustics in a reacting flow

This chapter introduces a model that describes the acoustic behaviour of a system in which a burner-stabilised flame is placed. Two disciplines come into play here. The field of acoustics investigates the linear behaviour of fluctuations in the reacting flow in such a way that the flame is looked upon as a distinct acoustical element in the system. The second discipline is combustion and deals with reactions occurring in the flame. It also provides the starting point for the derivation of a model that describes the details to determine the acoustic behaviour of the flame. The entire flow problem is described by transport equations. Arguments for simplifying the flow equations are given in the next section.

2.1   Introduction

To predict the acoustic behaviour of central-heating boilers, we are allowed to simplify the system on many levels. Each simplification is based on local flow properties in the central-heating boiler.

The first simplification is to consider low-amplitude waves only. In acoustics these waves are described by the linearised transport equations. The assumption of linearity is accurate for the acoustic behaviour in most parts of the system. However, the conversion of fuel in flames is a nonlinear process and is hard to describe by means of linear equations.

In our problem the advantage is that this nonlinear process takes place in a small area only. This advantage enables us to separate the burner/flame from the rest of the system. If an acoustic field is present in the system, the burner/flame area acts as a collection of point sources interacting with this field. Figure 2.1 shows a small source emitting sound waves in a medium. At a distance of a few wavelengths this source acts as a point source. The acoustical size of a source is characterised by the dimensionless Helmholtz number:

$$He = \frac{L}{c_0 \tau}, \tag{2.1}$$

where L is a characteristic length scale, τ is a characteristic time scale and c_0 the ambient speed of sound. In regions where the fluctuating quantities vary over distances L, which
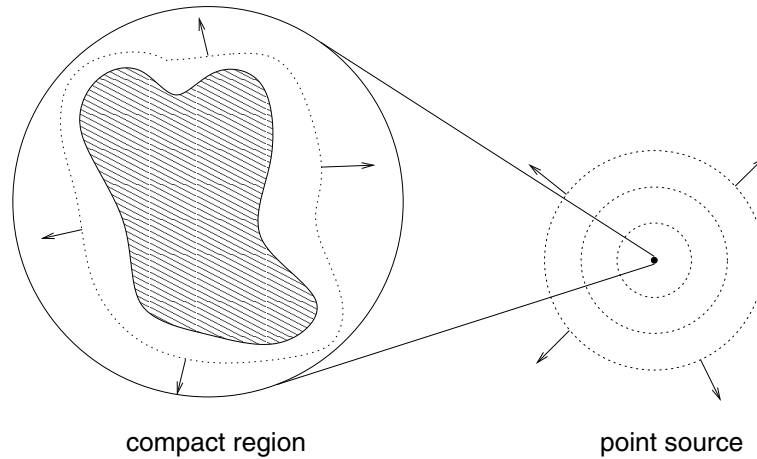
Figure 2.1: Compact region acts as point source in an acoustic field; the dotted lines represent propagating wave fronts.

are small compared to the wave length of the acoustic disturbances, the flow equations can locally be simplified by eliminating the acoustics from those equations. Such a region is called compact. For a more precise definition we distinguish the typical flame time scale $\tau = D/u_0^2$, where D is the diffusion coefficient of the fuel, and the flame length scale $L = D/u_0$ in the burner/flame region. Note that the thickness of the flame scales with L. Using the time and length scales in the burner/flame region the Helmholtz number equals the ambient Mach number Ma. In a compact region we thus have $He = Ma \ll 1$, which allows us to use the low-Mach number approximation of the equations to describe the local behaviour of an acoustic field in a compact region. This approximation is often referred to as the 'incompressible' approximation or Combustion Approximation [4], since pressure variations do not affect the properties of the flame in the compact region.

As chemical reactions take place in the flame, entropy waves will emerge in the burnt gases. However, the Mach number is low enough to assume that entropy fluctuations emerging from the flame are damped out before they reach the boundary of the compact region. This allows us to assume that outside that region isentropic conditions are present in an acoustic field with the fluctuations in the pressure and velocity as its state variables. If this is not true, entropy fluctuations should be included as state variable as well.

Simplifications are made on the level of the geometry of the central-heating boiler. It is assumed that the acoustic field can be described by one-dimensional waves, since in such a (duct) system the cross-flow dimensions are much smaller than the wave lengths present in the acoustic field. This assumption allows us to use the commonly used transfer matrix method to describe the acoustic behaviour of a complete system, using 1D acoustics. The burner/flame is then considered as a transfer function connecting the acoustic fields at both sides of the burner/flame region. This transfer function is often referred to as a 'black box', which owes its name to the fact that it was never modelled accurately. The connection by transfer functions is applied intuitively. Mathematically, it is a leading-order theory (in

Mach number), which is explained in section A.3 of the appendix.

The next sections simplify the general time-dependent reacting flow equations for a burner-stabilised flame, which are described in section 2.2. In section 2.3 the Combustion Approximation is applied on these equations. In section 2.4 the geometric configuration of the burner is discussed. The transfer matrix method is described in section 2.5.

2.2 Reacting gas flows

A chemically reacting gaseous flow system can be described by a set of transport equations, i.e. the convection-diffusion-reaction equations of the chemical components, continuity equation, the enthalpy conservation equation and the Navier-Stokes equations describing the conservation of momentum. This set of equations has to be closed with constitutive relations, such as the gas law. The complete set is presented in section 2.2.1, and in section 2.2.2 the model for the chemistry is discussed.

2.2.1 Transport equations

Consider a reacting gas mixture with N chemical components. Several processes play a role in a chemically reacting gas flow. The unsteady convection/diffusion/reaction equation of species i is [59]:

$$\frac{\partial \rho Y_i}{\partial t} + \boldsymbol{\nabla} \cdot (\rho(\boldsymbol{u} + \boldsymbol{U}_i)Y_i) = \dot{\rho}_i. \tag{2.2}$$

The quantities ρ, Y_i, $\boldsymbol{u}$, $\boldsymbol{U}_i$ and $\dot{\rho}_i$ denote the mass density, the mass fraction of species i, the gas mixture velocity, the diffusion velocity of species i and the chemical source term of species i, respectively.

In most combustion problems each species can be considered to behave as a perfect gas. The partial pressure is then given by:

$$p_i = n_i R_{\text{univ}} T, \tag{2.3}$$

where n_i is the molar density (or concentration) of species i, R_{univ} the universal gas constant and T the temperature of the mixture. According to Dalton's law, the static pressure p is equal to the sum of the partial pressures, which gives:

$$p = \rho \frac{R_{\text{univ}}}{\bar{M}} T, \tag{2.4}$$

where the mean molar mass $\bar{M}$ is defined by:

$$\bar{M} = \left[\sum_{i=1}^{N} \frac{Y_i}{M_i} \right]^{-1}, \tag{2.5}$$

where M_i is the molar mass of species i.

The diffusion of a species is caused by temperature gradients (Soret effect), concentration gradients and pressure gradients. In combustion processes the Soret effect and the diffusion caused by pressure gradients are negligible [1].

The diffusion velocities $\boldsymbol{U}_i$ are described by the Stefan-Maxwell equation [13]. However, the evaluation of this equation is still very complicated. In laminar combustion, the diffusion velocities are approximated by a Fick-like expression:

$$Y_i \boldsymbol{U}_i = -D_{\mathrm{im}} \boldsymbol{\nabla} Y_i, \tag{2.6}$$

with D_{im} the diffusion coefficient for species i in a mixture m. For trace species ($Y_i \approx 0$) this formulation is quite accurate. This assumption of strong dilution is reasonable if the oxidizer is air, because nitrogen is in excess in this case. In addition, the sum of the diffusion fluxes $Y_i \boldsymbol{U}_i$ must be zero. The chemical source term $\dot{\rho}_i$ in the right-hand side of equation (2.2) will be treated in more detail in section 2.2.2 where the reaction chemistry is discussed. Since chemical reactions are mass conserving the following relation must hold:

$$\sum_{i=1}^{N} \dot{\rho}_i = 0. \tag{2.7}$$

Furthermore, the sum of all mass fractions equals one:

$$\sum_{i=1}^{N} Y_i = 1. \tag{2.8}$$

Summation of the N convection/diffusion/reaction equations in (2.2) leads to the overall time dependent mass conservation equation:

$$\frac{\partial \rho}{\partial t} + \boldsymbol{\nabla} \cdot (\rho \boldsymbol{u}) = 0, \tag{2.9}$$

which can be verified easily. The total energy density is given by:

$$E = \frac{1}{2} |\boldsymbol{u}|^2 + e, \qquad e = h - \frac{p}{\rho}, \tag{2.10}$$

where e is the internal energy and the enthalpy h is defined as:

$$h = \sum_{i=1}^{N} h_i Y_i. \tag{2.11}$$

Furthermore, h_i is the specific enthalpy of species i:

$$h_i = h_i^0 + \int_{T^0}^{T} c_{p,i}(\tilde{T}) \mathrm{d}\tilde{T}, \tag{2.12}$$

with h_i^0 being the formation enthalpy of species i at a certain reference temperature T^0. $c_{p,i}$ is the specific heat capacity of species i, which defines the heat capacity at constant pressure as:

$$c_p = \sum_{i=1}^{N} c_{p,i} Y_i. \tag{2.13}$$

The conservation of energy in a reacting flow is described by:

$$\frac{\partial \rho E}{\partial t} + \boldsymbol{\nabla} \cdot (\rho \boldsymbol{u} E) + \boldsymbol{\nabla} \cdot \boldsymbol{q} + \boldsymbol{\nabla} \cdot (\bar{\bar{\boldsymbol{P}}} \cdot \boldsymbol{u}) = \rho \boldsymbol{u} \cdot \boldsymbol{g}, \tag{2.14}$$

where $\boldsymbol{g}$ is the gravitational acceleration, tensor $\bar{\bar{\boldsymbol{P}}} = p\bar{\bar{\boldsymbol{I}}} + \bar{\bar{\boldsymbol{\tau}}}$. In this thesis, the stress tensor $\bar{\bar{\boldsymbol{\tau}}}$ of the mixture is identical to the expression for a single-component Newtonian fluid:

$$\bar{\bar{\boldsymbol{\tau}}} = -\mu \left[(\boldsymbol{\nabla} \otimes \boldsymbol{u}) + (\boldsymbol{\nabla} \otimes \boldsymbol{u})^{\mathrm{T}} \right] + \frac{2}{3} \mu (\boldsymbol{\nabla} \cdot \boldsymbol{u}) \bar{\bar{\boldsymbol{I}}}, \tag{2.15}$$

where μ is the dynamic viscosity of the mixture. In fact, this expression is formally not correct since terms involving the gradients of the diffusion velocity $\boldsymbol{U}_i$, are neglected with respect to those of the average velocity $\boldsymbol{u}$. Otherwise the assumption $\mu_i = Y_i \mu$ with μ_i the dynamic viscosity of species i, has to be posed, to derive equation (2.15) rigorously [4]. It can be shown that (2.15) is accurate for laminar combustion [59].

Heat transport caused by concentration gradients (Dufour effect) and pressure gradients are negligible in combustion processes [23]. In this case the heat flux $\boldsymbol{q}$ is given by:

$$\boldsymbol{q} = -\lambda \boldsymbol{\nabla} T + \rho \sum_{i=1}^{N} h_i Y_i \boldsymbol{U}_i + \boldsymbol{q}_{\mathrm{rad}}, \tag{2.16}$$

where λ is the heat conductivity coefficient. Heat flux due to radiation is neglected ($\boldsymbol{q}_{\mathrm{rad}} = 0$).

Apart from the convection/diffusion/reaction equations of the species and the total energy, the momentum equations or Navier-Stokes equations are needed to describe a reacting flow completely. The conservation of momentum is described by:

$$\frac{\partial \rho \boldsymbol{u}}{\partial t} + \boldsymbol{\nabla} \cdot (\rho \boldsymbol{u} \otimes \boldsymbol{u}) = -\boldsymbol{\nabla} p + \boldsymbol{\nabla} \cdot \bar{\bar{\boldsymbol{\tau}}} + \rho \boldsymbol{g}. \tag{2.17}$$

The system of conservation equations, including the ideal gas law, is closed and describes time dependent reacting flows.

2.2.2   Combustion chemistry

In the previous section, the reacting flow equations are introduced, but the reaction rate for a species i, $\dot{\rho}_i$, in the species equation (2.2) is not specified yet. In hydrocarbon combustion the reactions involve chain reactions, which means that the oxidation of fuel is governed by many elementary reactions. For methane/air mixtures these elementary reactions are reasonably well-known. Detailed chemical models for CH_4 combustion consist of approximately 36 species and 210 reactions [16].

In general, many reactions simultaneously occur in a reacting mixture. Consider a gas mixture with M elementary reversible reactions among N species. A single reversible reaction with index k ranging from 1 to M can then be written as:

$$\sum_{i=1}^{N} \nu'_{i,k} \mathcal{M}_i \rightleftharpoons \sum_{i=1}^{N} \nu''_{i,k} \mathcal{M}_i \tag{2.18}$$

with $\nu'_{i,k}$ and $\nu''_{i,k}$ the stoichiometric coefficients for the reactant and product species i of reaction k, respectively. The symbol for the species i is given by $\mathcal{M}_i$. The variation of concentration of species i, $c_i = \rho Y_i / M_i$, in time due to reaction k is given by [3]:

$$\frac{\partial c_{i,k}}{\partial t} = \left(\nu''_{i,k} - \nu'_{i,k} \right) \left(k_{\mathrm{f},k} \prod_{j=1}^{N} c_j^{\nu'_{j,k}} - k_{\mathrm{b},k} \prod_{j=1}^{N} c_j^{\nu''_{j,k}} \right). \tag{2.19}$$

The reaction rates $k_{\mathrm{f},k}$ and $k_{\mathrm{b},k}$ represent the specific reaction rates of the forward and the backward reactions of reaction k, respectively. The total variation of c_i due to all the reactions is found after summation of relation (2.19) over the M reactions:

$$\dot{\rho}_i = M_i \sum_{k=1}^{M} \frac{\partial c_{i,k}}{\partial t}. \tag{2.20}$$

The specific reaction rates $k_{\mathrm{f},k}$ and $k_{\mathrm{b},k}$ depend on the temperature T and are of the form of the Arrhenius relation:

$$k = A \exp\left(-\frac{E_{\mathrm{a}}}{RT} \right), \tag{2.21}$$

where A is the frequency factor, which may be temperature dependent:

$$A = BT^{\gamma} \quad \text{with} \quad \gamma \in [-1, 2]. \tag{2.22}$$

The reaction rate data (E_{a}, B, γ) for each reaction can be found in the literature [15].

In numerical simulations, using a detailed model for the oxidation of methane, as many as 36 species equations must be solved each time step and together with the evaluation of the source terms, this would be a time-consuming task. Reduction of the number of species and reactions is a remedy.
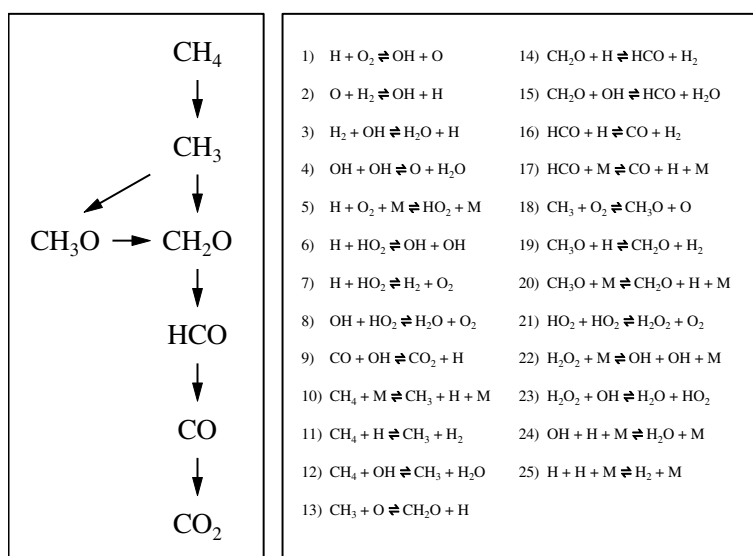
Figure 2.2: C-1 basic reaction chain of lean methane/air oxidation, consisting of 25 reactions among 16 chemical components (N_2 is an inert species).

For the methane/air mixtures considered in this thesis, the equivalence ratio ϕ is defined as:

$$\phi = \frac{2X_{\mathrm{CH_4}}}{X_{\mathrm{O_2}}}, \tag{2.23}$$

where $X_{\mathrm{CH_4}}$, $X_{\mathrm{O_2}}$ the mole fractions in the unburnt mixture. We only consider $\phi < 1$, i.e. lean mixtures.

The C-1 chain, as shown in figure 2.2, can be used to describe the chemistry [15] for these lean mixtures. This so-called skeletal mechanism consists of 25 reversible reactions among 16 chemical components, including inert nitrogen $\mathrm{N_2}$. Methane reacts with oxygen through several intermediate chemical components to $\mathrm{CO_2}$ and $\mathrm{H_2O}$, where radicals, such as O, H and OH, are involved in most of the reaction steps. It is also possible that reactions occur following the C-2 chain and higher hydrocarbons. Especially for fuel-rich mixtures, the latter reaction paths are important.

If only information is required for the global combustion quantities like temperature, burning velocity and concentration profiles of the products, then the chemistry can be simplified even further. A one-step reaction mechanism is sufficient in some cases. An example of a one-step overall reaction mechanism is given by:

$$\mathrm{CH_4 + O_2 \rightarrow CO_2 + 2H_2O}. \tag{2.24}$$

The overall reaction rate $\dot{\rho}_{\mathrm{CH_4}}$ of methane for this reaction can be expressed by [11]:

$$\dot{\rho}_{\mathrm{CH_4}} = -\frac{M_{\mathrm{CH_4}}}{M_{\mathrm{CH_4}}^\alpha M_{\mathrm{O_2}}^\beta} A \rho^p Y_{\mathrm{CH_4}}^\alpha Y_{\mathrm{O_2}}^\beta \exp\left(-\frac{E_{\mathrm{a}}}{RT}\right), \tag{2.25}$$

where the overall reaction order p is equal to $\alpha + \beta$. The overall activation energy E_{a} and the frequency factor A are somehow related to all the intermediate reactions. For the reaction rate (2.25), the unknown coefficients A, α, β and E_{a} can be obtained by experimentally measuring the overall reaction rate of flat methane/air flames under several conditions [57]. Overall reaction mechanisms are used in a number of numerical models of our group to compute methane/air combustion processes [11, 30].

This global reversible reaction mechanism and the skeletal reaction mechanism are used for the combustion chemistry calculations in this thesis, since we restrict our work to lean flames.

2.3   Combustion Approximation

In this section, the governing equations are simplified by using the property that the gas velocity is low compared to the speed of sound (the Mach number is $\mathrm{O}(10^{-4})$). Details of the derivation of the low-Mach number equations can be found in section A.1 of the appendix. The dimensionless pressure is written in a series of the Mach number Ma:

$$p = p_0 + Ma\ p_1 + Ma^2 p_2 + \mathrm{O}(Ma^3), \tag{2.26}$$

where p_i are O(1)-functions. As shown in the analysis in the appendix the leading-order and first-order pressure are functions of time only:

$$p_0 = p_0(t) \quad \text{and} \quad p_1 = p_1(t), \tag{2.27}$$

whereas the second-order pressure $p_2(x, t)$ is determined by the second order Navier-Stokes equations. In dimensionfull form these equations are given by:

$$\frac{\partial \rho \boldsymbol{u}}{\partial t} + \boldsymbol{\nabla} \cdot (\rho \boldsymbol{u} \otimes \boldsymbol{u}) + \boldsymbol{\nabla} p = \boldsymbol{\nabla} \cdot \bar{\bar{\boldsymbol{\tau}}} + \rho \boldsymbol{g}. \tag{2.28}$$

The gas law reads:

$$p_0 = \rho \frac{R_{\text{univ}}}{\bar{M}} T. \tag{2.29}$$

The *dimensionfull* function $p_0(t)$ is determined from the acoustic zone by matching. In this thesis the pressure variations outside the combustion zone are acoustic waves, which are, as shown in section A.2 of the appendix, first-order fluctuations superposed on a constant leading-order pressure. Thus, following the matching principle in section A.3 of the appendix, we have pressures $p_0 =$ constant and $p_1 = p_1(t)$, which does not affect the reacting flow up to a leading-order accuracy. A consequence of the constant leading-order pressure is that this pressure also vanishes from the energy equation (2.14), yielding:

$$\frac{\partial \rho h}{\partial t} + \boldsymbol{\nabla} \cdot (\rho \boldsymbol{u} h) + \boldsymbol{\nabla} \cdot \boldsymbol{q} = 0, \tag{2.30}$$

with $\boldsymbol{q}$ defined by:

$$\boldsymbol{q} = -\lambda \boldsymbol{\nabla} T - \rho \sum_{i=1}^{N} h_i D_{\text{im}} \boldsymbol{\nabla} Y_i. \tag{2.31}$$

The leading-order species equations and mass conservation equation remain unchanged and are given by (2.2) and (2.9). It is important to keep in mind that the solution of the system of equations (2.2), (2.9), (2.28), (2.29), and (2.30) is valid up to leading-order accuracy. This system of equations is used to model the reacting flow in a compact region of the system. The next section describes the configuration of the burner.

2.4 Burner/flame configurations

In laminar premixed combustion, roughly two types of flames can be distinguished: adiabatic flames and burner-stabilised flames. Adiabatic flames have a characteristic mass consumption rate and the corresponding velocity in a quiescent gas is called the adiabatic burning velocity s_{L}. Consider a one-dimensional configuration where gas is flowing from left to right. If the gas velocity is less than the adiabatic burning velocity the flame will
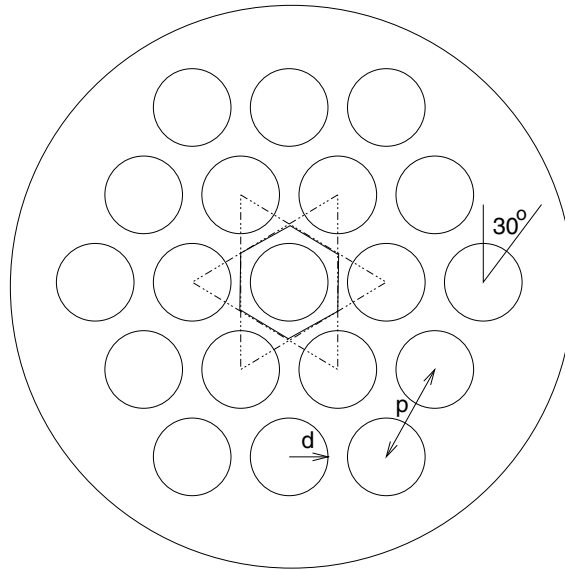
Figure 2.3: Perforated plate configuration.

move to the left. The flame can be prevented from moving to the left by cooling the gas on the upstream side. The burning velocity will adapt until it equals the unburnt mixture velocity. This means that not all heat is added to the gas, because some heat is lost to the burner by cooling.

Materials that suit for cooling are for example a gauze, perforated plate or ceramic foam. By placing those materials in the gas flow, heat is lost to stabilise the flame. In the following, a slit-burner configuration and a one-dimensional configuration are presented, which are used in this thesis.

The perforated plate is a three-dimensional configuration, where the holes are situated in a structured way as shown in figure 2.3. The multi-dimensional reacting flow problem is numerically hard to solve with the current numerical models. Therefore, a two-dimensional multi-slit configuration is introduced here instead. It is believed that this configuration gives a good indication of the local effects in the three-dimensional case.

The configuration of a micro-slit burner is composed of an array of parallel micro-slits, as schematically shown in figure 2.4. The parameters used in the geometry are the thickness t, the pitch p and the diameter d. The ratio $\phi = d/p$ gives the volumetric porosity of the burner plate and is chosen to be equal to the porosity of the three-dimensional perforated plate in figure 2.3. The average flow rate in every micro-slit is therefore equal to the mass flow rate in the corresponding three-dimensional configuration. It may be expected that the qualitative results obtained with the two-dimensional model are valid for the experimental burners of figure 2.3 if the slit thickness is equal to the diameter of the perforation. However, quantitatively, small differences are to be expected.

 Last, but not least, the geometry of a one-dimensional problem is even simpler and easier to solve. It is defined as a special case of the multi-slit burner with very small d, keeping ϕ constant. The flame looses its heat to the solid. In case of a ceramic foam, the flow
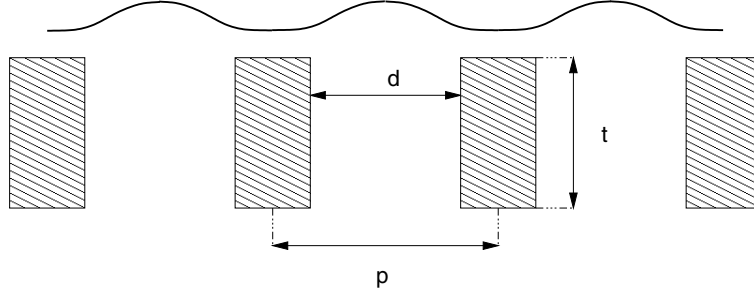
Figure 2.4: Perforated plate with diameter d, pitch p, and thickness t.

inside the burner can be approximated by a two-phase flow, and for each phase convection-diffusion equations are derived to describe this interaction [3]. The gas energy equation is given by:

$$\phi \rho_{\mathrm{g}} c_{p,\mathrm{g}} \frac{\partial T_{\mathrm{g}}}{\partial t} + \phi \rho_{\mathrm{g}} c_{p,\mathrm{g}} \boldsymbol{u} \cdot \boldsymbol{\nabla} T_{\mathrm{g}} - \boldsymbol{\nabla} \cdot (\phi \lambda_{\mathrm{g}} \boldsymbol{\nabla} T_{\mathrm{g}}) = \alpha S (T_{\mathrm{s}} - T_{\mathrm{g}}) - \phi \sum_{i=1}^{N} h_i \dot{\rho}_i, \qquad (2.32)$$

and in a similar way for the solid:

$$(1 - \phi) \rho_{\mathrm{s}} c_{\mathrm{s}} \frac{\partial T_{\mathrm{s}}}{\partial t} - \boldsymbol{\nabla} \cdot ((1 - \phi) \lambda_{\mathrm{s}} \boldsymbol{\nabla} T_{\mathrm{s}}) = -\alpha S (T_{\mathrm{s}} - T_{\mathrm{g}}). \qquad (2.33)$$

Subscripts g and s denote the variables in the gas mixture and material (solid), respectively. α is the heat transfer coefficient between the two phases and S the specific internal surface, where the heat transfer takes place. In this model, all the heat is radiated at the burner surface, where the resulting burner surface temperature is a function of the surface emissivity and the temperature of the surroundings. In the transport equation of the gas phase (2.32), the heat release:

$$Q_{\mathrm{rel}} = \sum_{i=1}^{N} h_i \dot{\rho}_i, \qquad (2.34)$$

is also present, since the flame might stabilise inside the material [3]. Different ways are possible to model the burner. In this thesis, it is assumed that the flame does not stabilise inside the burner, so no heat is released in that region. Furthermore, we use the type of burners where the temperature profiles are solutions of limiting cases of (2.32) and (2.33). It is assumed that the specific heat of the material is infinite $c_{\mathrm{s}} = \infty$. In this case, temperature changes in time of the solid phase inside the burner are not possible: $T_{\mathrm{s}}(\boldsymbol{x}, t) \equiv \bar{T}_{\mathrm{s}}(\boldsymbol{x})$. Another situation is that the heat transfer coefficient α is infinite which implies that the gas temperature equals the temperature of the solid: $T_{\mathrm{g}} = T_{\mathrm{s}} \equiv T$. Hence, equations (2.32) and (2.33) add up to

$$\phi c_p \boldsymbol{u} \cdot \boldsymbol{\nabla} T - \boldsymbol{\nabla} \cdot (\lambda_{\mathrm{m}} \boldsymbol{\nabla} T) = 0, \qquad (2.35)$$
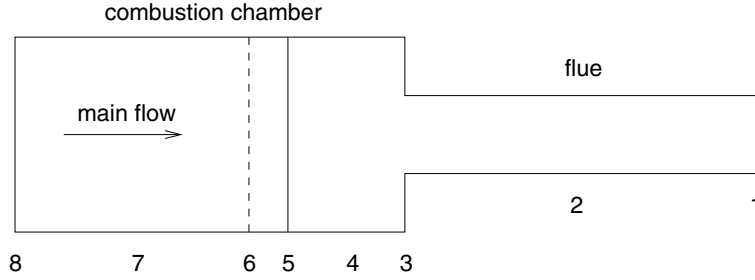
Figure 2.5: Simple configuration of a heating system divided into 8 elements.

where the subscript g is dropped from the specific heat c_p, and $\lambda_{\mathrm{m}} = \phi\lambda_{\mathrm{g}} + (1 - \phi)\lambda_{\mathrm{s}}$. The common definition of ideally-cooled burners is the case that the temperatures of the solid and the gas are equal to the inlet gas temperature: $T_{\mathrm{s}}(\boldsymbol{x}, t) \equiv \bar{T}_{\mathrm{u}}$.

In this thesis two situations are used in the investigation: the ideally-cooled burners with $\lambda_{\mathrm{m}} \to \infty$ and the ceramic foam burners with finite λ_{m}.

2.5   Transfer matrix method

In the previous sections, we presented the governing equations of a (reacting) flow in a compact region. The solution that satisfies the Combustion Approximation is accurate up to leading-order Mach number and analytical or numerical models are used to describe the acoustic behaviour of the burner/flame placed in an acoustic system. In section A.4 the precise form of the transfer matrix of a burner/flame in low-Mach number flows is described.

The propagation of noise by plane waves through an acoustic system can be described using the transfer matrix method (also called the transmission matrix or the four-pole parameter representation [41]). The method is explained by applying it on a simple configuration which is shown in figure 2.5. In this figure a tube with a sudden contraction is shown (element 3), wherein a burner/flame (elements 5 and 6) is placed. This configuration is in fact a very simple model of a central-heating boiler. Adopting pressure fluctuations p' and velocity fluctuations u' as the two state variables forming the acoustic field, the following matrix relation can be written so as to relate state variables on the left (l) and right (r) side of an element i:

$$\left[\begin{array}{c} p'_{\mathrm{l}} \\ u'_{\mathrm{l}} \end{array}\right] = T^i \left[\begin{array}{c} p'_{\mathrm{r}} \\ u'_{\mathrm{r}} \end{array}\right], \tag{2.36}$$

where the transfer matrix for element i is denoted by T^i.

The transfer matrix T of the total system, i.e.

$$T = T^7 T^6 T^5 T^4 T^3 T^2, \tag{2.37}$$

with

$$T = \left[\begin{array}{cc} T_{11} & T_{12} \\ T_{21} & T_{22} \end{array} \right], \tag{2.38}$$

represents the relation between the acoustic fields at both ends of the system, i.e. between $[p_1', u_1']^{\mathrm{T}}$ and $[p_8', u_8']^{\mathrm{T}}$.

The combined transfer matrix of elements 5 and 6 is the most complex one in this system and will be the end product of this thesis. The transfer matrix for the combustion zone is determined by the Combustion Approximation equations as described in the previous section. In the combustion zone we define the acoustic field to be the fluctuations in the leading-order velocity and in the first-order pressure $[p', u']^{\mathrm{T}}$. Since the p' is a function of time only the transfer matrix simply reads:

$$\left[\begin{array}{c} p_1' \\ u_1' \end{array} \right] = \left[\begin{array}{cc} 1 & 0 \\ 0 & \mathcal{V}^{-1} \end{array} \right] \left[\begin{array}{c} p_{\mathrm{r}}' \\ u_{\mathrm{r}}' \end{array} \right], \tag{2.39}$$

where $\mathcal{V}$ represents the matrix element of the velocity fluctuations transfer by the burner/flame region. Analytical expressions are available for the other elements and are given in section A.5 in the appendix.

Knowing the transfer matrices for all elements we can proceed in two ways to determine the instabilities. We distinguish the free system and the driven system. In the free system (figure 2.5) we effectively determine the eigensolutions of the system. These are the acoustic fields which emerge after perturbation of the system in state of rest. The frequencies related to these solutions are the resonance frequencies. In general, these resonance frequencies are complex numbers, representing damped and growing oscillations, i.e. the pressure:

$$p'(t) = \hat{p}(\omega) \exp(\mathrm{i}\omega t) = \hat{p}(\omega) \exp(-\mathrm{Im}(\omega)t) \exp(\mathrm{i}\mathrm{Re}(\omega)t), \tag{2.40}$$

where $\mathrm{Im}(\omega)$ is the damping factor and $\mathrm{Re}(\omega)$ the frequency of oscillation.

If we use the boundary conditions $p_1' = Z_1 u_1'$ and $p_8' = Z_8 u_8'$, where Z_1 and Z_8 are the acoustic impedances, we find

$$\frac{1}{Z_8} = \frac{T_{21}(\omega)Z_1(\omega) + T_{22}(\omega)}{T_{11}(\omega)Z_1(\omega) + T_{12}(\omega)}, \tag{2.41}$$

with T_{ij} defined by (2.37). An eigensolution satisfies the boundary condition $u_8' = 0$, and the corresponding resonance frequencies ω are derived from:

$$T_{21}(\omega)Z_1(\omega) + T_{22}(\omega) = 0. \tag{2.42}$$

The sign of $\mathrm{Im}(\omega)$ determines whether the eigensolution is a damped solution: $p' \rightarrow 0$ or a growing solution: $|p'| \rightarrow \infty$. The eigensolution oscillates with frequency $\mathrm{Re}(\omega)$. In a damping mode the flame produces less acoustic energy than is radiated at the open end. In a growing mode the flame always produces more acoustic energy than the radiated energy,
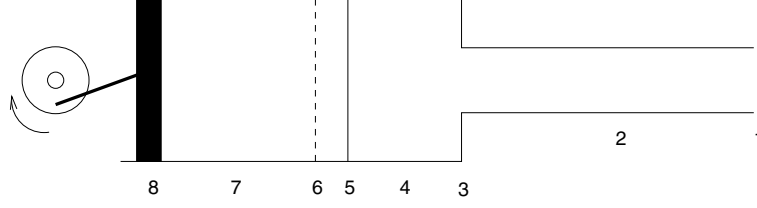
Figure 2.6: Acoustically driven system.

so that the amplitudes of those modes increase.

The second way of investigation is determining the energy production in a driven system. Instead of the condition ($u'_8 = 0$), we prescribe the velocity as shown in figure 2.6. Given u'_8, we determine the pressure p'_8 at the source:

$$p'_8(\omega) = Z_8(\omega)u'_8, \tag{2.43}$$

$$Z_8(\omega) = \frac{T_{11}(\omega)Z_1(\omega) + T_{12}(\omega)}{T_{21}(\omega)Z_1(\omega) + T_{22}(\omega)}. \tag{2.44}$$

The leading-order acoustic power of the source can also be determined, since in a tube the acoustic energy flux W is defined by [41]:

$$W = S\overline{u'p'}, \tag{2.45}$$

in which the bar denotes time-averaging and S the cross sectional area of the tube. Or, evaluated at the source:

$$W(\omega) = S\frac{1}{2}|u'_8|^2\mathrm{Re}(Z_8). \tag{2.46}$$

From equation (2.46), it follows that the source drains energy from the system, if the right-hand side is negative. The source drains energy from the system if the system itself produces acoustic energy. On the other hand, if the system drains energy, the source produces energy It can be shown that the frequencies at which eigensolutions grow are the frequencies at which the flame produces energy. Results of this method, applied to the simplified central-heating boiler, are presented in chapter 6.

Chapter 3

Numerical model

In the previous chapter a model has been introduced for the burner-stabilised flame. This chapter describes the numerical treatment of the transport equations. (2.2), (2.9), (2.28), (2.29), (2.30), and the equation of state (2.29). After a short introduction the computational domain is defined for which boundary conditions are needed. The transport equations, together with the boundary conditions, are approximated on discrete times and places resulting in a set of coupled algebraic equations. These equations are then solved using methods described in the next sections.

3.1 Introduction

Analytical solutions for the transport equations cannot be found, but in such cases a numerical approximation can accurately predict the flow. The solution will be determined in a discrete number of points in space and in time. The error of the discrete solution is measured in terms of the time step and mesh sizes used in the approximation. In a typical two-dimensional flow problem the number of unknowns is quadratically proportional to the inverse of the mesh size. In order to resolve to quick changes of the quantities in the flame, small mesh sizes must be used. To deal with the number of grid points, mesh refinement is applied and the computational domain is limited. If in regions far from the flame the flow does not change, or is known analytically, the domain is limited using the proper boundary conditions. Section 3.2 will discuss the boundary conditions which can be used in a two-dimensional flow geometry. Important is the treatment of the acoustic waves, which should not reflect back on these boundaries. In section 3.3 the discrete approximation of the transport equations is given. The spatial and temporal discretisation is based on the method-of-lines, which treats the space and time dependencies separately. The resulting set of algebraic equations is solved by using the pressure-correction method, which treats the pressure dependence explicitly. The low-Mach number approximation allows us to eliminate the time derivative of the density from the mass conservation equation. The conservation of mass has become a constraint for the flow field. The explicit pressure-correction method corrects the pressure in such a way that mass conservation is satisfied.
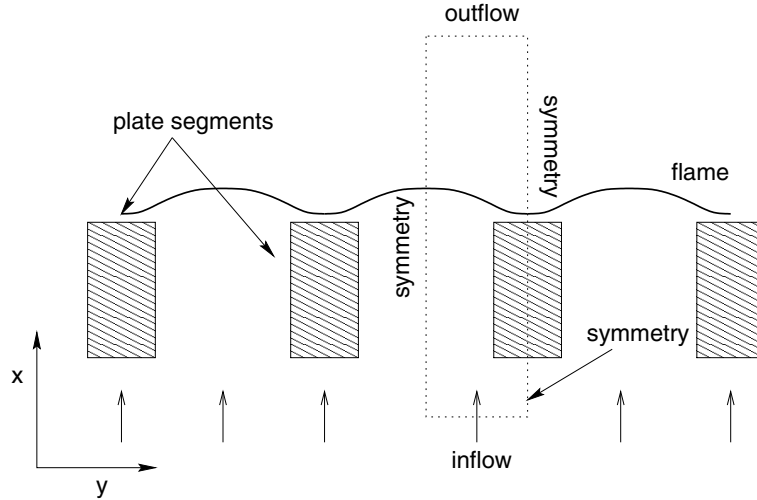
Figure 3.1: The dotted rectangle encloses the computational domain for the multi-slit burner configuration. The vertical dotted lines are symmetry boundaries and the lower and upper dotted lines are the in- and outflow boundaries, respectively.

The complete procedure is described in section 3.4. Section 3.5 validates the numerical approach for one-dimensional flow problems. The one-dimensional shock tube problem or Riemann problem is numerically solved and compared to the analytical solution. The flow in this problem is described by the non-reacting Euler equations, and is compressible, in the sense that the Mach number is not necessarily low. The low-Mach number assumption is validated by comparing the acoustical response of a burner-stabilised one-dimensional flame, described by the full compressible equations and the Combustion Approximation. The linearity in the acoustic behaviour, as is assumed in the transfer matrix method, is tested in section 3.5 as well.

3.2 Boundary conditions

In a multi-slit burner configuration, the computational domain can be limited to a small partition, as shown in figure 3.1. The symmetry axes are situated in the centre of the flow channel and at the centre of each plate segment. In the lower part of the flow, the domain can also be limited using the properties of the flow through a slit. A steady-state flow through that slit is close to a Poiseuille flow, a parabolic velocity profile with a maximum velocity in the centre of the slit and zero at the wall. This velocity profile could be used as a boundary condition if the burner plate is infinitely thick. A quasi-steady approach can be used as boundary condition for the fluctuating parts of the quantities at low frequencies. It can be shown that the acoustic boundary layer is confined to a thickness of $\delta_{\mathrm{A}} = (2\nu/\omega)^{1/2}$ (where $\nu = \mu/\rho$ is the kinematic viscosity of the gas) near the walls. In order to apply this steady-state approach we should have $\delta_{\mathrm{A}}/d > 1$, where d is the diameter of the perforations.
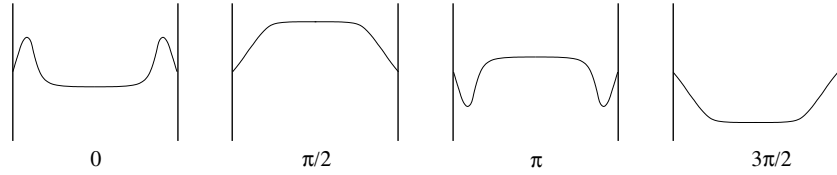
Figure 3.2: Five snap shots of a fluctuating velocity profile in one cycle. Due to inertia, the main flow lags behind the boundary layer.

Hence, the range of frequencies f at which this holds is:

$$f < \frac{\nu}{\pi d^2}. \tag{3.1}$$

For methane/air mixtures $\nu \approx 1.3 \times 10^{-5}$ m^2/s and the diameter of the holes used in this thesis varies between 0.1 mm and 1 mm. This means that the critical frequency ranges from 4 to 400 Hz. Depending on the frequency, the boundary layer is in phase with the pressure fluctuations and the mass flow lags behind due to inertance, as shown in figure 3.2. The exact time dependent boundary conditions are not known. Therefore, a part of the inflow area is modelled as well (see figure 3.1) and homogeneous inflow conditions are imposed.

In the two-dimensional geometry of figure 3.1 the conditions for the flow variables at the walls are the no-slip, no-flux and ideal-cooling conditions:

$$\boldsymbol{u} = 0, \qquad T = T_{\text{wall}}, \qquad \frac{\partial Y_i}{\partial \boldsymbol{n}} = 0, \tag{3.2}$$

where $\boldsymbol{n}$ is the normal vector of the wall.

At the in- and outflow boundaries we have to be careful, because of the presence of propagating waves in the numerical domain. A numerical difficulty arises, when waves are simulated as if there are no inflow and outflow boundaries. Since the burner/flame region is situated in an infinite region, imposing the acoustic open and/or closed end boundary conditions would cause acoustic wave reflections. Hence, standing waves may emerge that dissipate slowly.

A way to circumvent this is to impose non-reflecting boundary conditions. This can be achieved by using the hyperbolic properties of the equations and the assumption that the flow field is homogeneous at the in- and outflow boundaries. These one-dimensional conditions prescribe the incoming 'acoustic' waves and take care of the waves leaving the domain. Hyperbolic differential equations can be rewritten in a set of wave equations, as shown in section B.2 of the appendix. There, the non-reflecting boundaries for the one-dimensional reacting Euler equations are presented.

Formally, in the Combustion Approximation, the speed of sound is infinite and the procedure explained in section B.2 cannot be followed straightforwardly. Some boundaries conditions for the equations in the Combustion Approximation are determined using properties in the acoustic field at low Mach numbers.

In the low-Mach number analysis, diffusive terms appear in the second-order species and

energy equations, and third-order momentum equation only. These terms disappear at the boundaries and we have:

$$\frac{\partial \rho}{\partial t} + \frac{\partial}{\partial x}(\rho u) = 0, \tag{3.3}$$

$$\frac{\partial \rho Y_i}{\partial t} + \frac{\partial}{\partial x}(\rho u Y_i) = 0 \qquad \text{with } i = 1, \cdots, N, \tag{3.4}$$

$$\frac{\partial \rho h}{\partial t} + \frac{\partial}{\partial x}(\rho u h) = 0, \tag{3.5}$$

$$\frac{\partial \rho u}{\partial t} + \frac{\partial}{\partial x}(\rho u u) = -\frac{\partial p}{\partial x} + \rho g, \tag{3.6}$$

which are *consistent* with equations in the acoustic zone up to the first-order species and energy equation, and the second-order momentum equations. This set of differential equation is hyperbolic, if the pressure gradient is fixed.

It is clear that the eigenvalues of the hyperbolic system are all equal to u. This means that near the inflow and outflow, the waves propagate towards the burnt side of the flame. The Riemann invariants belonging to the eigenvalues are the flow variables: ρ, Y_i, u and h, and should be imposed at the inflow:

$$u(0, t) = u_{\text{inflow}}(t), \qquad Y_i(0, t) = Y_{i,\text{inflow}}, \qquad T(0, t) = T_{\text{inflow}}(t). \tag{3.7}$$

The pressure level in the compact zone is determined up to a constant. This level should be fixed on one side of the domain; the average pressure level in one of the acoustic zones:

$$p = \bar{p}_0 \qquad \text{at the downstream boundary}, \tag{3.8}$$

which is the leading-order pressure. The next term is a time-dependent acoustic pressure. Condition (A.52) leads to the consistent boundary condition for the pressure derivative:

$$\frac{\partial p}{\partial x} = 0 \qquad \text{at the inflow boundary}. \tag{3.9}$$

3.3   Method of lines approximation

The flow is described by a set of nonlinear partial differential equations, boundary and initial conditions. These equations are solved by the method of lines, where the solution is obtained for a discrete number of lines $(\boldsymbol{x}_j, t)$ in the $(\boldsymbol{x}, t)$-space. The resulting ordinary differential equations are solved using the Backward Euler time integration.

3.3.1   Spatial discretisation

Many different ways are known to discretise the spatial derivatives. We have chosen to use a finite volume method, because this method is based on approximations of the fluxes, which have a physical meaning. Moreover, this method deals with the integral formulation
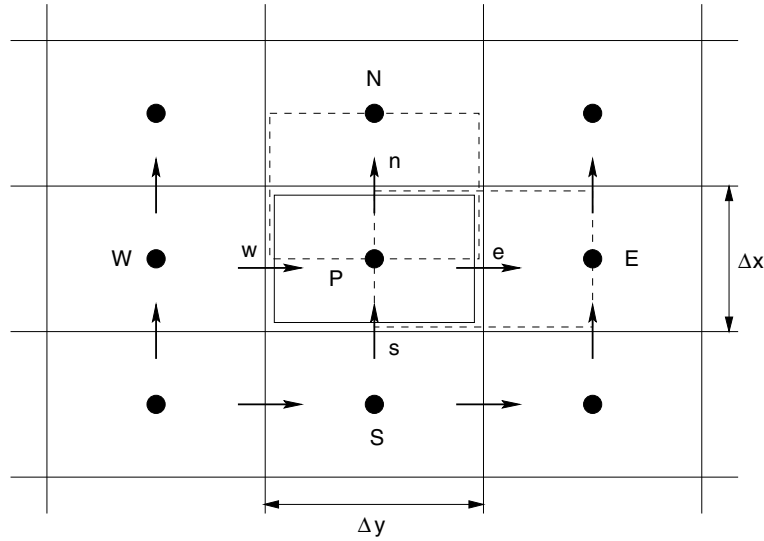
Figure 3.3: A staggered grid configuration. The solid rectangle denotes the cell for the scalar conservation equations. The cells for the momentum equations are dashed.

of a conservation equation. Then, this conservation property is preserved numerically, independent of what kind of discretisation scheme is used. For any sub-domain V we have:

$$\int_V \frac{\partial \phi}{\partial t}\, \mathrm{d}V + \oint_{\delta V} \boldsymbol{f} \cdot \boldsymbol{n}\, \mathrm{d}S - \int_V s(\phi)\, \mathrm{d}V = 0, \tag{3.10}$$

with ϕ a conserved quantity (i.e. $\rho, \rho Y_i, \rho u, ...$), $\boldsymbol{f}$ a combination of convective and diffusive flux terms, and s is a source term.

A finite volume approximation is obtained in the following way: the unknowns are approximated at a specified number of grid points in a staggered way, as shown in figure 3.3. The species mass fractions Y_i, the temperature T and pressure p are defined in the cell centres and the vertical velocity in the middle of the horizontal edges and the horizontal velocity in the middle of the vertical edges. With every grid point, a control volume is associated, in which the conservation equation is approximated. Here, we choose a cell-centred, rectilinear equidistant grid, with midpoint rule approximation for the integrals in equation (3.10). Each grid point P has neighbours, which are labelled as N, E, S and W, for north, east, south and west, respectively. The grid point P is located in the middle of a rectangular control volume and the staggered grid points, which are labelled n, e, s and w, are defined on the faces of the volume. Applying the midpoint rule to all the integrals, we find, after division by $\Delta x \Delta y$:

$$\frac{\partial \phi(\boldsymbol{x}_{\mathrm{P}}, t)}{\partial t} + \frac{F(\boldsymbol{x}_{\mathrm{n}}, t) - F(\boldsymbol{x}_{\mathrm{s}}, t)}{\Delta x} + \frac{G(\boldsymbol{x}_{\mathrm{e}}, t) - G(\boldsymbol{x}_{\mathrm{w}}, t)}{\Delta y} - s(\boldsymbol{x}_{\mathrm{P}})$$
$$= \mathrm{O}(\Delta x^2) + \mathrm{O}(\Delta y^2), \quad (3.11)$$

where the subscripts denote the place at which terms are evaluated. Next, let $\phi_P(t)$ denote the approximation for $\phi(\boldsymbol{x}_P, t)$. The conservation law is now approximated by:

$$\frac{\mathrm{d}\phi_P}{\mathrm{d}t} + \frac{F_n - F_s}{\Delta x} + \frac{G_e - G_w}{\Delta y} = s_P, \tag{3.12}$$

where F_n, F_s, G_e and G_w are the numerical approximations of the fluxes, and $s_P = s(\phi_P)$ is the approximated source term.

The (discrete) fluxes in (3.12) are obtained using an exponential scheme, based on the exact solution of the steady one-dimensional convection-diffusion equation:

$$\frac{\mathrm{d}F}{\mathrm{d}x} = 0, \qquad F(x) = u\phi - D\frac{\mathrm{d}\phi}{\mathrm{d}x}, \tag{3.13}$$

with a constant velocity $u = u_n$ and a constant diffusion coefficient $D = D_n$ locally at the interval (x_P, x_N) (see figure 3.3 for the definition of n, N, and P). The solution to (3.13) is:

$$\phi(x) = \phi_P + \frac{\phi_N - \phi_P}{\exp\left(\frac{u\Delta x}{D}\right) - 1}\left[\exp\left(\frac{u(x - x_P)}{D}\right) - 1\right], \tag{3.14}$$

where $\Delta x = x_N - x_P$. Evaluation of the flux in point n, $F_n = F(x_n)$, gives:

$$F_n = u_n\phi_P - u_n\frac{\phi_N - \phi_P}{\exp\left(\frac{u_n\Delta x}{D_n}\right) - 1}, \tag{3.15}$$

or equivalently,

$$F_n = u_n\frac{1}{2}(\phi_P + \phi_N) - D_n\left(\frac{Pe_n}{\exp(Pe_n) - 1} + \frac{1}{2}Pe_n\right)\frac{\phi_N - \phi_P}{\Delta x}, \tag{3.16}$$

with Pe_n the Péclet number $Pe = u\,\Delta x/D$, evaluated in point n. This is Spalding's scheme and switches smoothly from central-difference for diffusion dominated to upwind for convective dominated flow and has been successfully used in laminar flame computations [11, 52]. See Thiart [54], Ghilani *et al.* [18] and Van 't Hof [58] for more accurate discretisation schemes.

The derivation of the one-dimensional integration scheme is easily extended to two-dimensional problems. The resulting scheme is the sum of two one-dimensional schemes, one in x-direction and the other in y-direction.

3.3.2   Time integration

The set discretised differential equations (3.12) can be generalised to:

$$\frac{\mathrm{d}\underline{\phi}}{\mathrm{d}t} = F(\underline{\phi}), \tag{3.17}$$

for a given function F and $\underline{\phi}$ is the vector of unknowns. An underlined variable is a vector of discrete variables defined in all grid cells together. Reacting flow problems are stiff, because of the small time scales present in the flow. For reasons of stability, when explicit time-integration schemes are used, one has to take the time-step size smaller than or comparable to the smallest physical time scale. Beside the small times scales present in the reaction (especially the production and consumption of radicals, some of which are $O(10^{-9})$ s), we have to deal with the propagation time of sound waves. In air at room temperature the propagation velocity c is 325 m/s. If we have a mesh that has a grid size of, let say, the thickness of the reaction zone, $\Delta x = O(10^{-4})$, then we should take time-step size $\Delta x/c = O(10^{-6})$ s to obtain stability. For low-frequency wave calculations these small time step sizes are unwanted. The Combustion Approximation formally assumes $c \to \infty$, which would result in a zero time-step size.

To circumvent the need for a small time step arising in an explicit integration scheme, we use an implicit time integration scheme, the simplest of which is Backward Euler. It defines the approximate solutions $\underline{\phi}_n$ by:

$$\underline{\phi}_n = \underline{\phi}_{n-1} + \Delta t F(\underline{\phi}_n), \tag{3.18}$$

given a time step Δt and $\underline{\phi}_0$. So, for each time step a large system of nonlinear equations must be solved.

3.4 Solution procedure

Solving a set of discretised one-dimensional differential equations is not fundamentally different from solving a set of two-dimensional equations. However, the one-dimensional case has the advantage that the number of unknowns and equations is in general far less than in the two-dimensional case. Advantages can also be found in the structure of these equations.

Many numerical methods are available to solve the set of discretised differential equations. The best choice is the one that complies with the most important requirements: short computing time and small storage. Also the Combustion Approximation has its contribution to that choice. The set of equations is solved by a pressure correction method, originally developed for the incompressible flow problems. The incompressible methods cannot be adopted straightforwardly, since in combustion large density variations exist. However, the equations in the Combustion Approximation can be rewritten in a form to which an extension of the incompressible pressure correction method can be applied. In low-Mach number flows, the time derivative of the density can be eliminated from the continuity equation. This leads to an equation comparable to the divergence free velocity condition. These constraint equations are preferable to the continuity formulation for stability reasons [58]. The generalised pressure correction method is explained in the next section.

3.4.1   Two-stage pressure correction method

The pressure correction method presented here has close resemblance to the PISO (Pressure Implicit with Splitting Operators) of Issa [25] and is studied in great detail by Van 't Hof [58]. Pressure correction schemes produce an approximation for the solution at a new time level, by consecutive solutions in time. This is done by calculating predictor values for some of the variables first, after which these values are corrected to satisfy the constraint equation by projection.

We apply the two-stage pressure correction scheme [58] to the discretised version of the system of equations (2.2), (2.9), (2.28), (2.29) and (2.30). First, large vectors of unknowns are introduced: $\underline{\phi}$ contains the species and enthalpy defined in each grid cell:

$$\underline{\phi} = \left[\underline{Y}_1^{\mathrm{T}}, \ldots, \underline{Y}_{N-1}^{\mathrm{T}}, \underline{h}^{\mathrm{T}}\right]^{\mathrm{T}}, \tag{3.19}$$

and $\underline{\boldsymbol{u}}$ contains the velocity components defined in each (staggered) grid cell. By using this notation, the discretised equations can be written into a convenient way:

$$\frac{\underline{\phi}^n - \underline{\phi}^{n-1}}{\Delta t} = A_1(\underline{\phi}^n) + A_2(\underline{\phi}^n)\underline{\boldsymbol{u}}^* \tag{3.20}$$

$$\frac{\underline{\boldsymbol{u}}^* - \underline{\boldsymbol{u}}^{n-1}}{\Delta t} = B_1(\underline{\phi}^n, \underline{\boldsymbol{u}}^*) + B_2(\underline{\phi}^n)\underline{p}^{n-1} \tag{3.21}$$

$$\frac{\underline{\boldsymbol{u}}^n - \underline{\boldsymbol{u}}^{n-1}}{\Delta t} = B_1(\underline{\phi}^n, \underline{\boldsymbol{u}}^*) + B_2(\underline{\phi}^n)\underline{p}^n \tag{3.22}$$

$$P_1(\underline{\phi}^n)\underline{\boldsymbol{u}}^n = P_2(\underline{\phi}^n), \tag{3.23}$$

where the subscripts n and $*$ denote consecutive time solutions and a predictor solution, respectively. If $\phi \in \mathbb{R}^{MN}$ (M scalar equations defined in N grid points on a two-dimensional grid), then the image of the nonlinear operators $A_1 : \mathbb{R}^{NM} \to \mathbb{R}^{NM}$, $A_2 : \mathbb{R}^{NM} \to \mathbb{R}^{NM \times 2N}$, $B_1 : \mathbb{R}^{MN \times 2N} \to \mathbb{R}^{2N}$, $B_2 : \mathbb{R}^{MN} \to \mathbb{R}^{2N \times N}$, $P_1 : \mathbb{R}^{MN} \to \mathbb{R}^{N \times 2N}$, and $P_2 : \mathbb{R}^{MN} \to \mathbb{R}^{N}$. Note that equation (3.23) is the discretised constraint equation:

$$\rho \boldsymbol{\nabla} \cdot \boldsymbol{u} = -\frac{\mathrm{D}\rho}{\mathrm{D}t}, \tag{3.24}$$

in which the total derivative on the right-hand side is the expansion rate. As $\rho = \rho(T, Y_1, \ldots, Y_{N-1})$, the time derivatives can be eliminated using the species and energy equations.

Note that a second constraint equation can be derived for the pressure. In the two-stage pressure correction method, this pressure equation is imposed implicitly, which implies that the numerical solution depends on the initial conditions for the pressure. A three-stage pressure correction scheme is presented in [58], which explicitly impose the pressure equation.

The new values $\underline{\phi}^n$, $\underline{\boldsymbol{u}}^n$ and $\underline{p}^n$ defined in (3.20) to (3.23) can be found, because the pressure can be decoupled from the other variables. To do so, we subtract (3.21) from (3.22), which yields the increment equation for the velocity:

$$\underline{\boldsymbol{u}}^n = \underline{\boldsymbol{u}}^* + \Delta t B_2(\underline{\phi}^n)(\underline{p}^n - \underline{p}^{n-1}). \tag{3.25}$$

Next, we combine (3.23) and (3.25) to a Poisson equation:

$$\Delta t P_1(\underline{\phi}^n) B_2(\underline{\phi}^n)(\underline{p}^n - \underline{p}^{n-1}) = P_2(\underline{\phi}^n) - P_1(\underline{\phi}^n)\underline{\boldsymbol{u}}^*. \tag{3.26}$$

The new values $\underline{\phi}^n$, $\underline{\boldsymbol{u}}^n$ and $\underline{p}^n$ can be found in the following two steps, a predictor and corrector step:

1. Calculate $\underline{\phi}^n$ and $\underline{\boldsymbol{u}}^*$ by solving (3.20) and (3.21) in a coupled way.

2. Solve (3.26) for $\underline{p}^n$, and update $\underline{\boldsymbol{u}}^n$ from (3.25).

Equation (3.26) is a linear equation, involving one scalar field only. This equation and the equation for the predictor solution in step 1 can be efficiently solved using standard techniques, of which the one used for our calculations is described in the next section.

3.4.2 Block Gauss-Seidel method

The equations that have to be solved in step 1 in the pressure correction method can be written in a general form:

$$F(\underline{\phi}) = 0. \tag{3.27}$$

We solve this set of nonlinear equations with the well-known Newton method. In this method the sequence of solutions ϕ^k is defined by:

$$\underline{\phi}^{k+1} = \underline{\phi}^k - J^{-1}(\underline{\phi}^k) F(\underline{\phi}^k), \tag{3.28}$$

and a suitable solution $\underline{\phi}^0$, where J is the Jacobi matrix or Jacobian:

$$(J)_{ij} := \left(\frac{\partial F}{\partial \underline{\phi}} \right)_{ij} = \frac{\partial F_i}{\partial \phi_j}. \tag{3.29}$$

The evaluations of the Jacobian can be less computer expensive if the matrix is not updated every Newton step, but, for example, once every time step. This method is called the modified Newton method. Directly inverting the penta-diagonal Jacobian in two-dimensional problems is computationally expensive.
Therefore, an iterative method is proposed. There are many ways known [48]. All classical methods are based on approximations of the Jacobian. Most of these methods are still inefficient because of the dimensions of the Jacobian which must be stored somewhere. The method adopted in our calculations is a so-called matrix-free method, which circumvents the need of large storage. In each grid point the set of equations $F_i(\underline{\phi}^k) = 0$ is solved using the Modified Newton Method, in which the already solved unknowns $\underline{\phi}_j^k$ with $j < i$, are used in the evaluation. This is called the Block Gauss-Seidel method.
This way of solving sets of discretised differential equations may be more efficient when a

time extrapolation method is applied before each new time step to get a better initial guess. However, the gain in computing time is less than mentioned in [58]. The extrapolation method is described in section B.1.3.

If this method does not satisfy the computing time requirements, the calculation of the Jacobian matrices may be more efficient if the Broyden iteration method is used instead of Newton's method. In this method the iteration matrix converges from an initial guess to the correct Jacobian, which is explained in section B.1.1. It result in an decrease in computing time with a factor 2 to 3 [58].

On top of that, a multi-grid solver is implemented. The block Gauss Seidel method is a smoother rather than a solver and after a few smoothing steps the residual hardly decreases. But the residual is quite smooth and this means that a representation of that residual on a coarser grid can be used to obtain a solution on a coarser grid, thus less computing time (another factor 2 decrease, but becomes less useful when coarse grids are used and even counterproductive in combination with the extrapolation method) [58]). The multi-grid method is explained in section B.1.2.

3.4.3 One-dimensional flow problem

Despite the fact that the pressure correction method is applicable to flow problems of arbitrary dimensions, the calculations on the acoustic behaviour of the one-dimensional flame are performed following a slightly different procedure.

In one-dimensional flow problems the variables depend on one spatial coordinate only. In this situation, the pressure correction method is inefficient since only one velocity component is solved. In this case, the momentum equation can be decoupled from the equations and if the pressure distribution is of concern, the momentum equation is integrated. Mass is conserved implicitly by solving the discretised continuity, species and enthalpy equations in a coupled way. Still, Backward Euler is applied as the time integration method, resulting in solving equation (3.18), or the more general equation (3.27), each time step. At this point one can choose to apply an iteration method such as Block Gauss-Seidel, but the structure of the Jacobian allows us to use block-LU decomposition to invert the Jacobian in a direct way, which is a more efficient way to invert a matrix than Block Gauss-Seidel iterations.

This one-dimensional procedure will be tested in section 3.5. The one-dimensional shock-tube problem or Riemann problem is numerically solved and compared to the analytical solution in section 3.5.1. The flow in this problem is non-reacting and compressible, in the sense that it is not a low-Mach number flow. In essence, this problem only validates the time-dependency of the computer program. The low-Mach number assumption is validated by comparing the acoustical responses of a burner-stabilised one-dimensional flame described by the compressible equations and by the Combustion Approximation in section 3.5.2.
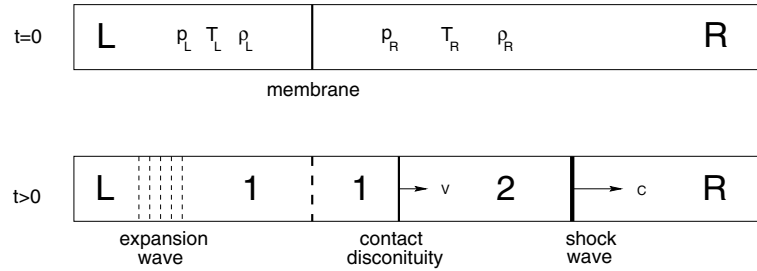
Figure 3.4: In the shock tube two gas states are separated by a membrane (top picture). At $t = 0$ the membrane is removed and an expansion wave, a contact discontinuity and a shock wave form in the tube (bottom figure).

3.5 Numerical validation of the model

Two time-dependent flow problems are used to validate the one-dimensional numerical procedures, such as the discretisation and the method to solve the set of algebraic equations. The first test problem is a shock tube problem of a non-reacting flow, which will be solved using the Euler equations. Even though shocks do not appear in our study on the acoustic behaviour of flames, it is interesting to know whether the numerical model captures shock waves correctly. The results are presented in section 3.5.1. In the transfer matrix method, it is assumed that the flame has a linear response. In section 3.5.2 the influence of the magnitude of the acoustic perturbation on the linearity is investigated. At the same time, the low-Mach number approximation should be correct and this is validated in section 3.5.3. The results are analysed and obtained by assuming specifically a linearity of the burner/flame response. This assumption allows us to determine the response in an efficient way, which is explained in section B.4 of the appendix.

3.5.1 Riemann problem

The shock tube or Riemann problem is an interesting test case, since it has an exact solution to the full set of one-dimensional (non-diffusive) Euler equations. This problem contains a shock wave, a contact discontinuity and an expansion wave.
The flow can be experimentally realised by the sudden removal of a membrane in a long tube separating two initial gas states at different pressure and densities. If viscous effects can be neglected along the tube walls and an infinite tube length is assumed, the exact solution can be obtained on the basis of separate regions of uniform conditions, as shown in the top picture in figure 3.4. At time $t = 0$ the membrane is removed from the tube and a pressure discontinuity propagates to the right, and simultaneously, an expansion wave propagates to the left. In addition, a contact discontinuity separating the two gas regions propagates to the right in the tube. This is illustrated in the bottom part of figure 3.4. Figure 3.5 shows the solution to the problem in space and time.
This solution is constructed using the characteristics (see section B.3) and is compared to the numerically obtained solution on a grid with 1000 points. In this simulation the
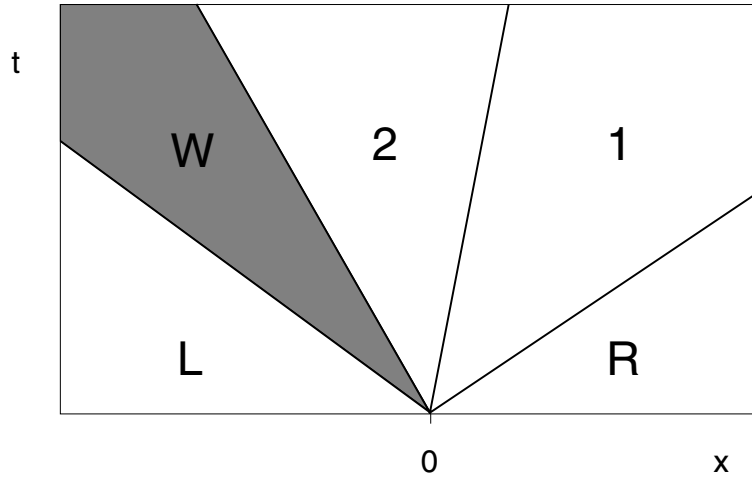
Figure 3.5: Solution in x, t-plane of the Riemann problem, wherein the grey area is the expansion wave.

initial pressure for air at $t < 0$ is $p = p_{\text{atm}}$ on the left side and a factor 10 lower at the right side of the membrane. The initial temperature is 298 K and there is no flow present in the entire tube. The numerical domain is 10 m in length and the membrane is placed at $x = 0$ m. At $t = 6 \times 10^{-3}$ s, a snap shot of the pressure is shown in figure 3.6. The exponential scheme, as presented in section 3.3.1, reduces to a first-order upwind scheme, since the Euler equations does not have diffusive terms. The results show that the model predicts the exact pressure profile well and the position of the shock is correct.

In figure 3.7 the evolution of the temperature profile in time is shown. Here, the non-reflective boundary conditions for an infinitely long tube are tested. The results show that initially, the temperature at the membrane position is not predicted well, but converges to the exact solution as time evolves. The temperature profile at the discontinuity is smoothed by numerical diffusion and hardly any reflection of wave at $x = -4.9$ m is shown in the plot when the expansion wave and the shock wave have passed the boundaries.

The results of the shock tube problem show that the numerical model can accurately predict the positions of discontinuities, but due to artificial diffusion the solution is somewhat smoothened. Also, the non-reflecting boundary conditions perform well.

3.5.2   Linearity

The transfer matrix method is based on a linear theory, and the linearity assumption should be verified before this method can be applied to flows wherein a flame is present. The behaviour of every flame can be linearised provided that the distortions in the flow are small enough. In case of the response of a flame, the amplitude of the upstream velocity fluctuations should be chosen small enough to render a linear response. As the reactions, which take place in the flame, are far from linear, this amplitude could turn out to be very small. This nonlinearity plays an important role in the reaction rates $\dot{\rho}_i$. If we linearise a
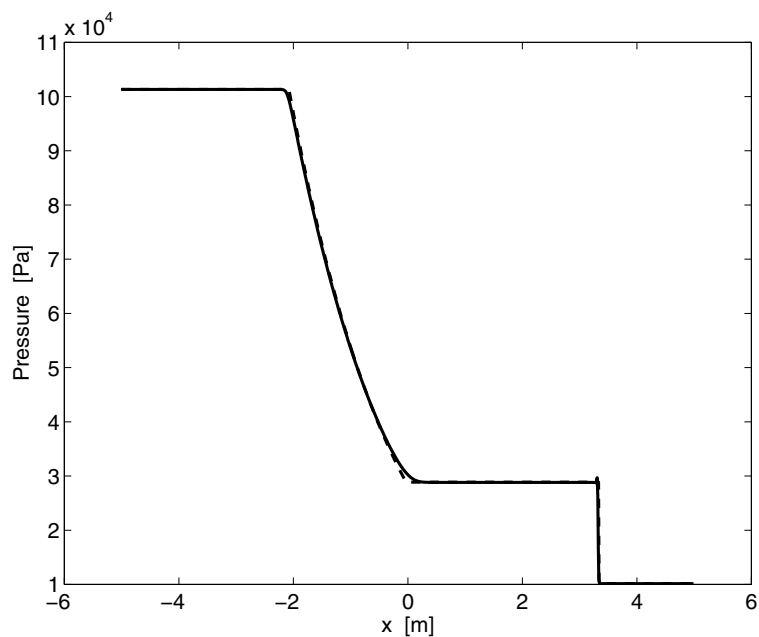
Figure 3.6: Pressure distribution in the tube from the numerical simulation (solid line), compared with the exact solution (dashed line) at $t = 6 \times 10^{-3}$ s.
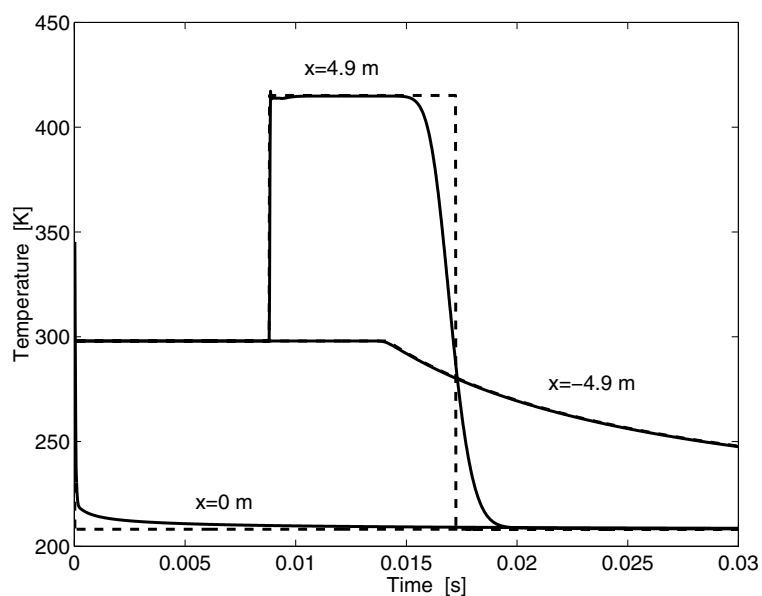

Figure 3.7: Time evolution of the temperature at three fixed points in the tube. Solid line: numerical simulation, dashed line: exact solution.
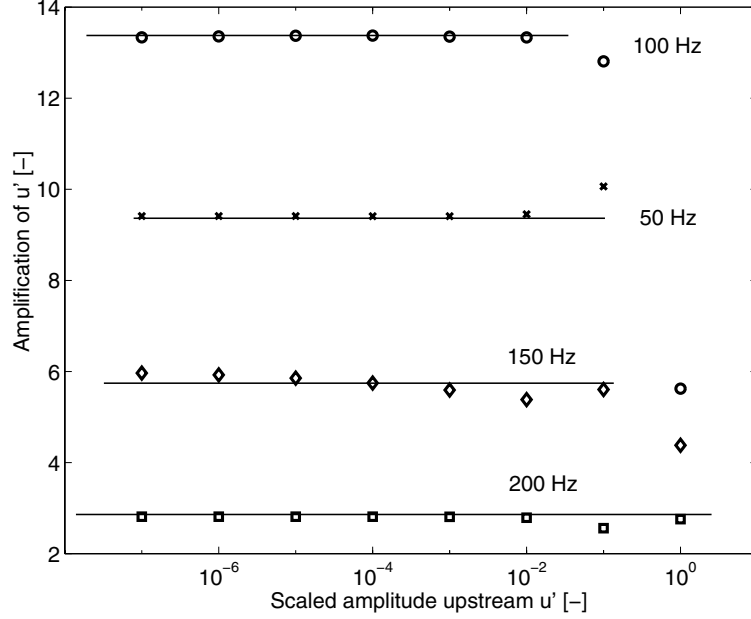
Figure 3.8: The amplification of the upstream velocity fluctuations, as function of the amplitude of the upstream velocity fluctuations divided by the steady upstream velocity, for a flame with $\phi = 0.8$ and $\bar{u}_{\mathrm{u}} = 15$ cm/s and discrete frequencies. Crosses: 50 Hz, circles: 100 Hz, diamonds: 150 Hz, squares: 200 Hz. The thin solid lines denote the average amplifications.

single Arrhenius term (2.21), using a perturbed temperature $T = \bar{T} + \epsilon T'$ with ϵ small, we obtain:

$$k = A \exp(-\Theta) \left(1 - \Theta \epsilon \frac{T'}{\bar{T}} + \frac{\Theta^2 \epsilon^2}{2} \left(\frac{T'}{\bar{T}} \right)^2 \right) + \mathrm{O}(\Theta \epsilon^2), \qquad (3.30)$$

where $\Theta = E_{\mathrm{a}}/(R\bar{T})$. From this expansion, it is clear that the magnitude of $\Theta \epsilon$ determines the linearity of the system. Since the activation energy in most flames is large (in fact, many models assume an infinitely large activation energy), the fluctuating quantities should be chosen small, e.g. $\mathrm{O}(\Theta^{-1})$. In numerical simulations, the amplitude of the perturbations cannot be taken arbitrarily small because of the accuracy of the numerical method and the maximum number of digits of the computer representation. Thus, an amplitude for the upstream velocity fluctuations is chosen in such a way that (1) the response is linear and a sweep is applicable (see section B.4 for an explanation of this type of signal), and (2) the loss of accuracy caused by the number representation of the computer is minimal. Figure 3.8 shows the response of the downstream velocity fluctuations as function of the amplitude of the upstream velocities for several frequencies. The flame is modelled with the low-Mach number approximation and $\phi = 0.8$ and $\bar{u}_{\mathrm{u}} = 15$ cm/s. It shows that the amplitudes can be chosen quite large, up to 10^{-2}. Figure 3.8 shows that an amplitude of 0.1 gives a deviating response for a frequency of 100 Hz. A scaled amplitude of 10^{-5}

is a good choice. Because the figure does not indicate that the response is influenced by the loss of accuracy for even lower amplitudes, we can conclude that such loss of accuracy does not play a role at that choice. The numerically obtained responses, with this value for amplitude of the upstream velocity fluctuations, can be used in the transfer matrix method, safely.

3.5.3 Low-Mach number approximation

Another important assumption made in the modelling is the low-Mach number assumption on which the numerical method is based. One should validate this assumption before using the model in the investigation.

For the purpose of validation we implemented the set of compressible flow equations. For reasons of simplicity, diffusion coefficients, viscosity and reaction rates in the model remain pressure independent. In section B.2.2 of the appendix the boundary conditions are derived, resulting in $N - 1$ wave equations for the species transport, one entropy-wave equation and two wave equations describing sound waves travelling with velocity $u + c$ and $u - c$, respectively.

First, the constant stationary pressure assumption in the low-Mach number approximation is validated. Figure 3.9 shows the relative pressure drop $\Delta p / \bar{p}_0$ over a burner-stabilised flame, with $\phi = 0.8, \bar{T}_{\mathrm{u}} = 300$ K and $\bar{p}_0 = 1$ atm$=101325$ Pa, as function of the stationary upstream velocity. Integration of the momentum equation gives a relation for the pressure drop:

$$\frac{\Delta p}{\bar{p}_0} = -\frac{\bar{M}}{R_{\mathrm{univ}}} \left(\frac{\bar{T}_{\mathrm{b}} - \bar{T}_{\mathrm{u}}}{\bar{T}_{\mathrm{u}}^2} \right) \bar{u}_{\mathrm{u}}^2. \tag{3.31}$$

The flame temperature $\bar{T}_{\mathrm{b}}$ ranges between 1500 K and 2000 K, so the pressure drop is approximately a parabolic function of the upstream velocity. The result shows that the pressure differences are negligible ($\Delta p \ll \bar{p}_0$), indicating that the constant pressure assumption is a valid one.

According to the low-Mach number approximation, the transfer matrix for the flame reduces to an undisturbed pressure transfer and a transfer function $\mathcal{V}$ that is O(1) (see equation (2.39)). In case of a finite Mach number, using the fully compressible version of the model, the four elements are solved by two *independent* simulations of the same flame to obtain two responses of p' and u', on the upstream and downstream sides of the flame. So we have four equations and four unknown elements T_{ij}, which can be solved. These independent simulations are performed by prescribing the incoming sound waves at the far upstream side of the flame in the first simulation and the incoming sound wave at the far downstream side in the second simulation. The boundary conditions on the opposite sides are non-reflecting. Independence could also be achieved by prescribing sound waves on one side in both simulations, but posing an open-end condition in the first simulation and the closed-end condition in the second simulation on the other side. These methods should give equal results. In figures 3.10 to 3.13 the elements of the *inverse* of the transfer function are
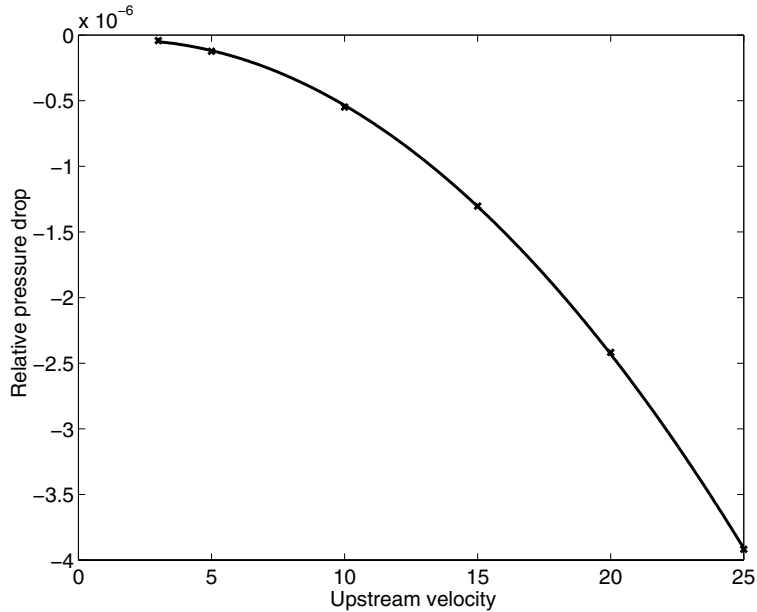
Figure 3.9: The relative stationary pressure drop $\Delta p/\bar{p}_0$ over a one-dimensional methane/air flame as function of the stationary upstream velocity. A parabolic curve is fitted through the data points (cross symbols).

shown for a typical methane/air flame used in this thesis ($\phi = 0.8$, upstream temperature $\bar{T}_\mathrm{u} = 300$ K and one-step chemistry) for different upstream velocities. The off-diagonal elements $(A^{-1})_{12}$ and $(A^{-1})_{21}$ are scaled with the characteristic impedance of the (virtual) tube on the downstream side of the flame: $Z_\mathrm{b} = \bar{\rho}_\mathrm{b}\bar{c}_\mathrm{b}$. Element $(A^{-1})_{11}$ is almost unity and $(A^{-1})_{22}$ is a O(1) function, which is a factor 100 larger than the off-diagonal elements. The wiggles in graphs can be interpreted as the nonlinear effects of the flame. However, the magnitude of the wiggles is negligible. It can be shown that the off-diagonal elements are O(Ma_b) and can be omitted from the transfer matrix in the low-Mach number approximation [24].

In figure 3.14 the transfer function $\mathcal{V}$ is shown comparing the low-Mach number approximation with the simulations with variable pressure for a typical methane/air flame with $\phi = 0.8$ and $\bar{T}_\mathrm{u} = 300$ K. The transfer functions obtained from both models compare very well in the entire frequency domain (maximum 2 percent error), and we conclude that the low-Mach number approximation or Combustion Approximation is also suitable for simulating the acoustic response in lean burner-stabilised methane/air flames.

(a)   (b)

Figure 3.10: The amplitude (a) and phase (b) of element $(A^{-1})_{11}$ in the transfer matrix of a one-dimensional flame with variable pressure. Solid lines: $\bar{u}_{\mathrm{u}} = 10$ cm/s, dashed lines: $\bar{u}_{\mathrm{u}} = 15$ cm/s, and dotted lines $\bar{u}_{\mathrm{u}} = 20$ cm/s.

(a)   (b)

Figure 3.11: The amplitude (a) and phase (b) of element $(A^{-1})_{12}$ in the transfer matrix of a one-dimensional flame with variable pressure. Solid lines: $\bar{u}_{\mathrm{u}} = 10$ cm/s, dashed lines: $\bar{u}_{\mathrm{u}} = 15$ cm/s, and dotted lines $\bar{u}_{\mathrm{u}} = 20$ cm/s.

(a)   (b)

Figure 3.12: The amplitude (a) and phase (b) of element $(A^{-1})_{21}$ in the transfer matrix of a one-dimensional flame with variable pressure. Solid lines: $\bar{u}_{\mathrm{u}} = 10$ cm/s, dashed lines: $\bar{u}_{\mathrm{u}} = 15$ cm/s, and dotted lines $\bar{u}_{\mathrm{u}} = 20$ cm/s.

(a)   (b)
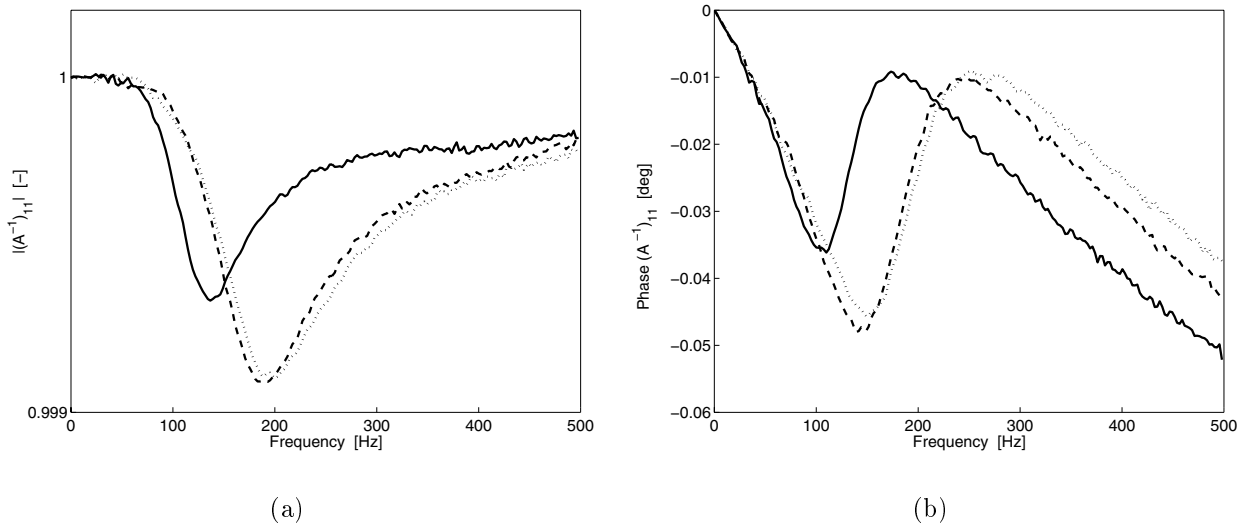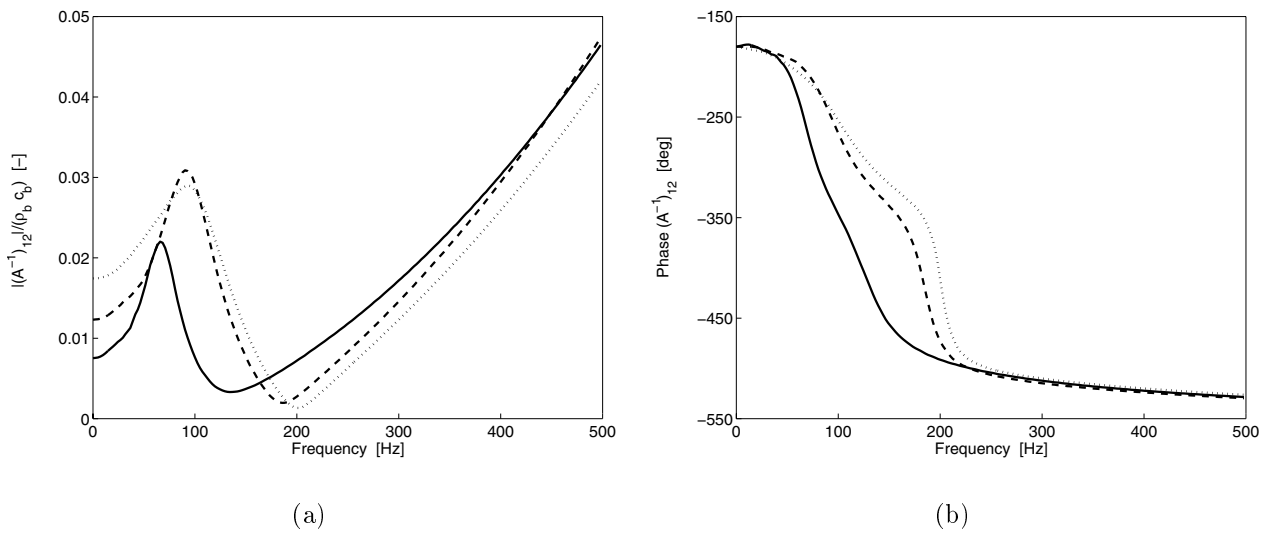
Figure 3.13: The amplitude (a) and phase (b) of element $(A^{-1})_{22}$ in the transfer matrix of a one-dimensional flame with variable pressure. Solid lines: $\bar{u}_{\mathrm{u}} = 10$ cm/s, dashed lines: $\bar{u}_{\mathrm{u}} = 15$ cm/s, and dotted lines $\bar{u}_{\mathrm{u}} = 20$ cm/s.

(a)   (b)
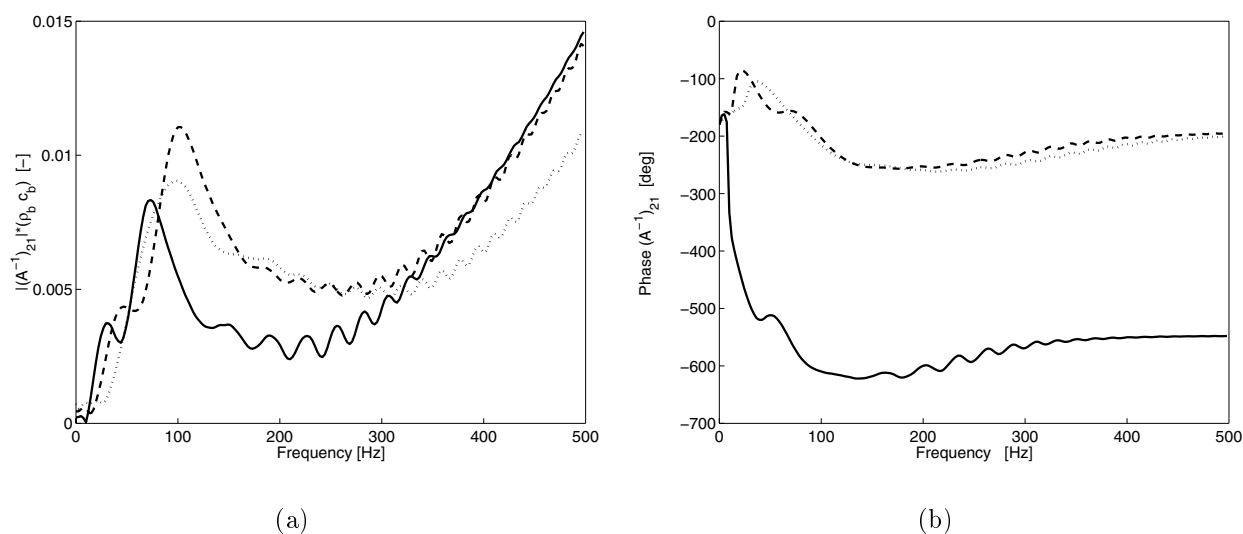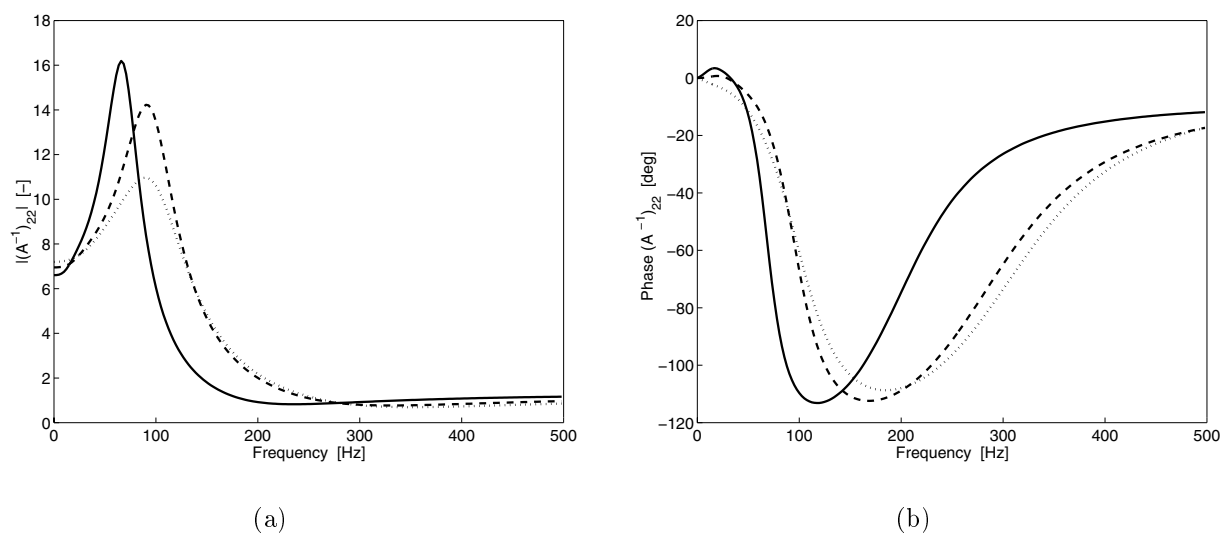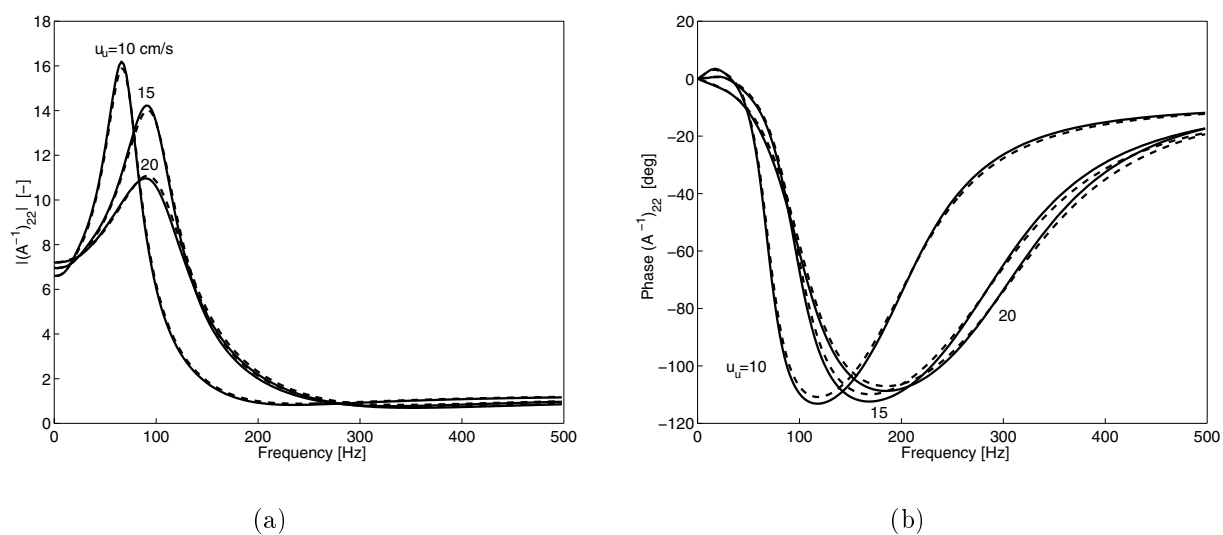
Figure 3.14: The amplitude (a) and phase (b) of element $(A^{-1})_{22}$ for a one-dimensional flame with variable pressure (solid line) and the low-Mach number approximation (dashed line), for three inlet velocities.

Chapter 4

Acoustics in one-dimensional flames

In this chapter, an acoustically perturbed one-dimensional flame is studied analytically and numerically. These perturbations can be imposed externally, but in some cases, the flame oscillates spontaneously. The acoustic behaviour of these flames is described by a set of frequency dependent relations. This set forms the analytical model, which is presented in section 4.2. In section 4.3 experimental results are presented. The results obtained with the analytical and numerical models, and comparison with experiments can be found in section 4.4.

4.1 Introduction

Up to 20 years ago, only phenomenological models were available for predicting the acoustic behaviour of flames. In these models, the heat release of the flame is coupled to the acoustic field (see for example the model of Dowling in section C.1). Depending on the time lag between those quantities, a flame causes resonance in a duct system. In the investigation of the stability of such systems, this time lag is the parameter that characterises the burner. Several of these models are applicable for adiabatic or almost adiabatic flame conditions, in which the response is quite different from that in burner-stabilised flames.

An analytical model has been developed by McIntosh & Clark for burner-stabilised flames. This work actually provides a transfer function $\mathcal{V}$ for the fluctuating velocity (see section C.2). However, the derivation is laborious and the physical picture of the acoustic behaviour cannot be easily understood. For this reason we developed a simple model that makes it possible to understand the physical background of the numerically observed phenomena more easily.

In the next sections, we try to sketch that picture. Important to know in advance is that, in a burner-stabilised flame, there exists a coupling between the heat loss of the flame to the burner and the flame velocity. When the flame moves, the heat loss will change, which influences the temperature of the flame, and consequently, the flame velocity. If this heat loss gives positive feedback to the flame velocity, this might lead to resonance in the flame response. This phenomenon has already been observed in numerical simulations (see figure

3.13) where, for a certain frequency, a resonance peak is present in the amplitude of the responses. For that frequency, the amplitude of the emitted wave is much larger than a steady-temperature increase would normally cause.

In the following simple model, the flame acts as a rigid structure moving with the flame velocity and is described by the so-called G-equation. The coupling between the fluctuating flame position and the mass flow is described in the next section.

4.2   Analytical model

To derive the model, the set of low-Mach number equations is used. These equations are simplified by assuming unit Lewis numbers and it is further assumed that all species have constant and equal specific heats ($c_p = \bar{c}_p$):

$$\frac{\partial \rho Y}{\partial t} + \frac{\partial \rho u Y}{\partial x} - \frac{\partial}{\partial x}\left(\frac{\lambda}{\bar{c}_p}\frac{\partial Y}{\partial x}\right) = \dot{\rho}, \tag{4.1}$$

$$\frac{\partial \rho T}{\partial t} + \frac{\partial \rho u T}{\partial x} - \frac{\partial}{\partial x}\left(\frac{\lambda}{\bar{c}_p}\frac{\partial T}{\partial x}\right) = -\frac{\Delta H}{\bar{c}_p}\dot{\rho}, \tag{4.2}$$

where Y is the mass fraction of methane, $\dot{\rho}$ is the consumption rate of methane, and ΔH is the combustion enthalpy (see section A.6). The source term in equation (4.2) can be eliminated by introducing the enthalpy J:

$$J = \Delta H\, Y + \bar{c}_p T. \tag{4.3}$$

Then, equation (4.2) can be replaced by the enthalpy equation:

$$\frac{\partial \rho J}{\partial t} + \frac{\partial \rho u J}{\partial x} - \frac{\partial}{\partial x}\left(\frac{\lambda}{\bar{c}_p}\frac{\partial J}{\partial x}\right) = 0. \tag{4.4}$$

Furthermore, it is assumed that the activation energy is large enough to reduce the area in which the chemical reactions take place, to one point x_f on the x-axis. So, the term $\dot{\rho}$ is a delta function. Note that this location is time dependent and that $\mathrm{d}x_f/\mathrm{d}t$ defines the local flame velocity u_f.

4.2.1   Extended definition of the mass burning rate

To model the movement of the flame, the recently introduced flamelet concept [10] for laminar flames is adopted. This flamelet model splits the set of one-dimensional species equations into a G-equation, describing the motion of the flame, and a flamelet system, describing the inner-flamelet structure and the mass burning rate. These two parts are coupled by the local flame stretch rate K, which is defined as the fractional rate of change of the mass $M(t)$ contained in an arbitrary volume $V(t)$ in the flame, moving with the flame:

$$\frac{\mathrm{d}M}{\mathrm{d}t} = \int_{V(t)} \rho K\, \mathrm{d}V \qquad \text{with } M(t) = \int_{V(t)} \rho\, \mathrm{d}V, \tag{4.5}$$

which in the limit of infinitely small volume $V(t)$ yields [9]:

$$K = \frac{1}{M}\frac{\mathrm{d}M}{\mathrm{d}t}.$$ (4.6)

The stretch rate, as defined in equation (4.6), is an extension of the usual stretch rate definition [59] and holds for general flames with finite thickness. Flame curvature and flow straining effects are obviously not present in one-dimensional burner-stabilised flames and the sole contribution to the flame stretch rate is related to unsteady flame thickness variations [10], hence:

$$\rho K = -\frac{\partial m}{\partial x},$$ (4.7)

where $m = \rho s_{\mathrm{L}}$ is the local mass burning rate in the flame. This relation shows that the difference between the mass burning rate at the flame front and the burner plate is related to the stretch rate. Equation (4.7) can be integrated from the burner plate at $x = 0$ to obtain the mass burning rate in the entire domain:

$$m(x, t) = m_{\mathrm{u}}(t) - \int_0^x \rho K \mathrm{d}\xi.$$ (4.8)

The motion of Y=constant is described by the G-equation:

$$\rho\frac{\partial Y}{\partial t} + \rho u\,\frac{\partial Y}{\partial x} = m\frac{\partial Y}{\partial x},$$ (4.9)

and the flamelet equation for the inner-flame structure is given by [10]:

$$\frac{\partial}{\partial x}\left(m\,Y\right) - \frac{\partial}{\partial x}\left(\frac{\lambda}{\bar{c}_p}\frac{\partial Y}{\partial x}\right) - \dot{\rho} = -\rho K Y.$$ (4.10)

Note that the full unsteady equation for Y is found when equations (4.7), (4.9) and (4.10) are combined. The model derived in this chapter assumes zero-flame stretch rate $K = 0$, which means that the mass burning rate depends on the time only, or $m(x, t) = m_{\mathrm{u}}(t)$ (see equation (4.8)). Thus, the flame structure behaves as a rigid oscillating structure, without internal dynamics. The assumption of zero stretch is introduced to solve the G-equation for Y analytically. Due to heat loss to the burner, this procedure cannot be followed for the temperature or enthalpy.

From numerical simulations this assumption of zero stretch is verified by determination of the variations in the mass burning rate $m = \rho s_{\mathrm{L}}$ on various locations between burner and flame. The mass burning velocity s_{L} is obtained from $u_{\mathrm{f}} = u - s_{\mathrm{L}}$ as a function of time. The technique used to determine u_{f} can be compared with Particle Image Velocimetry, as used in the experimental determination of velocities in a flow. Solutions on three time steps determine the motion in space, from which the velocity u_{f} is calculated, using a quadratic polynomial fit. This method works well in the regions where the profiles have relatively

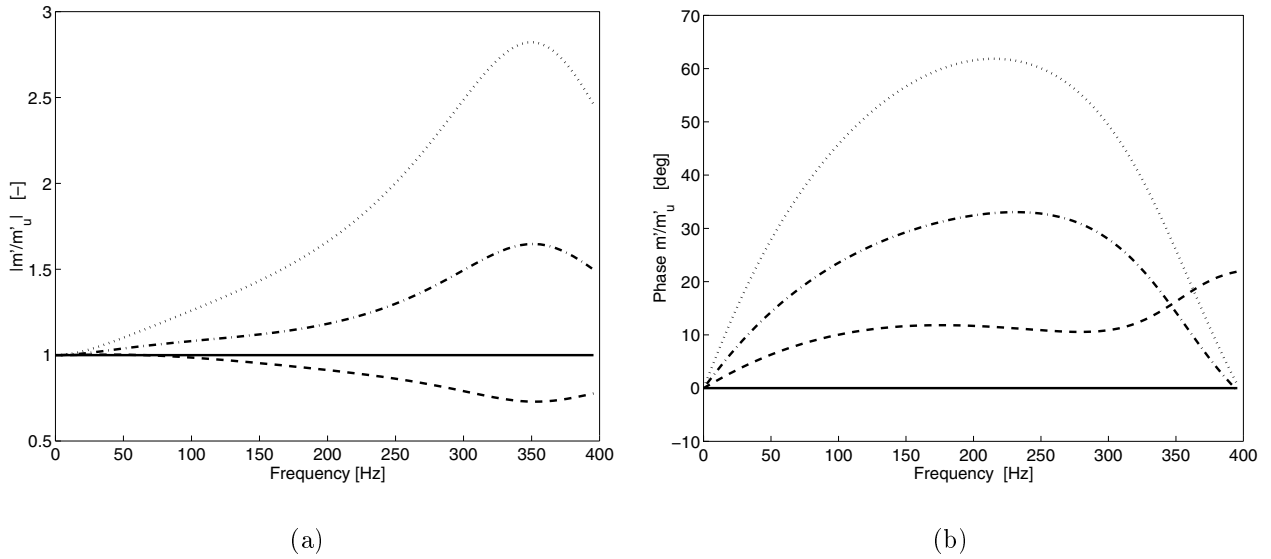(a)   (b)

Figure 4.1: Amplitude (a) and phase (b) of mass burning rate fluctuations as function of the frequency at different locations, normalised by the mass burning rate fluctuations at the burner outlet. Solid line: $x = 0$ mm, dashed line: $x = 0.05$ mm, dash-dotted line: $x = 0.2$ mm, and dotted line $x = 0.5$ mm

large gradients.

In figure 4.1 (a), the numerically obtained amplification of mass burning rate fluctuations is given as function of the frequency at different locations. The result shows that, close to the flame front (stand-off distance is about 0.55 mm for this flame), the mass burning rate response deviates considerably from unity for high frequencies. For these high frequencies, mass burning rate fluctuations propagating towards the burner plate are damped out more easily, which results in an increased amplitude ratio for $|m'(x,t)/m'(0,t)|$. For frequencies around 100 Hz (close to the flame resonance frequency) the maximum amplification of the mass burning rate is about 1.25 in the area between burner and flame.

Figure 4.1 (b) shows that near the flame front the mass burning rate fluctuations are at a maximum 60 degrees ahead. From this result, we conclude that the mass fraction profile shows significant internal deformation for all frequencies, so that the 'rigid-flame' model is not accurate. The influence of the stretch rate K could then be taken into account using weak stretch analysis.

4.2.2   Response of the mass burning rate

In this study, we neglect these influences and assume that $K = 0$. By using the assumption that the mass burning rate is a function of time only, we are able to couple the flame velocity to the fluctuating mass flow at the burner plate. This coupling finally yields three relations that describe the acoustic response of the fluctuating mass burning rate, flame

position, and flame temperature, respectively.

First, the spatial dependency of the density is eliminated from the equations by transformation of (x, t) to the density-weighted coordinates or Von Mises coordinates (ψ, τ):

$$\psi(x, t) = \frac{1}{\bar{\rho}_u} \int_0^x \rho(\xi, t) \, \mathrm{d}\xi \qquad \text{and} \qquad \tau(x, t) = t, \tag{4.11}$$

where the bar denotes the steady part of a quantity. The G-equation (4.9), for $K = 0$, is written in these coordinates as:

$$\bar{\rho}_u \frac{\partial Y}{\partial \tau} + \phi_u(\tau) \frac{\partial Y}{\partial \psi} = m_u(\tau) \frac{\partial Y}{\partial \psi}, \tag{4.12}$$

where $\phi_u(\tau) = \bar{\rho}_u u(0, \tau)$ is the mass flow rate at the burner outlet $\psi = 0$. Since the flame moves as a rigid structure with speed u_f, the density weighted position ψ_f of the flame is related to the mass burning rate as:

$$\bar{\rho}_u \frac{\mathrm{d}\psi_f}{\mathrm{d}\tau} = \phi_u - m_u. \tag{4.13}$$

It is assumed that the thermal conductivity obeys $\rho\lambda = \bar{\rho}_u \bar{\lambda}_u$. This is a plausible assumption, since $\lambda \propto T^{0.7}$ [15]. This assumption simplifies the diffusion terms in the flamelet equation for the inner-flame structure, as well as the enthalpy equation:

$$m_u \frac{\partial Y}{\partial \psi} - \frac{\bar{\lambda}_u}{\bar{c}_p} \frac{\partial^2 Y}{\partial \psi^2} = \frac{\bar{\rho}_u}{\rho} \dot{\rho}, \tag{4.14}$$

and

$$\bar{\rho}_u \frac{\partial J}{\partial \tau} + \phi_u \frac{\partial J}{\partial \psi} - \frac{\bar{\lambda}_u}{\bar{c}_p} \frac{\partial^2 J}{\partial \psi^2} = 0 \qquad \text{for } \psi > 0. \tag{4.15}$$

Equations (4.12), (4.13) (4.14), and (4.15) form the basis for the analytical study. From these relations, we derive the profiles for J and Y. These quantities have a steady part and a fluctuating part, for example, $J = \bar{J} + J'$. All the relations are linearised with respect to the undistorted quantities.

In the steady-state situation, $\bar{m}_u = \bar{\phi}_u$, the flamelet equation (4.14) has an analytical solution $\bar{Y}(\psi)$. At $\psi = \bar{\psi}_f$ all fuel is burnt, or $\bar{Y}(\bar{\psi}_f) = 0$, yielding the steady-state mass fraction profile:

$$\bar{Y}(\psi) = \bar{Y}_u - \bar{Y}_u \exp\left(\frac{\psi - \bar{\psi}_f}{\delta}\right) \qquad \text{for } \psi \leq \bar{\psi}_f, \tag{4.16}$$

and $\bar{Y}(\psi) = 0$ elsewhere, where $\delta = \bar{\lambda}_u/(\bar{\phi}_u \bar{c}_p)$ is the flame thickness.

The steady enthalpy $\bar{J}(\psi) = \bar{J}(0) = \bar{c}_p \bar{T}_b$ for $\psi > 0$. Hence, a relation for the steady stand-off distance can be derived when the steady enthalpy $\bar{J}(\psi)$ is evaluated at the burner outlet, $\psi = 0$:

$$\bar{\psi}_f = \delta \ln\left(\frac{T_{ad} - \bar{T}_u}{T_{ad} - \bar{T}_b}\right), \tag{4.17}$$

where $\Delta H\, \bar{Y}_{\mathrm{u}} + \bar{c}_p \bar{T}_{\mathrm{u}} = \bar{c}_p T_{\mathrm{ad}}$ is used, T_{ad} being the adiabatic flame temperature. For $\psi \leq 0$, the temperature is fixed, so $\bar{J}$ exponentially decreases between $\psi = -\infty$ and $\psi = 0$. The fluctuating part of the enthalpy $J'(\psi, \tau)$ is the solution of the convection-diffusion equation (cf. equation (4.15)):

$$\bar{\rho}_{\mathrm{u}} \frac{\partial J'}{\partial \tau} + \bar{\phi}_{\mathrm{u}} \frac{\partial J'}{\partial \psi} - \frac{\bar{\lambda}_{\mathrm{u}}}{\bar{c}_p} \frac{\partial^2 J'}{\partial \psi^2} = 0 \qquad \text{for } \psi \geq 0. \tag{4.18}$$

The solution of equation (4.12) is given by:

$$Y(\psi, \tau) = \bar{Y}(\psi - \psi'_{\mathrm{f}}(\tau)), \tag{4.19}$$

where $\bar{Y}(\psi)$ is the steady-state solution. Note that (4.19) is a solution of (4.12), but not a solution of the (time-dependent) flamelet equation (4.14). $\psi'_{\mathrm{f}}(\tau)$ is the harmonically fluctuating part of the stand-off distance ψ_{f}:

$$\frac{\psi'_{\mathrm{f}}(\tau)}{\delta} = \frac{\phi'_{\mathrm{u}} - m'_{\mathrm{u}}}{\bar{\phi}_{\mathrm{u}} \hat{\omega}}, \tag{4.20}$$

with $\hat{\omega}$ the complex dimensionless frequency defined by:

$$\hat{\omega} = \frac{\delta}{\bar{u}_{\mathrm{u}}} \omega. \tag{4.21}$$

The harmonic solution of equation (4.18) is given by:

$$J'(\psi) = J'(0) \exp\left(\frac{\psi}{2\delta} (1 - \sqrt{1 + 4\hat{\omega}}) \right), \tag{4.22}$$

where $J'(0)$ is a harmonic function, which is used as a boundary condition for the enthalpy fluctuations. To obtain the exact form of this boundary condition, we use the properties of the temperature at the burner outlet and at the flame position. Substitution of (4.19) in (4.3), the space- and time-dependent enthalpy gives:

$$J(\psi, \tau) = \bar{c}_p T(\psi, \tau) + \Delta H\, \bar{Y}(\psi - \psi'_{\mathrm{f}}). \tag{4.23}$$

From (4.16), the second term reads:

$$\Delta H\, \bar{Y}(\psi - \psi'_{\mathrm{f}}) = \Delta H \left[\bar{Y}_{\mathrm{u}} - \bar{Y}_{\mathrm{u}} \exp\left(\frac{\psi - \bar{\psi}_{\mathrm{f}}}{\delta} \right) \exp\left(-\frac{\psi'_{\mathrm{f}}}{\delta} \right) \right]. \tag{4.24}$$

Using this expression, the enthalpy J linearises to:

$$J(\psi, \tau) = \bar{c}_p T(\psi, \tau) + \Delta H \left[\bar{Y}(\psi) + \bar{Y}_{\mathrm{u}} \exp\left(\frac{\psi - \bar{\psi}_{\mathrm{f}}}{\delta} \right) \frac{\psi'_{\mathrm{f}}}{\delta} \right]. \tag{4.25}$$

At the burner outlet, $\psi = 0$, we obtain the boundary condition for J' as function of the oscillating flame position $\psi'_f(\tau)$:

$$J'(0, \tau) = \Delta H \, \bar{Y}_u \exp\left(-\frac{\bar{\psi}_f}{\delta}\right) \frac{\psi'_f}{\delta}. \tag{4.26}$$

Using equation (4.22), (4.26), and the constant steady enthalpy $\bar{J}$, we derive a harmonic relation for the fluctuating flame temperature T'_b as function of the harmonic flame position ψ'_f:

$$T'_b = (T_{ad} - \bar{T}_u) \exp\left(-\frac{\bar{\psi}_f}{\delta}\right) \exp\left(\frac{\bar{\psi}_f}{2\delta}(1 - \sqrt{1 + 4\hat{\omega}})\right) \frac{\psi'_f}{\delta}. \tag{4.27}$$

The last ingredient is a relation between the flame temperature fluctuations and the mass burning rate. In the steady-state situation, there exists an exponential relation between the flame temperature $\bar{T}_b$ and mass flow rate $\bar{m}_u$ [26]:

$$\bar{m}_u^2 \propto \exp\left(-\frac{T_a}{\bar{T}_b}\right), \tag{4.28}$$

where the activation temperature T_a is related to the Zeldovich number Ze as:

$$T_a = Ze\frac{\bar{T}_b^2}{\bar{T}_b - \bar{T}_u}. \tag{4.29}$$

The linearisation of equation (4.28) yields a quasi-stationary relation. To do so, it is assumed that the flame temperature instantaneously reacts on mass burning rate changes:

$$m'_u = \frac{Ze}{2} \frac{\bar{\phi}_u}{\bar{T}_b - \bar{T}_u} T'_b. \tag{4.30}$$

From equations (4.20), (4.27), and (4.30) the response of the (harmonically) oscillating mass burning rate in a one-dimensional burner-stabilised flame is derived. Elimination of ψ'_f and T'_b from these equations yields:

$$\frac{m'_u}{\phi'_u} = \frac{MN}{MN + \hat{\omega}} \equiv \mathcal{A}(\hat{\omega}), \tag{4.31}$$

with

$$\begin{aligned} M &= \frac{Ze}{2} \frac{1}{\bar{T}_b - \bar{T}_u}, \\ N &= (T_{ad} - \bar{T}_u) \exp\left(-\frac{\bar{\psi}_f}{\delta}\right) \exp\left(\frac{\bar{\psi}_f}{2\delta}(1 - \sqrt{1 + 4\hat{\omega}})\right). \end{aligned} \tag{4.32}$$

In the quasi-steady limit, $\hat{\omega} = 0$, the fluctuating mass burning rate is equal to the fluctuating mass flow, as expected.

4.2.3   Transfer function for the velocity fluctuations

In the previous section, three relations are derived that describe the acoustical behaviour of a one-dimensional burner-stabilised flame, in terms of the response of the mass burning rate as function of the inlet velocity fluctuations. Integration of the energy equation yields the response of the fluctuating velocity in the burnt gases in a straightforward way, as will be shown in this subsection.

The fluctuating energy balance is determined using the energy equation (4.2). Integration from $x = 0$ to $x = \infty$ gives, using $\rho T = \rho_{\mathrm{u}} T_{\mathrm{u}}$:

$$\bar{c}_p(\phi_{\mathrm{b}} T_{\mathrm{b}} - \phi_{\mathrm{u}} T_{\mathrm{u}}) = Q_{\mathrm{rel}} - Q_{\mathrm{bur}}, \tag{4.33}$$

where the energy sources Q_{rel} and Q_{bur} are recognised as the total heat release and heat loss to the burner, respectively. The total heat release is defined as:

$$Q_{\mathrm{rel}} \equiv -\Delta H \int_0^\infty \dot\rho \, \mathrm{d}x, \tag{4.34}$$

provided that all reactions are concentrated at the flame front. The heat loss to the burner is defined as:

$$Q_{\mathrm{bur}} \equiv \lambda(0)\frac{\partial T}{\partial x}\bigg|_{x=0^+}. \tag{4.35}$$

Equation (4.33), by using $\rho_{\mathrm{b}} T_{\mathrm{b}} = \bar\rho_{\mathrm{u}} \bar T_{\mathrm{u}}$, yields the fluctuating energy balance:

$$\bar{c}_p \bar\rho_{\mathrm{u}} \bar T_{\mathrm{u}}(u'_{\mathrm{b}} - u'_{\mathrm{u}}) = Q'_{\mathrm{rel}} - Q'_{\mathrm{bur}}. \tag{4.36}$$

In the following we derive the expressions for Q'_{rel} and Q'_{bur} where we switch back into Von Mises coordinates.

The source term $\dot\rho$ in (4.34) is given by the mass fraction flamelet equation (4.10). Integration of this function from $\psi = 0^+$ to $\psi = \infty$ yields:

$$\Delta H \, m(0) Y(0) - \Delta H \, \frac{\bar\lambda_{\mathrm{u}}}{\bar{c}_p} \, \frac{\partial Y}{\partial \psi}\bigg|_{\psi=0^+} = -\Delta H \int_0^\infty \frac{\bar\rho_{\mathrm{u}}}{\rho}\dot\rho \, \mathrm{d}\psi \, (= Q_{\mathrm{rel}}) . \tag{4.37}$$

Using the solution Y, linearisation of (4.37) results in the following fluctuating heat release:

$$Q'_{\mathrm{rel}} = \bar{c}_p(\bar T_{\mathrm{b}} - \bar T_{\mathrm{u}})m'_{\mathrm{u}}. \tag{4.38}$$

Obtaining the fluctuating part of the heat loss is not straightforward. The enthalpy in the vicinity of the burner outlet ($\psi = 0$) can be recast in a relation for the temperature at the burner outlet. Since we know the enthalpy and the mass fraction solutions, the temperature simply yields the difference of the two:

$$\bar{c}_p T(\psi, \tau) = J(\psi, \tau) - \Delta H \, Y(\psi, \tau), \tag{4.39}$$

where J and Y are given in the section 4.2.2. The spatial derivative of equation (4.39) in $\psi = 0$ is:

$$\bar{c}_p \frac{\partial T}{\partial \psi}\bigg|_{\psi=0^+} = J'(0)\frac{1}{2\delta}(1 - \sqrt{1 + 4\hat{\omega}}) + \Delta H\, \bar{Y}_\mathrm{u} \frac{1}{\delta} \exp\left(-\frac{\bar{\psi}_\mathrm{f} + \psi'_\mathrm{f}}{\delta}\right) \qquad (4.40)$$

with $J'(0)$ given in the previous section by equation (4.26).

By using the relation for $J'(0)$, we linearise the second term of the right hand side of equation (4.40), assuming small ψ'_f. This yields:

$$\frac{\partial T'}{\partial \psi}\bigg|_{\psi=0^+} = -\frac{1}{\delta}(T_\mathrm{ad} - \bar{T}_\mathrm{u}) \exp\left(-\frac{\bar{\psi}_\mathrm{f}}{\delta}\right) \frac{1}{2}\left(1 + \sqrt{1 + 4\hat{\omega}}\right) \frac{\psi'_\mathrm{f}}{\delta}. \qquad (4.41)$$

Using $\delta = \bar{\lambda}_\mathrm{u}/(\bar{\phi}_\mathrm{u}\bar{c}_p)$ and (4.35), the fluctuating part of the heat loss to the burner is found:

$$Q'_\mathrm{bur} = -\bar{c}_p\bar{\phi}_\mathrm{u}(T_\mathrm{ad} - \bar{T}_\mathrm{u}) \exp\left(-\frac{\bar{\psi}_\mathrm{f}}{\delta}\right) \frac{1}{2}\left(1 + \sqrt{1 + 4\hat{\omega}}\right) \frac{\psi'_\mathrm{f}}{\delta}. \qquad (4.42)$$

From equation (4.38) we see that the fluctuating heat release Q'_rel is a function of the fluctuating mass burning rate m'_u and the fluctuating heat loss Q'_bur is a function of the fluctuating flame position ψ'_f. The relations for the responses of these quantities are already derived in the previous sections. Substitution of equations (4.20), (4.27), and (4.30) into the energy balance (4.36), finally gives a relation of the response of the fluctuating velocity at the burnt side and the fluctuating inlet velocity:

$$\frac{u'_\mathrm{b}}{u'_\mathrm{u}} = 1 + \frac{\bar{T}_\mathrm{b} - \bar{T}_\mathrm{u}}{\bar{T}_\mathrm{u}}\mathcal{A}(\hat{\omega}) + \frac{T_\mathrm{ad} - \bar{T}_\mathrm{u}}{\bar{T}_\mathrm{u}} \exp\left(-\frac{\bar{\psi}_\mathrm{f}}{\delta}\right) \frac{1}{2}\left(1 + \sqrt{1 + 4\hat{\omega}}\right) \frac{1 - \mathcal{A}(\hat{\omega})}{\hat{\omega}}. \qquad (4.43)$$

4.2.4 Thermoacoustics in ceramic foam burners

So far, we studied the thermoacoustic behaviour of idealised burners, in the sense that they were assumed to absorb heat from the flame, infinitely fast. The result is that the burner remains at the ambient temperature $\bar{T}_\mathrm{u}$ (the gases that flow through the burner, are also fixed at $T = \bar{T}_\mathrm{u}$ for $x < 0$). In section 2.4 it was explained that in that case the thermal conductivity λ_s of the burner material, as well as the volumetric heat transfer coefficient αS between gas and burner material, are infinite. This situation does not often occur in reality. For that reason, we extend the analysis to ceramic type burners, which have a finite conductivity. This extension yields a temperature change in the burner area, so that the burner surface becomes hot. It is assumed that the heat loss of these burners is dominated by thermal radiation of the burner surface. This means that three burner-material parameters λ_s, ϕ (porosity) and ϵ (surface emissivity) come into play. The volumetric heat transfer coefficient αS and the specific heat c_s are still assumed to be infinite, making an analytical treatment still possible.

With this last assumption, we find that the temperature of the gas and burner material

are equal to a temperature $\bar{T}(x)$, satisfying the leading-order equation found by adding the temperature equations for the gas and solid phases (cf. equations (2.32) and (2.33)):

$$\bar{\phi}_u \bar{c}_p \frac{\mathrm{d}\bar{T}}{\mathrm{d}x} - \lambda_m \frac{\mathrm{d}^2\bar{T}}{\mathrm{d}x^2} = 0, \tag{4.44}$$

where the effective parameter λ_m is constant inside the burner (cf. equation (2.35)). On the downstream side of the burner, only the gas properties play a role and the temperature is described by equation (4.2). The discontinuous change of λ_m, at the interface $x = 0$, leads to a discontinuous derivative of T at $x = 0$. This is related to the fact that the heat exchange between the gas and burner takes place at $x = 0$ with an infinite rate ($\alpha S \to \infty$). The heat at the interface is radiated to the surroundings at this interface. In a steady-state situation, this heat loss is given by [3]:

$$\bar{Q}_{bur} = \bar{\phi}_u \bar{c}_{p,g}(T_{ab} - \bar{T}_b) = \epsilon\sigma(T_{surf}^4 - T_{surr}^4), \tag{4.45}$$

with $T_{surf} = \bar{T}(0)$ the surface temperature and T_{surr} the temperature of the surrounding. For a given mass flow rate $\bar{\phi}_u$ and flame temperature $\bar{T}_b$, T_{surf} is directly found from equation (4.45). The burner is assumed infinitely thick, i.e. the boundary condition is $\bar{T} = \bar{T}_u$ at $x = -\infty$. Because of the high heat capacity of the burner material, the length of the region with considerable temperature gradient is very small compared to the thickness of the burner. Therefore, while solving (4.44) the burner can be assumed infinitely thick, i.e. the boundary condition is $\bar{T} = \bar{T}_u$ at $x = -\infty$. The (stationary) temperature inside the burner is given by:

$$\bar{T}(x) = \bar{T}_u + (T_{surf} - \bar{T}_u)\exp(x/\delta_c), \tag{4.46}$$

with the length scale $\delta_c = \lambda_m/\bar{\phi}_u$. For $\psi > 0$, the temperature increases from T_{surf} to $\bar{T}_b$:

$$\bar{T}(\psi) = [T_{surf}\exp(\bar{\psi}_{f,c}/\delta) - \bar{T}_b + (\bar{T}_b - T_{surf})\exp(\psi/\delta)][\exp(\bar{\psi}_{f,c}/\delta) - 1]^{-1}, \tag{4.47}$$

or

$$\bar{T}(\psi) = (\bar{T}_u - T_{ad} + \bar{T}_b) + (T_{ad} - \bar{T}_u)\exp[(\psi - \bar{\psi}_{f,c})/\delta]. \tag{4.48}$$

The increased surface temperature results in an altered stand-off distance $\bar{\psi}_{f,c}$:

$$\bar{\psi}_{f,c} = \delta\ln\left(\frac{T_{ad} - \bar{T}_u}{T_{ad} - \bar{T}_b + T_{surf} - \bar{T}_u}\right). \tag{4.49}$$

Note that, in case of $T_{surf} = \bar{T}_u$, this expression gives (4.17).

Two questions arise: (1) how does the acoustic velocity change in the burner area due to the fixed exponential temperature profile and (2) are there new ingredients in the acoustic response of the flame, compared with an ideally cooled burner?

The first question has a simply answer: as already indicated, the combination of an infinite heat transfer coefficient and the large specific heat of the burner leads to a temperature

profile inside the burner (equation (4.46)) which remains unchanged by acoustic distortions. So, the gas is accelerated due to a decreasing density, and mass conservation gives the relation between the fluctuations at the burner outlet $x = 0$ and the velocity fluctuations at $x = -\infty$:

$$\frac{u'(0)}{u'_\mathrm{u}} = \frac{\bar{\rho}_\mathrm{u}}{\bar{\rho}(0)} = \frac{T_\mathrm{surf}}{\bar{T}_\mathrm{u}}. \tag{4.50}$$

From here, we follow section 4.2.3. Nothing has changed but the stand-off distance. For unit-Lewis number, we still get for the familiar response of the mass burning rate at the burner outlet:

$$\frac{m'(0)}{\phi'(0)} = \mathcal{A}(\hat{\omega}), \tag{4.51}$$

but now, the stand-off distance is given by (4.49).

At each position inside the burner, the velocities can be obtained by dividing the corresponding flow rates by the local density. In the case of the surface temperature different from the unburnt gas temperature $\bar{T}_\mathrm{u}$, the flame velocity and the fluctuating energy balance (cf. equation (4.36)) read:

$$\bar{\rho}_\mathrm{u}\frac{\mathrm{d}\psi_\mathrm{f}}{\mathrm{d}\tau} = \phi(0) - m(0), \tag{4.52}$$

and

$$\bar{c}_p\bar{\rho}(0)\bar{T}(0)[u'_\mathrm{b} - u'(0)] = Q'_\mathrm{rel} - Q'_\mathrm{bur}, \tag{4.53}$$

where the fluctuating total heat release and heat loss are obtained in the same way as (4.38) and (4.42), respectively. This results in the following response of the fluctuating velocity at the burner outlet:

$$\frac{u'_\mathrm{b}}{u'(0)} = 1 + \frac{\bar{T}_\mathrm{b} - T_\mathrm{surf}}{T_\mathrm{surf}}\mathcal{A}(\hat{\omega})$$
$$+ \frac{T_\mathrm{ad} - \bar{T}_\mathrm{u}}{T_\mathrm{surf}}\exp\left(-\frac{\bar{\psi}_\mathrm{f,c}}{\delta}\right)\frac{1}{2}\left(1 + \sqrt{1 + 4\hat{\omega}}\right)\frac{1 - \mathcal{A}(\hat{\omega})}{\hat{\omega}}. \tag{4.54}$$

This equation, multiplied by the transfer function for the burner (cf. equation (4.50)), gives the complete transfer function which connects the fluctuating velocities at the burnt and unburnt sides:

$$\frac{u'_\mathrm{b}}{u'_\mathrm{u}} = \frac{T_\mathrm{surf}}{\bar{T}_\mathrm{u}} + \frac{\bar{T}_\mathrm{b} - \bar{T}_\mathrm{surf}}{\bar{T}_\mathrm{u}}\mathcal{A}(\hat{\omega})$$
$$+ \frac{T_\mathrm{ad} - \bar{T}_\mathrm{u}}{\bar{T}_\mathrm{u}}\exp\left(-\frac{\bar{\psi}_\mathrm{f,c}}{\delta}\right)\frac{1}{2}\left(1 + \sqrt{1 + 4\hat{\omega}}\right)\frac{1 - \mathcal{A}(\hat{\omega})}{\hat{\omega}}. \tag{4.55}$$

4.2.5 Flame instability

Small random fluctuations are always present, but in general do not lead to instabilities because the fluctuations are damped via the coupling of between the flame motion and the heat loss to the burner. Instability occurs when the amplification is higher than the system is able to damp via enthalpy transport. This happens e.g. in case of large activation energy (rich flames). Small distortions spontaneously grow in time until they are of such a magnitude that they could extinguish the flame. These conditions are far from linear. However, linear theory can predict whether flame modes are unstable or not. This will be studied in this subsection.

For the steady burner-stabilised flame ($\phi'_u = 0$), the flame modes can be determined from the harmonic relations (4.20), (4.27), and (4.30). The fluctuating temperature, mass burning rate and stand-off distance can be eliminated from these equations, resulting in a frequency condition or dispersion equation for the frequency $\hat{\omega}$ of the flame mode, satisfying:

$$\hat{\omega} + MN(\hat{\omega}) = 0, \tag{4.56}$$

where M and N are given by (4.32).

The sign of $\mathrm{Re}(\hat{\omega})$ determines the damping or growth rate of a distortion in the flame. Thus, if it is negative, then the distortion will damp out, otherwise that mode grows and the system becomes unstable. In order to determine the instabilities, we are interested in that frequency at which distortions neither damp nor grow. This is called neutral stability. To obtain those frequencies, we have to solve $\hat{\omega}$ from:

$$a = \mathrm{Re}(-MN(\hat{\omega})), \tag{4.57}$$

$$b = \mathrm{Im}(-MN(\hat{\omega})). \tag{4.58}$$

where $a = \mathrm{Re}(\hat{\omega})$ and $b = \mathrm{Im}(\hat{\omega})$. The real and imaginary part of $-MN(\hat{\omega})$ can be found by looking at the quadratic polynomial $p(c)$:

$$p(c) \equiv c^2 + c - (a + ib). \tag{4.59}$$

A root of this polynomial is given by:

$$c = -\frac{1}{2}\left(1 - \sqrt{1 + 4(a + ib)}\right). \tag{4.60}$$

Using this root and (4.32) gives:

$$MN(\hat{\omega}) = Z \exp\left(-\frac{\bar{\psi}_f}{\delta}c\right), \tag{4.61}$$

with

$$Z = \frac{Ze}{2}\left(\frac{T_{ad} - \bar{T}_b}{\bar{T}_b - \bar{T}_u}\right). \tag{4.62}$$

Note that $\mathrm{Re}(c) > 0$. The root c is a complex number, which can be written as $c = k + il$. Substitution in equation (4.59) yields:

$$(k + il)^2 + k + il - (a + ib) = 0. \tag{4.63}$$

Or, by looking at the real and imaginary parts separately:

$$a = k^2 - l^2 + k, \tag{4.64}$$

$$b = 2kl + l \qquad \text{or} \qquad k = \frac{b}{2l} - \frac{1}{2}. \tag{4.65}$$

From the first relation, we eliminate k, to obtain a quadratic relation for l^2:

$$4(l^2)^2 + (l^2)(1 + 4a) - b^2 = 0. \tag{4.66}$$

Knowing that l is real, the solution reads:

$$l^2 = \frac{1}{2}\sqrt{(a + \frac{1}{4})^2 + b^2} - \frac{1}{2}(a + \frac{1}{4}). \tag{4.67}$$

Given the relation (4.65) for k and the implicit relation (4.67) for l, equations (4.57) and (4.58) can be written as

$$a = -Z \exp\left(-\frac{\bar{\psi}_f}{\delta}k\right)\cos\left(\frac{\bar{\psi}_f}{\delta}l\right), \tag{4.68}$$

$$b = Z \exp\left(-\frac{\bar{\psi}_f}{\delta}k\right)\sin\left(\frac{\bar{\psi}_f}{\delta}l\right). \tag{4.69}$$

In case of neutral stability, we must have that $a = 0$, which corresponds to $l = \pi\delta/(2\bar{\psi}_f)$. With these values for a and l, we can determine b from equation (4.67):

$$b = \frac{1}{4}\sqrt{\left\{2\left(\frac{\pi\delta}{\bar{\psi}_f}\right)^2 + 1\right\}^2 - 1}, \tag{4.70}$$

$$k = \frac{\bar{\psi}_f}{\pi\delta}b - \frac{1}{2}. \tag{4.71}$$

These values for a, b, k and l hold for the neutral stability point. On the other hand, the magnitude of the effective coefficient Z at the neutral stability point (i.e. the critical value Z_c), can be found from equations (4.69) and (4.71):

$$Z_c = b \exp\left(-\frac{\bar{\psi}_f}{2\delta}\right)\exp\left(b\frac{\bar{\psi}_f^2}{\pi\delta^2}\right), \tag{4.72}$$

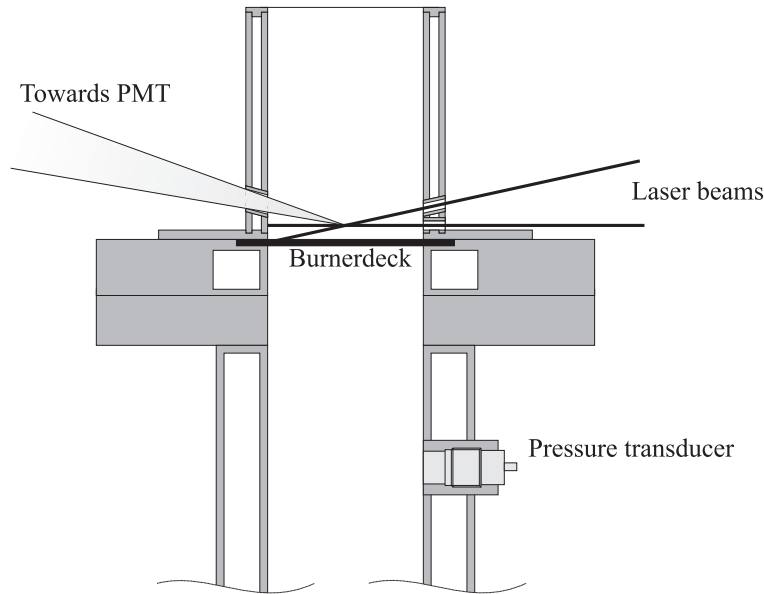with b given by equation (4.70).

Figure 4.2: Sketch of the burner head showing one pressure transducer, the laser beams of the laser-Doppler velocimeter and the burner deck. The burner deck and the upper part of the tube are (thermostatically) cooled. The total length of the tube below the burner deck is approximately 45 cm.

4.3 Experimental transfer function

The measurement of the transfer matrix element, coupling the acoustic velocities before and after the flame, involves the time-correlated measurement of the velocity upstream of the flame and downstream of the flame. These measurements are performed by Schreel *et al.* [51]. A way of determining *pressure* waves inside a tube is by means of multiple pressure transducers fitted in the wall of the tube [41]. If the medium in the tube has constant properties (density and temperature), two microphones suffice to characterise the complete wave. From the pressure wave and the properties of the medium and the tube, the velocity wave can be determined. The upstream region of the flame does have the desired constant density and temperature, but the downstream region does not, because the hot gas cools down rapidly. Therefore, the two microphone method has been chosen in the upstream region, but a direct measurement of the velocity in de downstream region by means of laser-Doppler velocimetry (LDV) is used instead. The LDV method uses two laser beams and at the intersection the velocity is determined by measuring the frequency difference in the reflected waves from small particles entrained in the flow [29].

The burner

The burner system essentially consists of a 50 cm long tube with a diameter of 5 cm (see figure 4.2). The bottom is closed with a flange, in which a small hole serves as inlet for

the premixed methane/air mixture. Some grids are fitted right after the inlet to settle the flow. In the lower part of the tube a hole is made in the side which is coupled by a flexible hose to a loudspeaker. The top is an open end, to allow the exhaust gas to escape. The burner plate is placed approximately 7 cm below the exit. This was done to avoid problems with the determination of the velocity fluctuations. An open end nearly acts as a perfect reflector of acoustic waves with, in first order, a maximum of the velocity fluctuations at the open end. A small portion of the acoustic energy, however, is radiated out, and a small transfer region exists in which the velocity fluctuations decrease strongly from the values associated with the wave inside the tube to the values outside the tube. The length of this region is approximately equal to the diameter of the tube. For this reason, the combustion area is placed 7 cm inside the tube. The part of the tube downstream of the burner plate and the burner plate itself are water cooled at nominally 50 °C. The burner plate itself is a perforated plate made of brass with a thickness of 2 mm. The perforation pattern is hexagonal, with a hole diameter of 0.5 mm and a pitch of 0.7 mm. The hole size is small enough that a flat methane/air flame stabilises on top of it (see chapter 5). To allow for the use of the two-microphone method, two pressure transducers are mounted in the side of the tube. Optical access to the downstream region of the flame is somewhat difficult since the burner plate is placed 7 cm before the open end. Three small holes have been made in the downstream part of the burner. Two serve as entrance for the two LDV laser beams, and through the third hole the scattered laser light from seeding particles in the flow is detected. In this way the velocity is measured in the middle of the tube at a height of 4 mm above the burner plate.

In principle, one does not measure the transfer matrix element of the flame in this way, but the transfer matrix of the flame combined with the burner plate. Test measurements showed however that the transfer matrix of the burner plate without flame is very close to unity for the frequencies of interest, and the influence can be neglected.

Another variable behaving differently in the experiments in the one-dimensional approximation of the system is the temperature of the burner plate surface. Since the flame is burner stabilised, some heat loss will occur via the burner plate. This will result in a parabolic temperature profile across the burner plate. But since we are measuring very close to the flame, the assumption will be made that the LDV measurement can be interpreted as a measurement of a true one-dimensional flame with a burner surface temperature equal to the temperature right below the measurement point. Also, the gas will be heated when passing through the burner plate and as a result the flow velocity will increase.

4.4 Results and discussion

In this section, numerical results with respect to the response of fluctuations in the mass burning rate, total heat release, heat loss to the burner and velocity are compared with the analytical model. First, the flame resonance phenomenon is studied. This resonance is observed in all responses of the flames in this thesis. The transfer functions obtained from one-step calculations, detailed calculations, and equation (C.12) derived by McIntosh *et*

al. [34] are also compared.

The response also predicts the stability of the flame. If the activation energy is large enough, the flame may oscillate spontaneously. The circumstances, in which this occurs, are described below.

Response of a perturbed flame

In our model, the phenomenon of resonance is easily recognised when the enthalpy fluctuations J' at the burner are in counter phase with the flame velocity $u'_f = u' - s'_L$. This is explained in figure 4.3, where a snapshot of a moving flame is shown. Assume that the flame is moving from a maximum distance variation x'_f towards the burner, with the corresponding flame velocity $u'_f = dx'_f/dt$, then the mass fraction profile at the burner outlet is also moving, resulting in a decreasing value of Y'. This induces enthalpy fluctuations at the burner ($x = 0$), which act as a boundary condition for the fluctuations in the enthalpy J' for $x > 0$. Depending on the diffusion coefficient and the stand-off distance, the phase difference of J' at the burner outlet $x = 0$ and the flame front $x = x_f$ can be $\pi/2$. This means that J' increases at $x = x'_f$, as shown in figure 4.3. The flame temperature T'_b and the burning velocity s'_L, or mass burning rate m', have the same phase as the enthalpy, so s'_L (or m') increases. In case of a resonance, the flame velocity is dominated by the mass burning velocity $u'_f = u' - s'_L \approx -s'_L$. Hence, u'_f and s'_L have opposite signs. This causes even higher flame velocity fluctuations, which means that we have a system that amplifies oscillations. Only one mode is found, for the reason that short-length waves are damped out.

 In other words: resonant behaviour is observed when there is a $\pi/2$ phase lag between the flame temperature and the heat loss to the burner. In this case, the variation in the burning velocity 'assists' the acoustic velocity perturbation giving a large acoustic perturbation in the burnt gas region. In the following this phenomenon is theoretically and numerically demonstrated by considering a methane/air flame, which has an equivalence ratio $\phi = 0.8$ and an upstream velocity $\bar{u}_u = 15$ cm/s. This mixture has a density of $\bar{\rho}_u = 1.131$ kg/m^3 and heat conductivity $\bar{\lambda}_u = 2.75 \times 10^{-2}$ J/(K m s). The temperature of the burner is fixed at $\bar{T}_u = 300$ K, the steady flame temperature is $\bar{T}_b = 1836$ K, and the adiabatic flame temperature is $T_{ad} = 2013$ K. The effective Zeldovich number Ze in equation (4.29) is obtained by numerical evaluation of stationary burner-stabilised flames for different gas velocities. Half the slope in the graph of $\ln(\bar{u}_u)$ as function of $1/\bar{T}_b$ can be considered as the effective activation temperature T_a. $Ze = 13.2$ is then found for a flame with upstream velocity $\bar{u}_u = 15$ cm/s. From equation (4.17), we find $\bar{\psi}_f/\delta = 2.3$. However, the comparison between the analytical and numerical results improves when the higher value 2.8 is used. This means that equation (4.17) underestimates the stand-off distance. A reason for this is that in the model the flame front is assumed to be infinitely thin, while numerically it has a finite thickness: the equilibrium is reached far downstream.

The absolute values and the phase shifts of the responses of s'_L, Q'_{rel} and Q'_{bur} to the upstream velocity fluctuations are shown in figures 4.4 to 4.6. In these figures, analytical results are compared with numerical results.
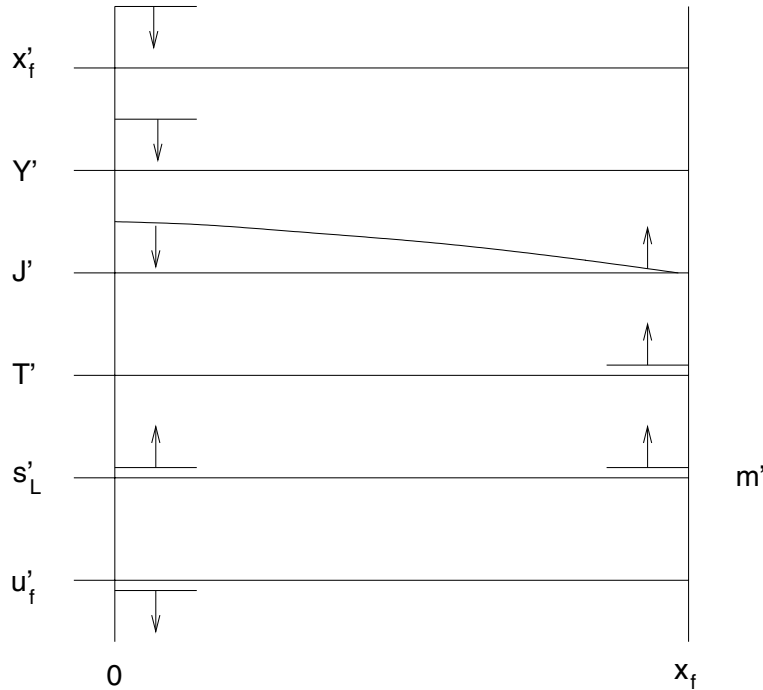
Figure 4.3: Snapshot of the phase of x'_f, Y', J', T', s'_L and u'_f in case of resonance.

Figure 4.4 shows that the curves for $|s'_L/u'_u|$ match for low frequencies reasonably well, but the phase shows a discrepancy for higher frequencies. For low frequencies we observe the quasi-stationary behaviour: the mass burning velocity fluctuations are equal to the gas velocity fluctuations. For higher frequencies, the flame cannot react on the distortions anymore ($|s'_L/u'_u| \to 0$) and in the vicinity of a frequency of 100 Hz, the curve shows a peak value. Mass flow fluctuations with this frequency induce strongly amplified mass burning rate fluctuations, as explained earlier.

Figure 4.5 shows the response of the total heat release on the upstream velocity fluctuations. Again, around 100 Hz the response shows a resonance peak, the amplitude is underestimated by the analytical model; the phase is predicted well. According to equation (4.38), the response of the total heat release should be proportional to the response of the mass burning rate. However, the numerically obtained phase shift in figure 4.5 (b) shows a decrease for higher frequencies, whereas in figure 4.4 (b) an increase is seen in the numerical results.

Figure 4.6 shows the response of the heat loss to the burner Q'_{bur}/u'_u. In the quasi-stationary limit $\omega \to 0$ we see that the numerical phase shift approaches $-\pi$ which is in accordance with the model. This value is found independent of $\bar{u}_u$ in the analytical model. In the numerical simulations this is not always the case, when much lower upstream velocities are considered. This different behaviour is the result of approximations in the analytical model. It is assumed that the heat loss increases when the flame moves towards the burner. This is intuitively clear because the stand-off distance decreases, if the temper-

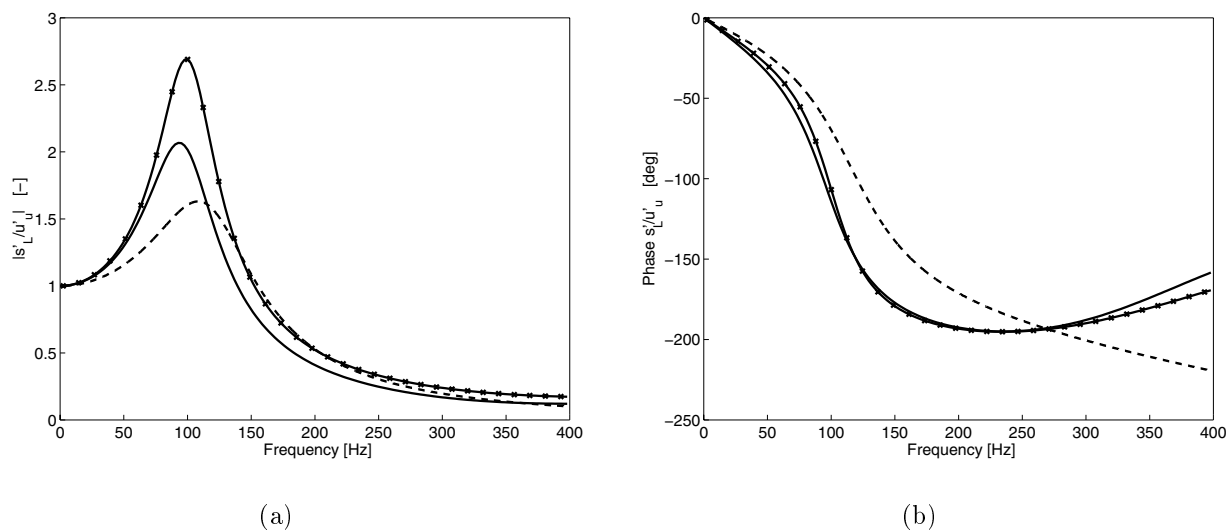(a)   (b)

Figure 4.4: Amplitude (a) and phase (b) of response of the burning velocity on the velocity fluctuations. Solid line: numerical model with one-step chemistry. Solid line with symbols: numerical model with skeletal chemistry. Dashed line: analytical model.
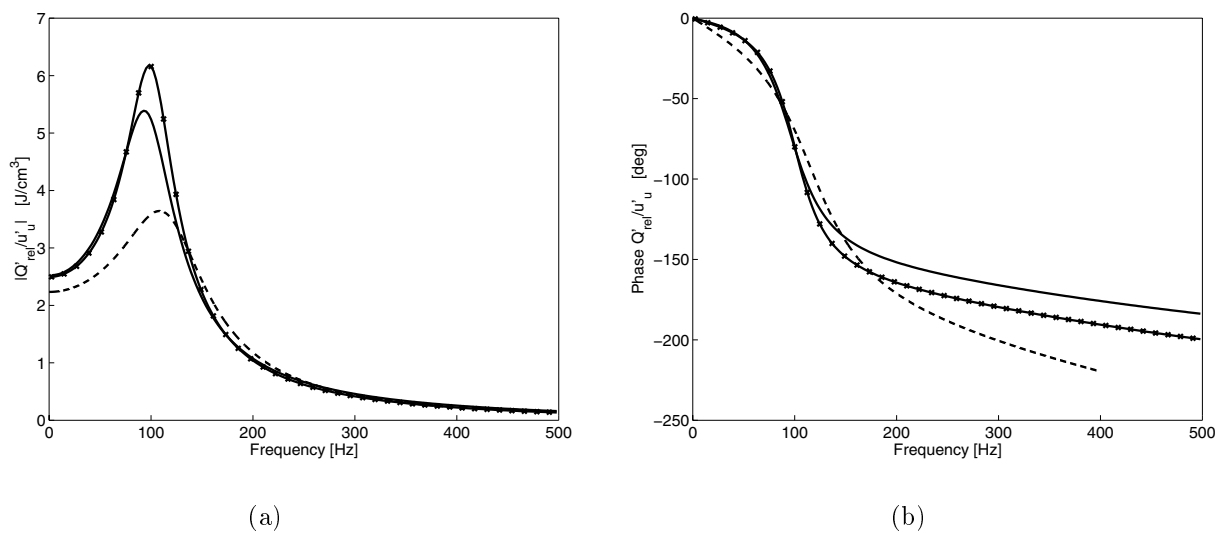

(a)   (b)

Figure 4.5: Amplitude (a) and phase (b) of response of total heat release on the velocity fluctuations. Solid line: numerical model with one-step chemistry. Solid line with symbols: numerical model with skeletal chemistry. Dashed line: analytical model.
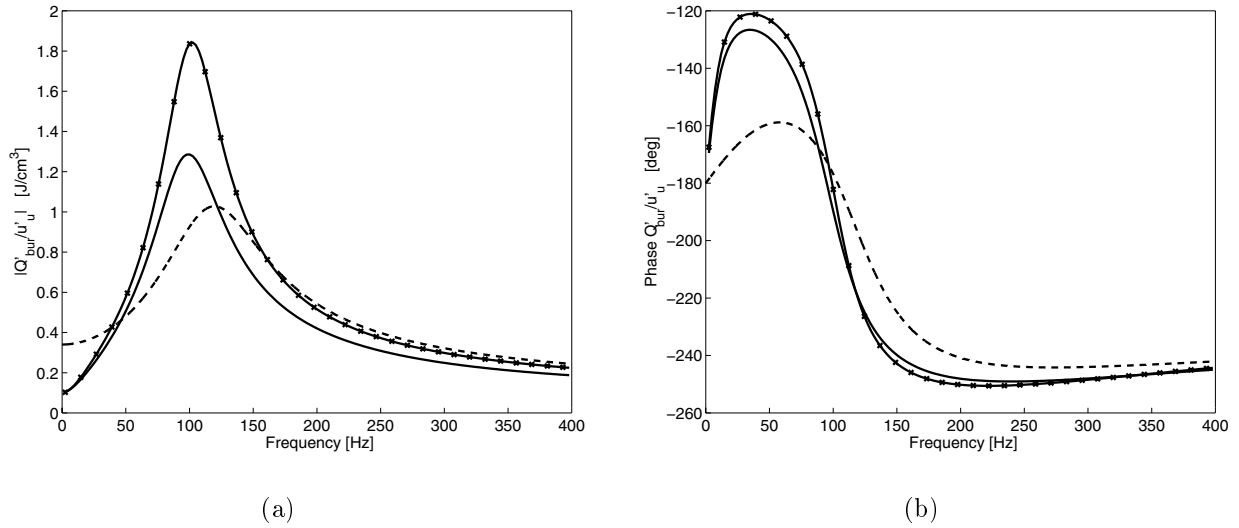
(a)   (b)

Figure 4.6: Amplitude (a) and phase (b) of response of the heat loss on the burner on the velocity fluctuations. Solid line: numerical model with one-step chemistry. Solid line with symbols: numerical model with skeletal chemistry. Dashed line: analytical model.

ature gradient increases. However, the quasi-stationary numerical response ($\omega \rightarrow 0$) of the heat loss $\bar{Q}_{\mathrm{bur}}$ does not only depend on the gas velocity, but also on the flame temperature. The relation between these quantities is given by:

$$\bar{Q}_{\mathrm{bur}} = \bar{\phi}_{\mathrm{u}} \bar{c}_p (T_{\mathrm{ad}} - \bar{T}_{\mathrm{b}}). \tag{4.73}$$

equation (4.35). We see that for low velocities and for almost adiabatic flames, the heat loss is small. This means that $\bar{Q}_{\mathrm{bur}}$ has a maximum at a certain gas velocity $\bar{u}_{\mathrm{u}}$. Thus, for a stationary flame $\bar{Q}_{\mathrm{bur}}(\bar{u}_{\mathrm{u}})$ has a negative as well as a positive slope. Consequently, the phase of the quasi-stationary response of Q'_{bur} on u'_{u} is either zero or $-\pi$ near $\omega = 0$. In the case of a flame at $\bar{u}_{\mathrm{u}} = 15$ cm/s the numerical calculations show a positive slope, which is the case for the analytical model as well (see equation (4.42)). If lower upstream velocities are used in the numerical model (e.g. 10 cm/s), we observe a zero phase in the quasi-stationary limit.

Figure 4.7 shows the response of the downstream velocity fluctuations to the upstream velocity fluctuations for different models. In this figure, the response equation (C.12) of McIntosh is also included. The results show that the phase shift tends to zero for high frequencies.

Both the one-step model and skeletal model in the numerical simulations predict the resonant behaviour in the acoustic response. The discrepancies between the models are mainly due to the fact that the parameters in the one-step model are fitted for a wide range of flames. Thus, for an accurate prediction of the response, even a simple model is useful. Another result is shown in figure 4.8, where the resonance peak frequency is plotted as function of the upstream velocity $\bar{u}_{\mathrm{u}}$. It shows that burner-stabilised flames have

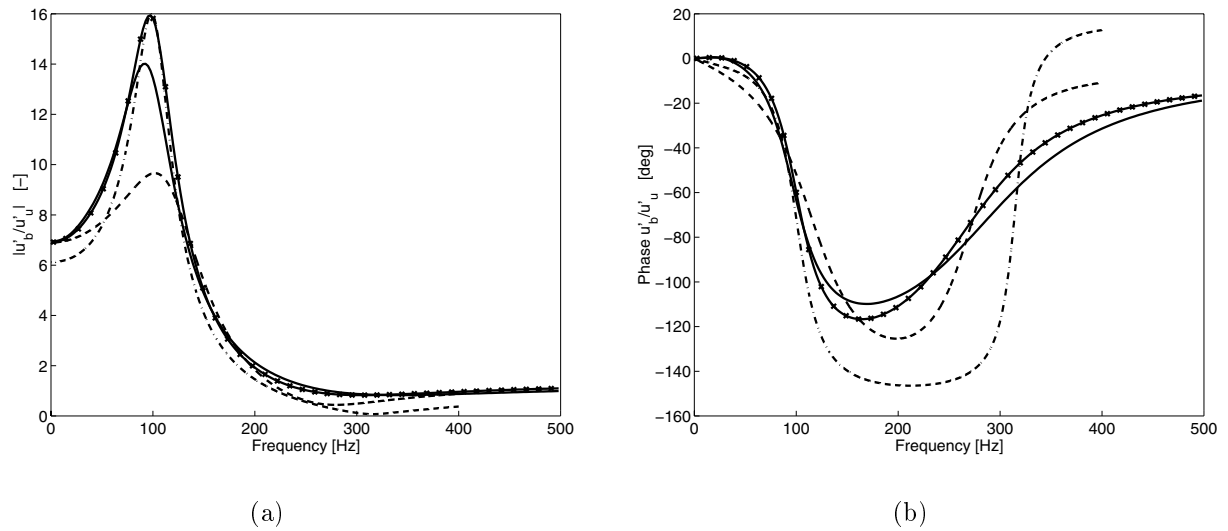(a)   (b)

Figure 4.7: Amplitude (a) and phase (b) of the transfer function for the velocity fluc-
tuations. Solid line: numerical model with one-step chemistry. Solid line with symbols:
numerical model with skeletal chemistry. Dashed line: analytical model. Dashed dotted
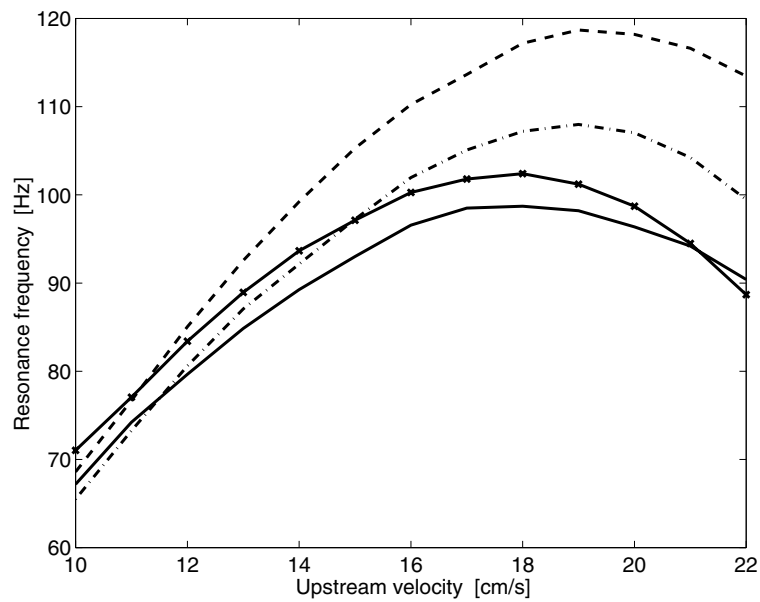line: McIntosh

Figure 4.8: Resonance frequencies as function of the upstream gas velocity for the different
models Solid line: numerical model with one-step chemistry. Solid line with symbols:
numerical model with skeletal chemistry. Dashed line: analytical model. Dashed dotted
line: McIntosh

a maximum resonance frequency. This frequency slightly differs between the investigated models, but show a similar behaviour.

Quasi-stationary limit $\hat{\omega} \to 0$

Finally, the quasi-stationary limit $\hat{\omega} \to 0$ of the analytical model presented in section 4.2, and the response derived by McIntosh *et al.* are compared. Different limits are obtained and the reasons for this difference are discussed.

In the analytical model (4.43) we find that:

$$\frac{u_{\mathrm{b}}'}{u_{\mathrm{u}}'} \to \frac{\bar{T}_{\mathrm{b}}}{\bar{T}_{\mathrm{u}}} + \frac{2}{Ze} \frac{\bar{T}_{\mathrm{b}} - \bar{T}_{\mathrm{u}}}{\bar{T}_{\mathrm{u}}}, \qquad \hat{\omega} \to 0, \tag{4.74}$$

in which two terms can be distinguished: the ratio of gas temperatures $\bar{T}_{\mathrm{b}}/\bar{T}_{\mathrm{u}}$ and an additional term dependent on the Zeldovich number. From a quasi-steady analysis, we also find this expression. By taking the limit in equation (C.12) of McIntosh, we find another limit:

$$\frac{u_{\mathrm{b}}'}{u_{\mathrm{u}}'} \to \frac{\bar{T}_{\mathrm{b}}}{\bar{T}_{\mathrm{u}}}, \qquad \hat{\omega} \to 0. \tag{4.75}$$

Clearly, this limit shows that relation (C.12) discards terms of higher order in Ze^{-1}. The jump conditions for the flame for small scale perturbations were justified up to order $O(Ze^{-1})$ and McIntosh anticipated here that these jump conditions are valid for high-order terms. This, however, was not proven [32].

The transfer function (4.43) predicts the correct quasi-steady limit, without using Large Activation Energy Asymptotics.

Ceramic foam burner

In figure 4.9, the responses of a flame stabilised on ceramic foam are shown. The surface temperature is fixed at different values ($T_{\mathrm{surf}} = 293$ K, 500 K, 750 K, and 1000 K). As the surface temperature increases, the flame stabilises closer to the burner, which results in a higher resonance frequency. The magnitude of the amplification decreases, and completely vanishes for high surface temperatures. It is clear that the analytical model predicts the resonance frequencies well for low surface temperatures, and underestimates the magnitude. However, the analytical model overestimates the response of the $T_{\mathrm{surf}} = 1000$ K case. For these high temperatures, the flame stabilises so close to the burner that fuel is burnt inside the burner, and the model does not cover these circumstances. The transfer function (4.55) predicts the resonant flame frequencies well, for higher surface temperatures the model breaks down.

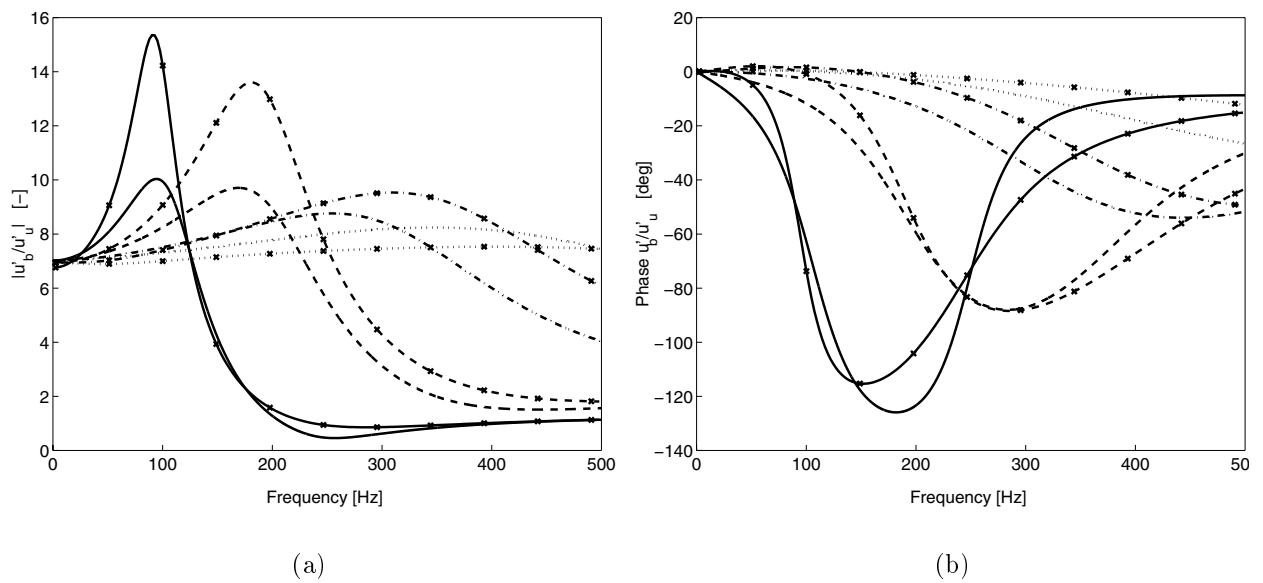(a)   (b)

Figure 4.9: Amplitude (a) and phase (b) of the response of fluctuating velocities of a flame stabilised on a burner with different (fixed) surface temperatures. Solid line: $T_{\mathrm{surf}} = 293$ K, dashed line: $T_{\mathrm{surf}} = 500$ K, dashed dotted line: $T_{\mathrm{surf}} = 750$ K and dotted line: $T_{\mathrm{surf}} = 1000$ K. The lines without symbols are obtained from the analytical model and the others are numerical calculations with skeletal chemistry.
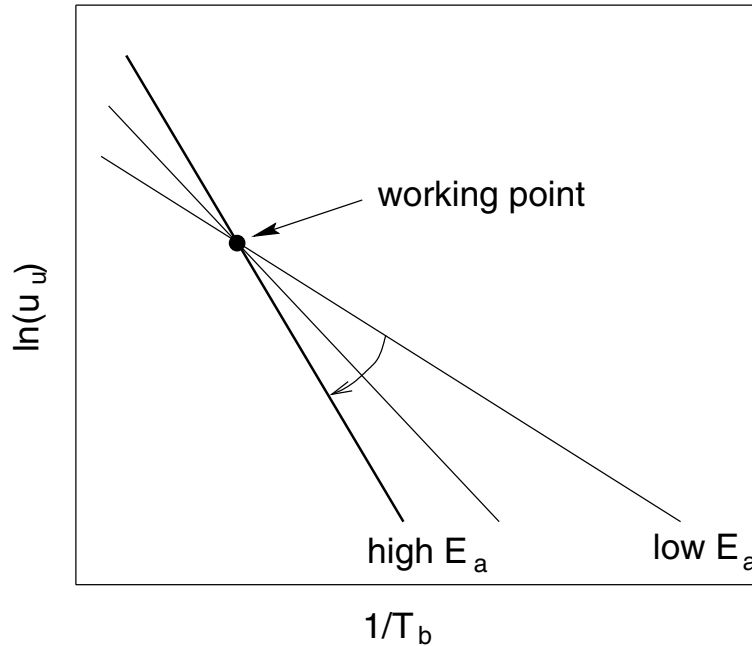
Figure 4.10: The effect on the Kaskan plot when the activation energy is increased.

Flame instability

Similar to the externally perturbed flames, the flame spontaneously oscillates if the phase difference of the enthalpy fluctuations at the flame front is such that the flame helps to increase the flame motion. This only occurs when the amplification of the mass burning rate by the flame temperature fluctuations is large enough to cancel out the damping of the fluctuating enthalpy. The frequency and growth rate at which the flame oscillates depend on the feedback coefficient Z. The neutral stability of burner-stabilised flames is determined by the critical value Z_c of Z in equation (4.62). The way to obtain the critical value is to increase the activation energy while keeping the flame temperature $\bar{T}_b$ constant. This procedure can be interpreted as changing the mixture properties. So, an activation energy $E_a = 137.173$ kJ/mole in the one-step chemistry mechanism corresponds to a methane/air mixture with $\phi = 0.8$, whereas a larger activation energy corresponds to a mixture of a higher hydrocarbon fuel. A larger activation energy can also be obtained by considering rich methane/air flames ($\phi > 1$).

In figure 4.10, the sensitivity of the flame temperature $\bar{T}_b$ due to variations in $\bar{u}_u$ is presented in a Kaskan-plot, being a graph of $\ln(\bar{u}_u)$ as function of $1/\bar{T}_b$(cf. equation (4.28)). When the activation energy is increased, the sensitivity increases and the negative slope becomes steeper, which leads to an increase of Z in equation (4.62).

Figures 4.11 and 4.12 show the results for the growth rate and the resonance frequency as function of the activation energy. These numerical growth rates are obtained by perturbing the steady solution at time zero, and following the time evolution of, in this case, the fluctuating outlet velocity. The growth rate is easily determined by looking at the slope
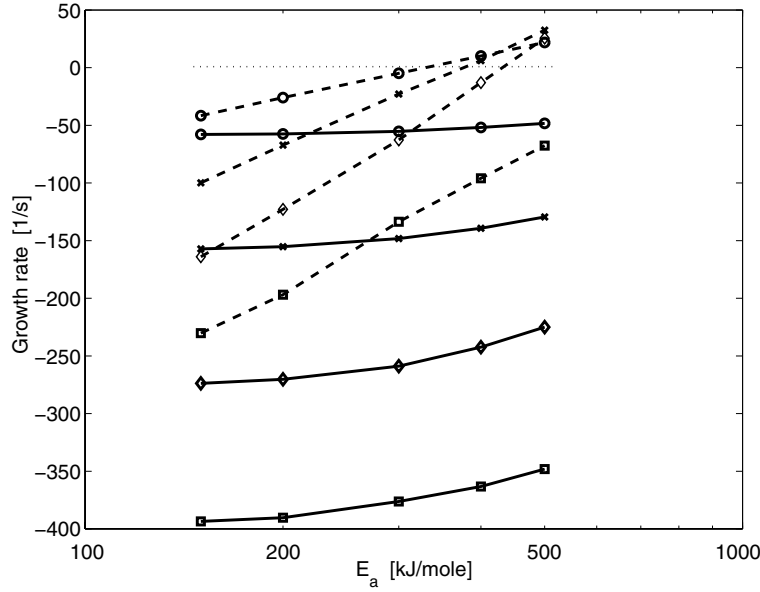
Figure 4.11: Growth rates for four velocities as function of the activation energy: the line with the circles: $\bar{u}_u = 5$, symbol $\times$: $\bar{u}_u = 10$, diamonds: $\bar{u}_u = 15$, and squares: $\bar{u}_u = 20$ cm/s. Solid lines: analytical model, dashed lines: numerical results. The thin dotted line denotes the zero-stability line (growth rate is zero).

of the logarithm of the amplitude as function of time. The figures show that, if the inlet velocity decreases, the growth rate increases and the resonance frequencies decrease, for fixed E_a.

Theoretically, this can be understood by looking at the relation between a and b, derived from equations (4.68) and (4.69). Figure 4.13 shows this relation for four inlet velocities (the frequencies are still dependent on the flame temperature). It is clear that the resonance frequencies increase when the inlet velocity $\bar{u}_u$ decreases. From this figure we also see that frequencies lower than the neutral frequency $a = 0$, the growth rate is negative, hence these modes are damped out, whereas the higher frequency modes are unstable. For each inlet velocity a unique resonance frequency can be found, which corresponds to a unique critical value $Z = Z_c$.

Figure 4.14 shows the imaginary part of $MN(\hat{\omega})$ (cf. equation (4.32)) as function of the frequency b for several values Z. For this particular flame ($\bar{u}_u = 15$ cm/s, $\phi = 0.8$), $Z = 2.6$. For this and any other flame, it is possible to find the critical value Z_c, where the flame is neutrally stable. Above this value, the flames are unstable.

By interpolation, the numerical activation energies and their corresponding Z on the neutral-stability line are determined (see the dotted line in figure 4.11). Figure 4.15 shows the results for the values Z_c obtained from the numerical simulations and the theoretical model. On a logarithmic scale, these values show roughly a linear dependence on the inlet velocity. However, the analytical model predicts substantially larger critical values than in the numerical simulations. This means that the flames are more unstable than the
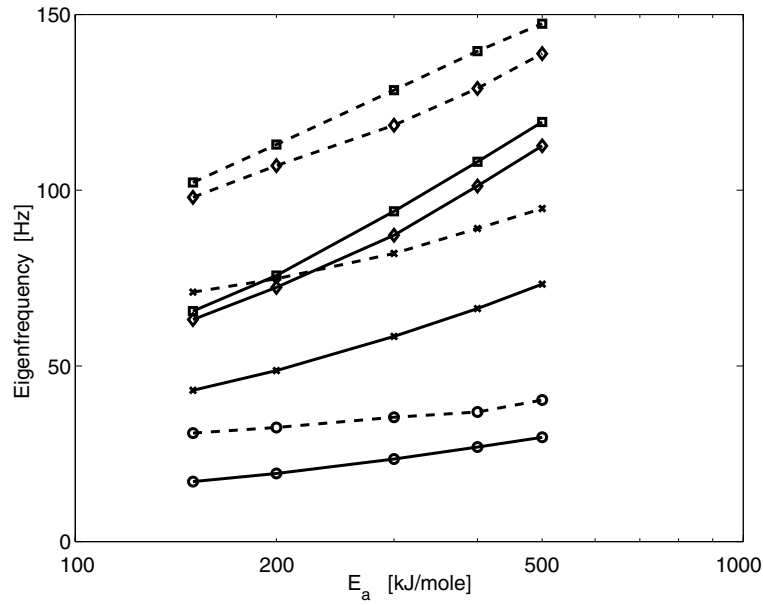
Figure 4.12: Resonance frequencies for four velocities as function of the activation energy: lines with the circles: $\bar{u}_u = 5$, symbol x: $\bar{u}_u = 10$, diamonds: $\bar{u}_u = 15$ and squares: $\bar{u}_u = 20$ cm/s. Solid lines: analytical model, dashed lines: numerical results.
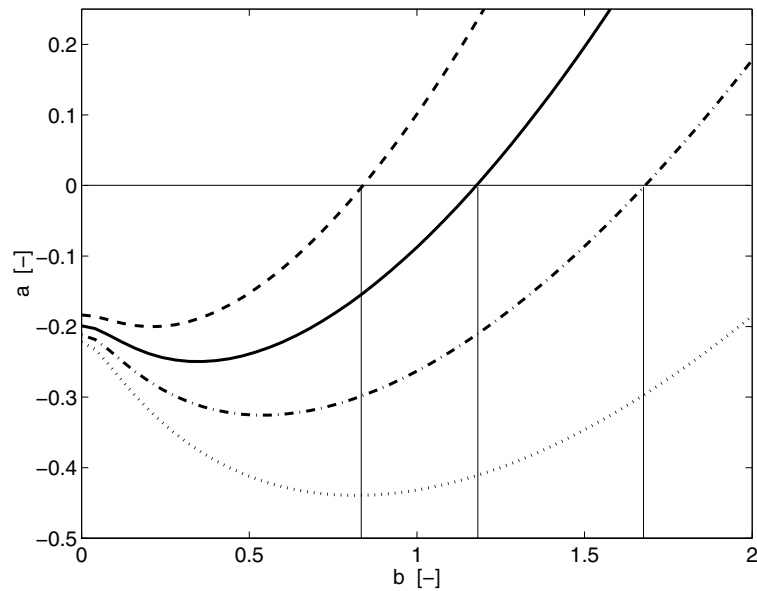

Figure 4.13: Relation between the growth rate a and resonance frequency b for four inlet velocities. Dashed line 20 cm/s, solid line 15 cm/s, dash-dotted line 10 cm/s, and dotted line 5 cm/s. Line $a = 0$ corresponds to the neutral stability.
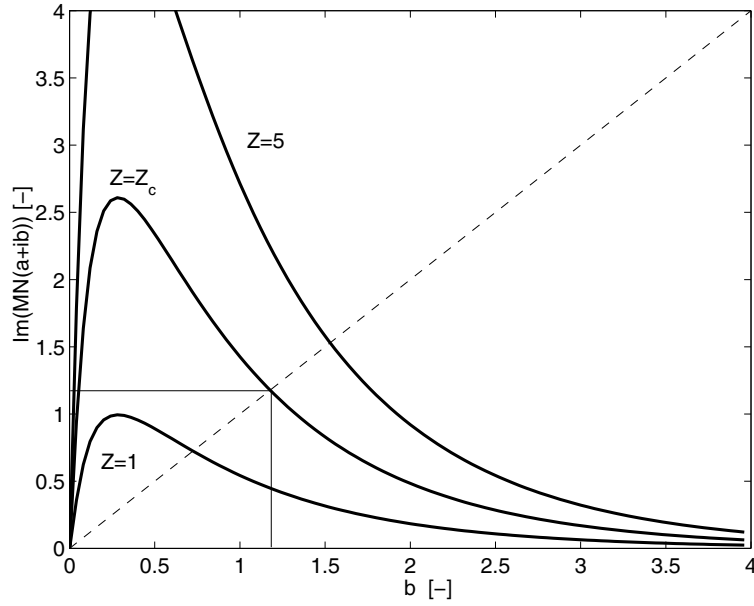
Figure 4.14: The imaginary part of the frequency condition for several values of Z and $\bar{u}_\mathrm{u} = 15$ cm/s. The intersection with the dashed line represents the resonance frequencies. At the critical value Z_c the flame is neutrally stable.

theoretical model predicts.

It must be noted that the methane flames ($\phi = 0.8$ and $E_\mathrm{a} = 137.173$ kJ/mole) used in this thesis are all stable ($a < 0$). It is known that rich methane/air flames are unstable for sufficiently low inlet velocities [19], since they have larger effective values for E_a. The model derived in section 4.2.5 qualitatively predicts the trends in the resonance frequencies, but fails for the determination of growth rates. This result is also found in [19], where it is shown that a higher-order analysis (in Ze^{-1}) is needed to predict the main features of the growth rate.

Experiments

Below, results from the numerical simulations are compared to the experimental results, using the setup described in section 4.3. In figure 4.16 the frequency dependence of $\mathcal{V}$ is plotted for $\phi = 0.8$ and $\bar{u}_\mathrm{u} = 14$ cm/s. One can clearly see the resonance at about 150 Hz in the experiments. For low frequencies the absolute value of the transfer function tends to a value around 7, which corresponds to the stationary limit, where $\bar{u}_\mathrm{b} = (\bar{T}_\mathrm{b}/\bar{T}_\mathrm{u})\bar{u}_\mathrm{u}$. For higher frequencies the amplification drops to values around 1. The correspondence to the numerical simulation is good. Both the phase and the magnitude of the transfer function are quantitatively close to the measured values. For four different values of the inlet velocity ($\bar{u}_\mathrm{u} = 10$ cm/s, $\bar{u}_\mathrm{u} = 14$ cm/s, $\bar{u}_\mathrm{u} = 18$ cm/s, and $\bar{u}_\mathrm{u} = 22$ cm/s), experiments have been carried out at $\phi = 0.8$ and with a cooling water temperature of 50 °C
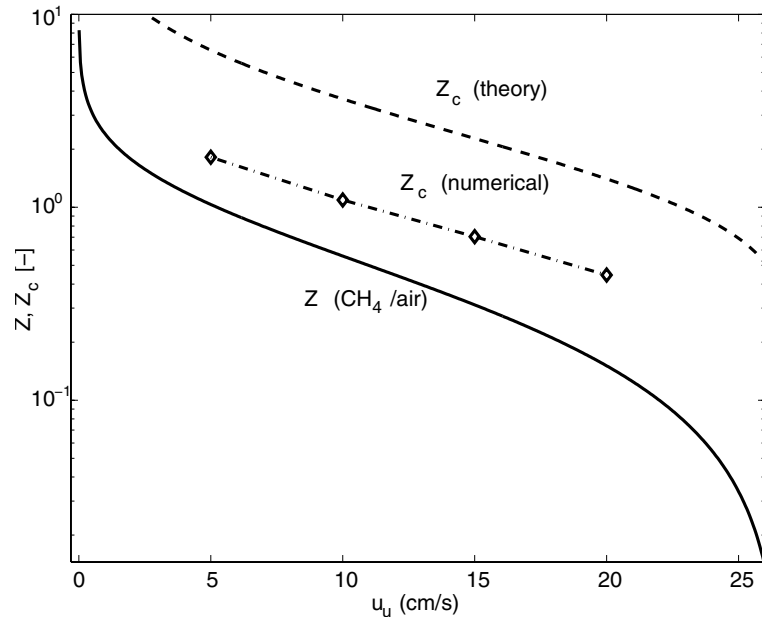
Figure 4.15: Values Z for a methane/air flame, and the critical values Z_c as function of the inlet velocity. Dashed lines are results using the model, and the dash-dotted lines are numerically obtained results.
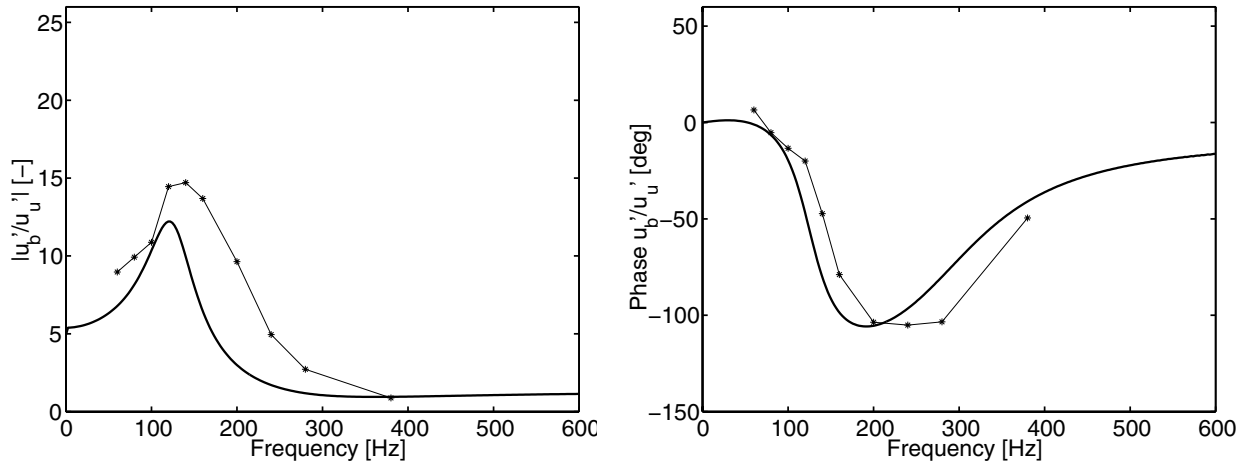

Figure 4.16: The frequency dependence of the absolute value and phase of the transfer function $\mathcal{V}$ for $\bar{u}_u = 14$ cm/s and $\phi = 0.8$. Thick lines are numerical results and thin lines with symbols are experimental results. Clearly a resonance can be identified which is well predicted by the numerical simulation.
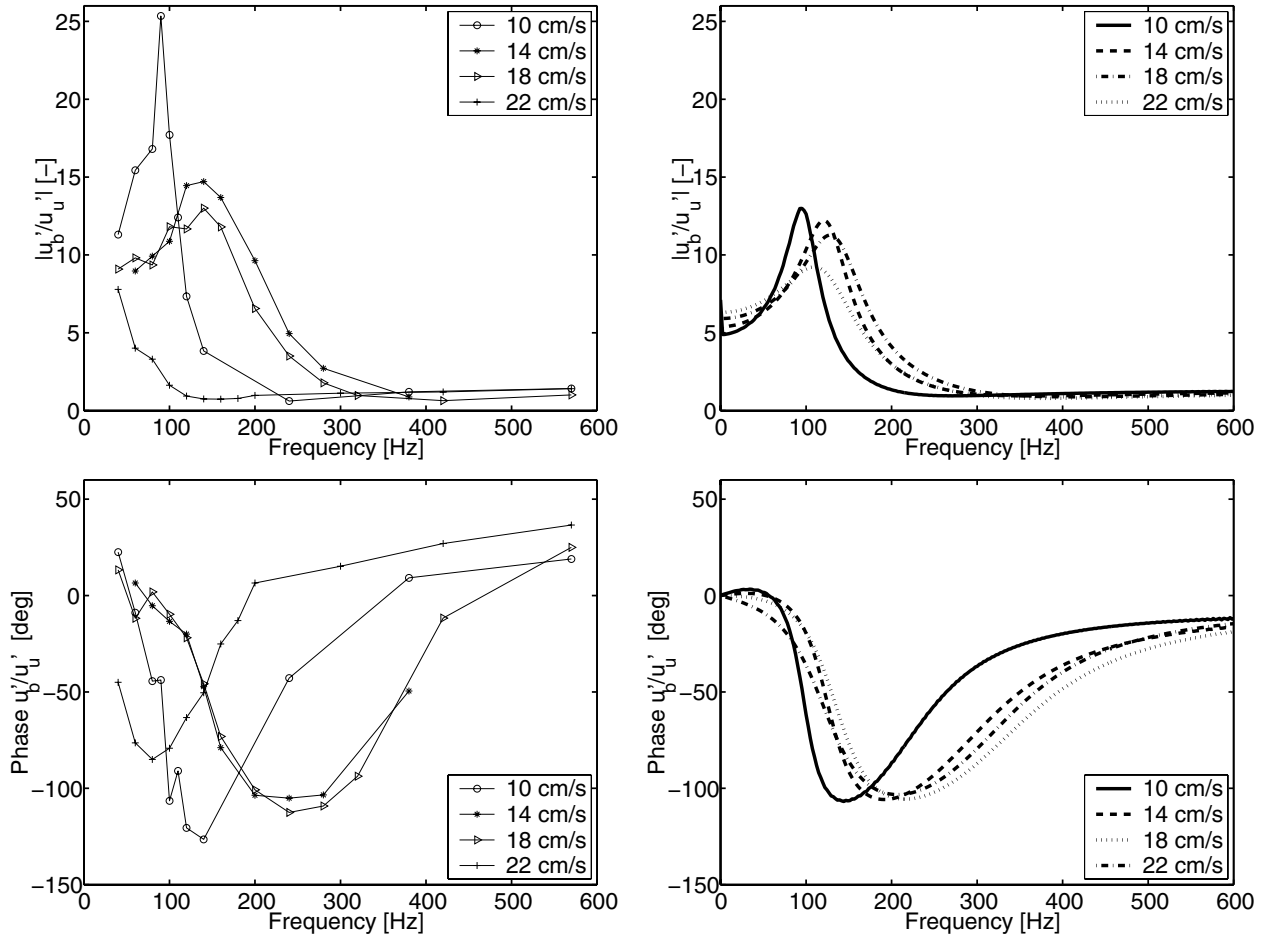
Figure 4.17: The dependence of the transmission coefficient on the frequency for several upstream flow velocities $\bar{u}_\mathrm{u}$ with fixed $\phi = 0.8$. The left two graphs represent the experimental data, and the right two graphs represent the numerical simulations.

(so that $T_\mathrm{surf} = 50^\circ\mathrm{C}$). The net effect of the variation in mass flow is that both the flame temperature and the stand-off distance are influenced. For low decreasing mass flows, the stand-off distance will increase, but the flame temperature will decrease. The experimental results show indeed lower resonance frequencies and increasing amplification. For a flow near the adiabatic burning velocity ($\bar{u}_\mathrm{u,ad} = 23.9$ cm/s), the stand-off distance increases again, which results in a sudden decrease in resonance frequency. For 22 cm/s, this resonance frequency is undetectably low. These results are more or less confirmed by the simulations. The strong amplification at 10 cm/s is not predicted, nor the strong decrease in resonance frequency at 22 cm/s. The overall picture is, however, the same. For the experiment near the adiabatic burning velocity one has to take into account that small errors (either experimentally or numerically) can have a strong impact on the result. In numerical simulations the behaviour as observed experimentally at 22 cm/s, has also been obtained for different settings.

The results show a clear resonance type of behaviour for a flat flame, with amplification factors as high as 25. These resonances occur in the region 80–200 Hz, depending on the flow properties. For shorter stand-off distances (controlled by the burner surface temperature) higher resonance frequencies are observed. The correspondence to numerical simulations is good, both qualitatively and quantitatively. This indicates that the numerical model can be used to calculate the acoustical properties of the burner in a full scale acoustical model for heating devices.

Chapter 5

Acoustics in two-dimensional flames

Real flames are three-dimensional structures. In the special case that the flame does not change in certain directions, the flame becomes a less complicated structure. The one-dimensional flames in chapter 4 are believed to be a special case of the two-dimensional flame stabilised on a slit burner. If the diameter of the slits is small enough, the effects parallel to the burner plate can be neglected. In this chapter, the stationary and acoustic behaviour of flames for such small perforation diameters are investigated numerically. This investigation might also give clues for an extended acoustic transfer model of two-dimensional flames stabilised on a burner.

5.1   Introduction

In the literature, experimental and numerical studies are performed on the acoustic interaction of Bunsen type flames on relatively large single-slit burner configurations [12, 20]. In these studies, an extended analytical model of Fleifil *et al.* [17] is adopted to describe the shape of the flame as function of time. The model uses a G-equation description of the flame front. It is assumed that the burning velocity is constant and that the total heat release is proportional to the flame front area. The model predicts the wrinkles in the flame shape caused by the fluctuating velocity field, which are also seen in experimental work [12]. This model can be applied only to strongly perturbed Bunsen flames, and does not describe the phenomena observed in a burner-stabilised flame.

The type of flame that is closer to the one-dimensional case of chapter 4 is the flat flame, which stabilises on a perforated burner plate with small perforations. This flame shows small changes in directions other than the global flow direction [57]. The configuration, as defined in section 2.4, models a perforated plate for which the dimensions of the perforations are chosen small so that a flat flame is formed. This micro-slit burner will be studied numerically in this chapter. In figure 5.1 the numerical domain is shown. The grid is equidistant (24 cells in horizontal direction and 336 cells in vertical direction). The domain is chosen quite small to limit the total number of cells and have a spatial resolution comparable to the smallest resolution in the one-dimensional calculations. The limited
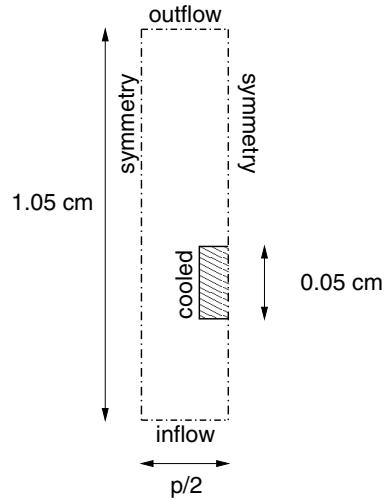
Figure 5.1: Computational domain of the micro-slit burner. The domain is limited by using symmetry, inflow and outflow boundaries.

vertical length (1.05 cm) has an influence on the steady-state solution: the diffusion terms are not completely negligible at the outflow. This small domain, however, does not have a big impact on the acoustic phenomena (slightly increased resonance peak, due to a higher flame temperatures). For a good comparison, the one-dimensional simulations in this chapter are conducted on the same domain with an equal equidistant grid. For larger domains, local grid refinement should be applied to limit the number of grid points [58].

Section 5.2 gives a numerical analysis of the stationary flame on a micro-slit burner and section 5.3 investigates acoustic phenomena of this flame. In both sections the zero limit of the diameter ($d \rightarrow 0$) is used to make a connection between the one-dimensional (cf. chapter 4) and two-dimensional flames. The results give insight to the two-dimensional acoustic effects of flames stabilised on a micro-slit burner.

5.2   Analysis of the stationary micro-slit burner

The steady case of a micro-slit burner problem has been studied numerically by De Goey *et al.* [8] using the streamfunction-vorticity formulation for the steady flow field. From [8], it has become clear that the diameter versus pitch ratio d/p is very important and should be chosen larger than 0.5, otherwise blow-off occurs at relatively large velocities. This ratio should also be smaller than 0.8, otherwise burner loads become too large. A diameter versus pitch ratio of 2/3 is a compromise and small diameters d with this fixed ratio show geometrically flat flames. The limit $d \rightarrow 0$ with fixed d/p corresponds to the one-dimensional burner-stabilised flames [52].

In contrast to the one-dimensional flames, the slit burner configuration includes a complex flow pattern around a bluff body. An isothermal flow passing obstacles is an extensively studied problem. Many aspects to the problem can be recognised, such as counter-flow
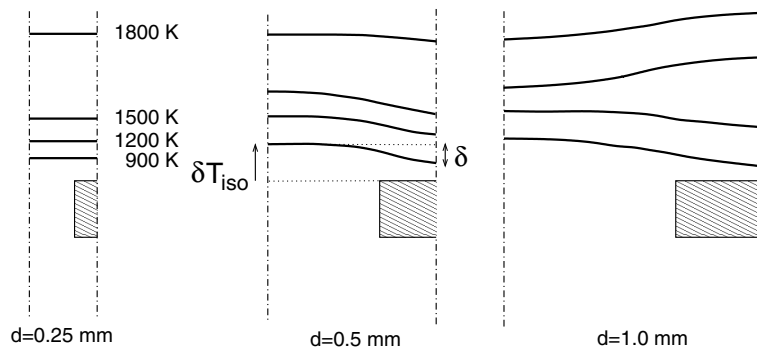
Figure 5.2: Definition of the isotherms, distances T_{iso} and δ

patterns in the wake of the body as found in the backward facing step problem.

Near the burner outlet, pressure singularities and high heat fluxes are present. Numerically, it is hard to resolve those details. Thus, the two-dimensional problem should be solved on very fine grids in all directions, despite the flame being almost one-dimensional. In order to limit CPU-time, all the results are generated using one-step chemistry.

Another aspect is the formation of the parabolic flow pattern in the perforations of the plate. This particular flow profile is dependent on the Reynolds numbers Re of the flow. If $Re > 2300$, the flow is turbulent. In such a flow, the velocity is almost homogeneous, except in the boundary layers, where the velocity quickly varies from the no-slip conditions to the mean flow velocity. In the flow through the slits, studied in this chapter, Reynolds numbers are low enough ($Re \approx 10$) to assume that the flow is laminar.

In the study by Bosch [8], an indicator of the flame stand-off distance is introduced. The parameter δ is defined as being the difference in height of a certain isotherm with value T_{iso} in the centre of the flow channel and in the centre of the plate segment. Consequently, δ is equal to zero if the flame is one-dimensional. Furthermore, $\delta T_{\mathrm{iso}}(d)$ is the distance of the isotherm above the burner plate at the centre of the slit channel for a given diameter d.

If the flame becomes more curved, the height found at the centre boundary will differ more and more from the one found at the side boundary. Schematically, this idea is presented in figure 5.2, where four isotherms are shown for three steady-state computations. The δT_{iso} values are calculated for isotherms equal to 900 K, 1200 K, and 1500 K, in a flame with $\phi = 0.8$ and $\bar{u}_{\mathrm{u}} = 15$ cm/s. Figure 5.3 shows the results of $\delta T_{\mathrm{iso}}(d) - \delta T_{\mathrm{iso}}(0)$ for the same flames. Note that the flame stabilises closer to the burner when d is increased. For $d = 1$ mm, the flame distance increases again. δ divided by half the pitch gives the typical curvature of the flame. In [8] the (steady) flame is said to be flat if $2\delta/p$ is less than 0.1 for the 900 K isotherm. The reference value of $T = 900$ K has been chosen, because this is the approximate temperature above which chemical reactions become important. This criterion gives a global indication of the flatness of the flame. According to the criterion, the three geometries are flat ($d = 1$ mm: $2\delta/p = 0.070$, $d = 0.5$ mm: 3.38×10^{-2}, and $d = 0.25$ mm: 3.70×10^{-3}). The critical diameter d_{c} is the largest diameter for which the criterion holds. In [8], it is found that this value is 0.35 mm for skeletal chemistry with

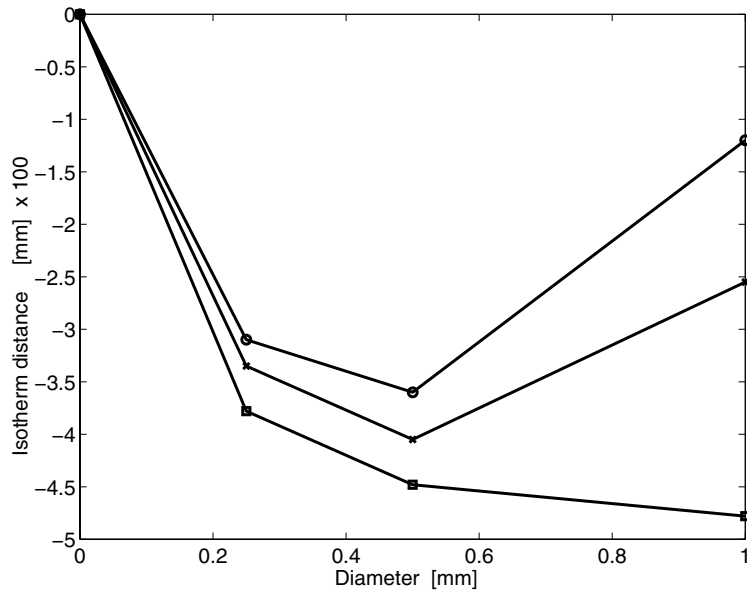Figure 5.3: Isotherm distance differences $\delta T_{\mathrm{iso}}(d) - \delta T_{\mathrm{iso}}(0)$ as function of the diameter. Circles: $T_{\mathrm{iso}} = 900$ K, crosses $T_{\mathrm{iso}} = 1200$ K, and squares: $T_{\mathrm{iso}} = 1500$ K.

fixed $d/p = 2/3$.

The position of the flame front (defined as the line with the local maxima of the total heat release) is dependent on the diameter and varies above the burner plate, when the flame is not one-dimensional. Figure 5.4 shows the flame fronts for three perforation diameters. The results show that the flame has a minimum distance from the burner at approximately $d = 0.5$ mm, which can also be seen in figure 5.3. For decreasing diameters, the flame front becomes flatter, as expected. For comparison, the stand-off distance for the one-dimensional case is 0.55 mm. Even with the smallest diameter used ($d = 0.25$ mm) the perforations are large enough to stabilise the flame closer to the plate. Results from [8], with one-step chemistry, show that the pressure drop across the flame, caused by the expansion of the hot gases, distorts the flow field significantly. The position where the flow becomes homogeneous again is called the outlet length. The cold-flow (flow without the flame) outlet lengths are far greater than a typical stand-off distance of the flame. For a slit diameter $d = 1$ mm and uniform inlet velocity $\bar{u}_{\mathrm{u}} = 15$ cm/s the cold-flow outlet length is approximately $L_{\mathrm{outlet}} = 4$ mm, whereas the stand-off distance $\bar{x}_{\mathrm{f}}$ for a one-dimensional burner-stabilised flame with this inlet velocity is 0.55 mm. However, in flat flames the flow becomes homogeneous again at distances smaller than the stand-off distance. In figures 5.5 (a) and (b) the velocity field is shown for a perforated plate with $d = 0.25$ mm. Due to the presence of the flame and the small dimensions of the plate segments, no recirculation zone is present just downstream the plate segments. It also shows that the velocity profile inside the perforations is a Poiseuille flow and becomes homogeneous again at two tenths of a millimetre above the burner plate, well below the flame front.
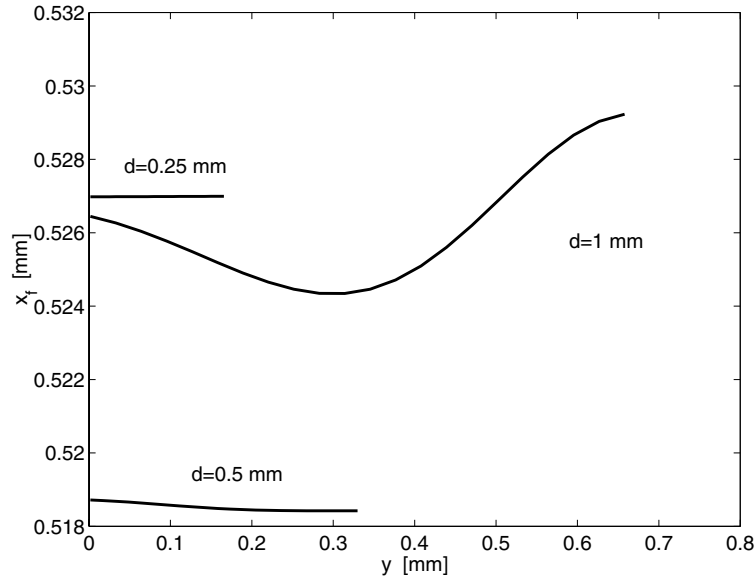
Figure 5.4: Position of flame fronts at burner with varying perforation diameters.

The sharp edges of the plate cause a pressure singularity at the corner of the burner plate as shown in figure 5.5 (c). On the inflow side of the burner plate pressure builds up and the contraction causes a pressure drop, which is 0.4 Pa for $d = 0.5$ mm and 0.7 Pa for $d = 0.25$ mm ($\Delta p / \bar{p}_0 = O(10^{-6})$), of the same order as found in section 3.5.3). At the outflow, the pressure drops quickly, resulting into a pressure sink at the edge on top of the plate, as shown in figure 5.6. These two-dimensional effects are larger if the diameter decreases, but confined to a smaller area. The enthalpy also has a sink on the outflow side of the burner, as shown in figure 5.7. This is caused by the heat loss of the flame near the plate segment.

Compared to the ideally cooled burner, the average temperature at the cross sectional area at $x = 0$ is higher, which results in a heat loss at the walls inside the burner plate for $x < 0$. Figure 5.8 shows the local heat loss for different diameters. It can be seen that at the corner on the burnt side most heat is lost and the heat loss decreases towards the symmetry axis. An exception is the computation for $d = 1$ mm, where near the centre of the plate segment, the mass flow is low and the heat loss becomes higher. In the limit $d \to 0$, the heat loss is expected to be homogeneous at the top wall of the plate segment. However, a peak is present at the corner, where the flame at the centre of the flow loses most of its heat.

From the analysis of the isotherms, it is clear that the gas temperature profile inside the burner plate is not equal to the temperature of the burner plate. Heat is transferred to the burner at a finite rate inside the burner area for $x < 0$. Figure 5.9 shows the average temperature profile in the burner plate. A global heat transfer coefficient αS can be defined by integration of the temperature difference along the y-axis inside the burner and
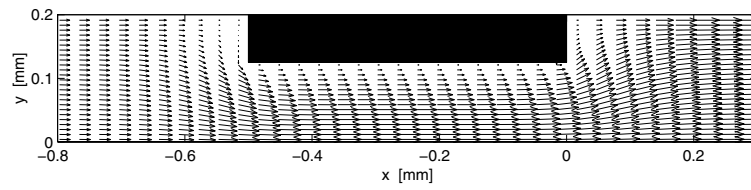
(a) Velocity vectors
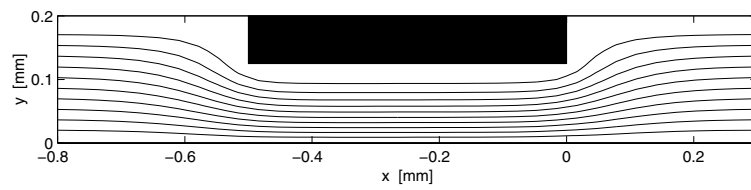
(b) Streamlines
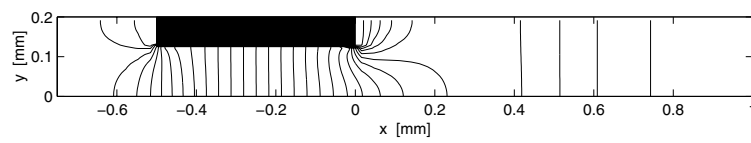
(c) Isobars

Figure 5.5: Flow through the perforated plate for a flame with $\bar{u}_u = 15$ cm/s, $\phi = 0.8$ and $d = 0.25$ mm.
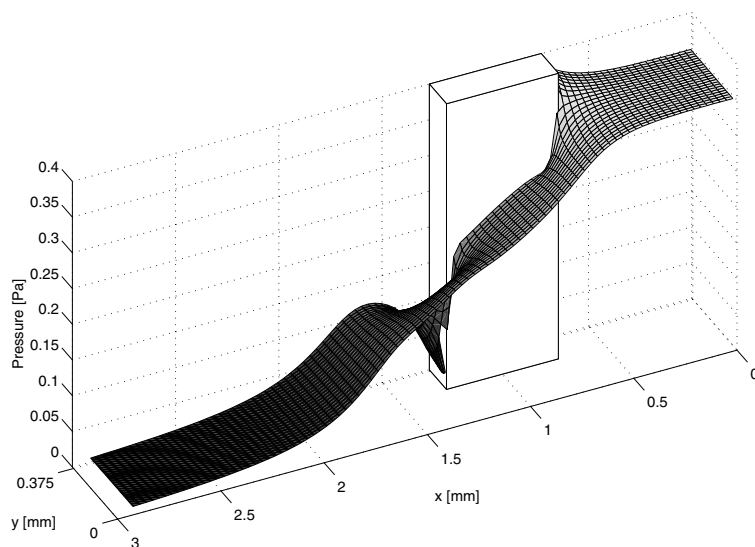
Figure 5.6: Pressure distribution in the perforated plate configuration for a flame with $\bar{u}_{\mathrm{u}} = 15$ cm/s, $\phi = 0.8$ and $d = 0.5$ mm. Note that the gas flows from right to the left in this figure.
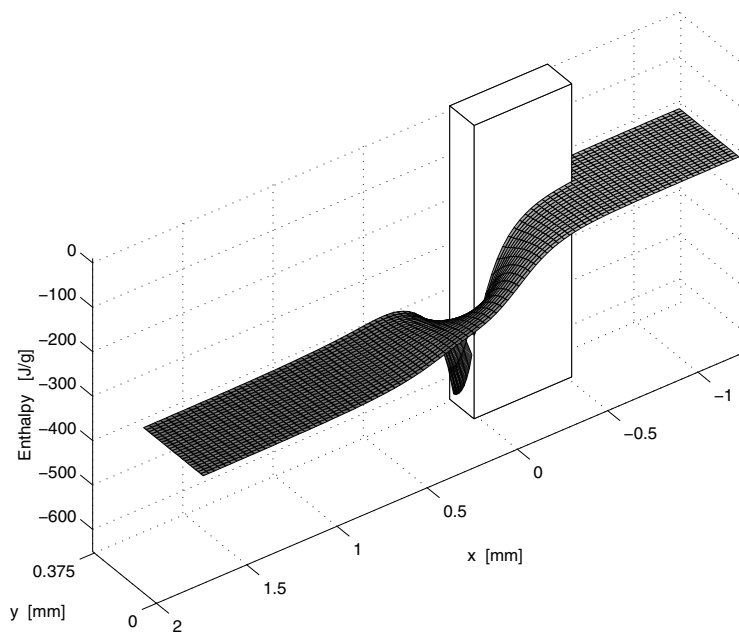
Figure 5.7: Enthalpy distribution in the perforated plate configuration for a flame with $\bar{u}_{\mathrm{u}} = 15$ cm/s, $\phi = 0.8$ and $d = 0.5$ mm.
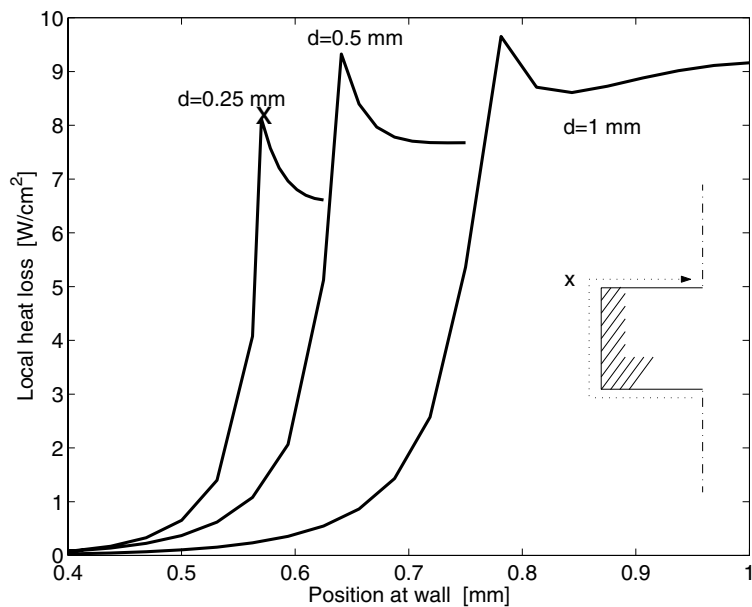
Figure 5.8: Local heat loss as function of the position on the wall, starting on the unburnt side at the symmetry axis (see inlay picture). The cross indicates the maximum heat loss at the downstream corner.
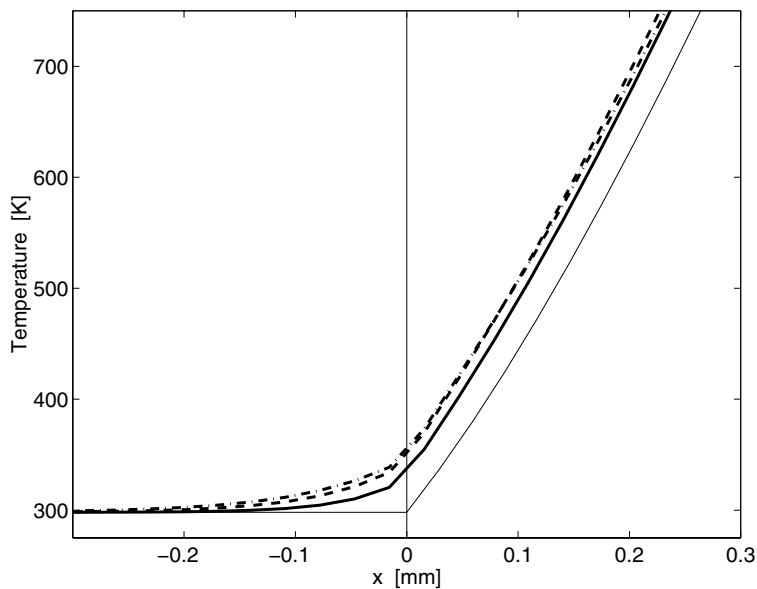
Figure 5.9: The temperature profile near the burner plate for different diameters in case of $\phi = 0.8$ and $\bar{u}_u = 15$ cm/s. The profile is averaged over the y-axis. Solid line: $d = 0.25$ mm, dashed line: $d = 0.5$ mm, dash-dotted line: $d = 1$ mm, and thin line: $d = 0$ mm (1D).
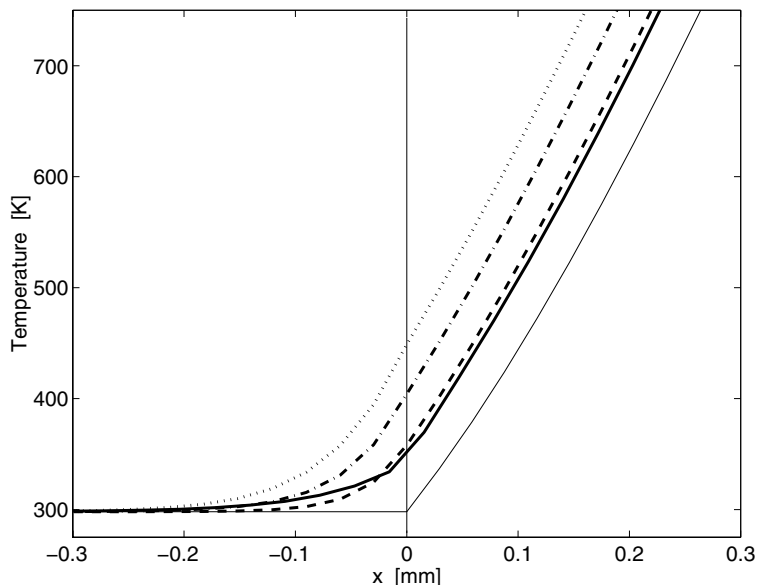
Figure 5.10: The temperature profile near the burner plate for different αS values in case of $\phi = 0.8$ and $\bar{u}_{\mathrm{u}} = 15$ cm/s. Solid line: two-dimensional calculation (averaged), $d = 0.5$ mm, dashed line: one-dimensional calculation, $\alpha S = 11.2$ W/(cm^{3}K), dash-dotted line: $\alpha S = 5$ W/(cm^{3}K), dotted line: $\alpha S = 3$ W/(cm^{3}K), and thin solid line: one-dimensional calculation with $\alpha S = \infty$.

comparing it to the total energy per unit length that is lost to the burner $\bar{Q}_{\mathrm{bur}}$ (W/m):

$$\alpha S \int_{A} (\bar{T} - \bar{T}_{\mathrm{s}}) \, \mathrm{d}A = \bar{Q}_{\mathrm{bur}}, \tag{5.1}$$

where $\bar{T}_{\mathrm{s}}$ is the (fixed) temperature of the burner plate and A the surface of the flow inside the burner plate. This heat transfer coefficient can be used in the one-dimensional simulations to model a perforated burner plate. For $d = 0.5$ mm it is found that $\alpha S = 11.2$ W/(cm^{3}K). Figure 5.10 shows one-dimensional simulations with various heat transfer coefficients for a burner with $\bar{u}_{\mathrm{u}} = 15$ cm/s, $\phi = 0.8$, and porosity $d/p = 2/3$. The results show that the heat transfer coefficient $\alpha S = 11.2$ W/(cm^{3}K) can be used for modelling this particular burner plate. Lower heat transfer coefficients result in higher gas temperatures inside the burner plate, yielding a smaller stand-off distance. In stationary one-dimensional flame calculations, a finite αS captures the global structure of the temperature profile. Besides that, the stand-off distance of the two-dimensional calculation is captured as well. ($\bar{x}_{\mathrm{f,1D}} = 0.511$ mm in the one-dimensional calculation with $\alpha S = 11.2$ W/(cm^{3}K) value) compared to 0.52 mm in the two-dimensional simulation (see figure 5.4).
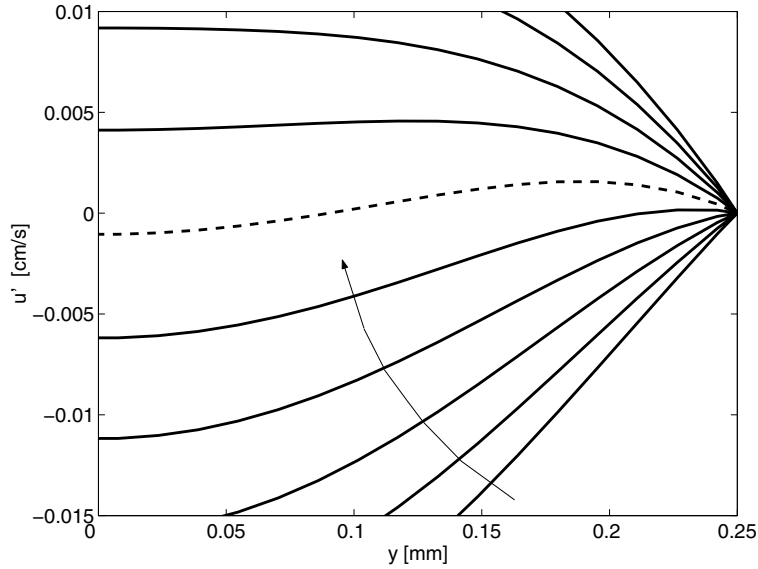
Figure 5.11: Velocity fluctuations at several phases in the centre of the burner plate ($x = -0.25$ mm). The dashed line corresponds to phase zero, with respect to inlet velocity fluctuations. The frequency (100 Hz) is near the resonance frequency of the similar one-dimensional flame with $\bar{u}_{\mathrm{u}} = 15$ cm/s and $\phi = 0.8$, and $d = 0.5$ mm.

5.3   Analysis of the unsteady micro-slit burner

There are reasons to expect that the acoustic behaviour of the micro-slit geometry also tends to the one-dimensional behaviour when $d \to 0$, and d/p is fixed. Contrary to the parabolic structure of the steady velocity field inside the burner, the fluctuations in the velocity in the slit depend on the ratio of unsteady and viscous forces, which is linear in the frequency of the perturbations. For low-frequency fluctuations, the flow slowly adapts following the parabolic flow profile (see section 3.2). The velocity fluctuations inside the burner-plate are not parabolic at 100 Hz, as shown in figure 5.11. The fluctuations in the mean flow slightly lag behind those in the boundary layer. The fluctuating enthalpy is quite different from the one-dimensional case. Figure 5.12 shows three phases in one cycle at 100 Hz, near the resonance frequency of the flame, with $\bar{u}_{\mathrm{u}} = 15$ cm/s, $\phi = 0.8$ and $d = 0.5$ mm. In these plots the one-dimensional simulation is shown as well. Clearly, the amplitude of the fluctuations are highest at the plate segments. The amplitude of the enthalpy fluctuations downstream is lower than in the one-dimensional case. The amplitude decreases for positions within the channel $0 < y < d/2$. It appears that the net contribution of the enthalpy fluctuations at $x = 0$ is lower for the perforated plate than for the one-dimensional flame. Figure 5.13 shows the enthalpy fluctuations as function of time at the flame front ($\bar{x}_{\mathrm{f,1D}} = 0.55$ mm and $\bar{x}_{\mathrm{f,2D}} = 0.519$ mm). The amplitude of the two-dimensional simulation is lower and shows a larger phase shift in comparison to the one-dimensional simulation ($d = 0$ mm). The variation in fluctuations along the y-axis are very small (within 3 percent of the global fluctuations) and the extra phase shift is

not caused by the difference in the stand-off distance. This means that the fluctuating two-dimensional flame is a flat flame as in the stationary case. The main difference with the one-dimensional flame is the change in the phase and amplitude in the enthalpy, as shown in figure 5.13.

The same decrease in amplitude and increase in phase shift is observed in the flame velocity u'_f, mass burning velocity s'_L, and gas velocity $u'(x_\mathrm{f,2D})$, as shown in figures 5.14 to 5.16. As expected, the mass burning velocity is in phase with the enthalpy fluctuations at the flame front. The limit of the transfer function for $d \to 0$ (with d/p fixed) for a reacting flow through a slit burner is also investigated. The influence of the contraction in the flow is small. In the previous chapter the influence of the porosity of the burner was neglected and this assumption is justified as shown in figure 5.17 for the $\bar{u}_\mathrm{u} = 15$ cm/s, $\phi = 0.8$ flame. The porosity in the one-dimensional simulations has a little effect on the response, in terms of the position of the resonance peak and the phase. A slight increase in the amplitude is observed, but for a porosity $d/p = 2/3$ this is about 10%. This means that the velocity fluctuations are homogeneous again before they reach the flame.

In figure 5.18, the transfer function of the velocity perturbations is shown for three two-dimensional calculations with fixed $d/p = 2/3$. The solid lines are the one-dimensional results. For large diameters, the resonance peak is lower and, for diameters close to zero, the phase of the response slightly differs from the one-dimensional situation: a larger time lag is present for high frequencies. Furthermore, the resonance peak shifts to lower frequencies when the diameter increases (d/p fixed). In the previous section it was demonstrated that a finite heat transfer coefficient was sufficient to explain the shift in the global stationary stand-off distance (for $d = 0.5$ mm we found that $\alpha S = 11.2$ W/(cm^{3}K)). Figure 5.19 shows the response in one-dimensional simulations for different values αS. It is clear that the resonance peak for $\alpha S = 11.2$ W/(cm^{3}K) would be too high (amplification factor is greater than 14) compared to the corresponding peak for $d = 0.5$ mm (dash-dotted line, amplification factor is about 12) in figure 5.18. For lower αS the resonance frequency does not match the frequencies found in the one-dimensional simulations as seen in figure 5.13.

Thus, the observed two-dimensional behaviour cannot be explained by the influence of global one-dimensional parameters like the porosity d/p and αS alone. The main difference between the one-dimensional and two-dimensional behaviour can likely be found in the change in enthalpy fluctuations.

5.4 Concluding discussion

The complexity of the flow through the burner plate does not allow for a simple analytical model, like the one derived in chapter 4. From the stationary analysis, we have seen that the enthalpy at $x > 0$ is far from constant, which is an essential assumption in the one-dimensional model. The non-constant enthalpy is also found in the unsteady simulations. However, the non-constant properties are restricted to a small area around the burner plate. From the simulations, it is shown that the variables are constant in y-direction (within a few percent) at the flame front position. For the observed perforation diameters,

the flame can be assumed to remain flat at the flame front position during motion.
An important difference is the position of the flame. The burner plate is not able to cool the
gas as effectively as in the one-dimensional case and the flame stabilises closer to the plate.
The one-dimensional simulations with a finite heat transfer coefficient αS show a lower
resonance peak. This effect should be incorporated in the model. However, using a finite
heat transfer in one-dimensional simulations does not resolve completely the decreased res-
onance frequency as observed in the two-dimensional case (cf. figures 5.18 (a) and 5.19 (a)).

In literature, little can be found on the analytical treatment of the two-dimensional
equations. Fleifil [17] does not use the flow equations, but makes rigorous assumptions
on the flow variables being homogeneous except at the flame front position. Therefore,
this work does not give insight into how to treat the equations for inhomogeneous flows.
McIntosh [32] investigated cellular instability of flames, in which the periodicity in y-
direction of the problem was used to solve two-dimensional effects (two-dimensional flame
structures with small wave numbers, where the burner plate is still one-dimensional). A
similar technique is applied to the micro-slit burner problem in appendix D to make an
attempt to model the acoustic behaviour of the burner-stabilised flame.
However, to solve the resulting equations, rigorous assumptions should be made on the
steady flow field and thickness of burner plate. These assumptions are questionable in
our configuration and, unfortunately, the resulting model does not explain the observed
decreasing resonance peaks.
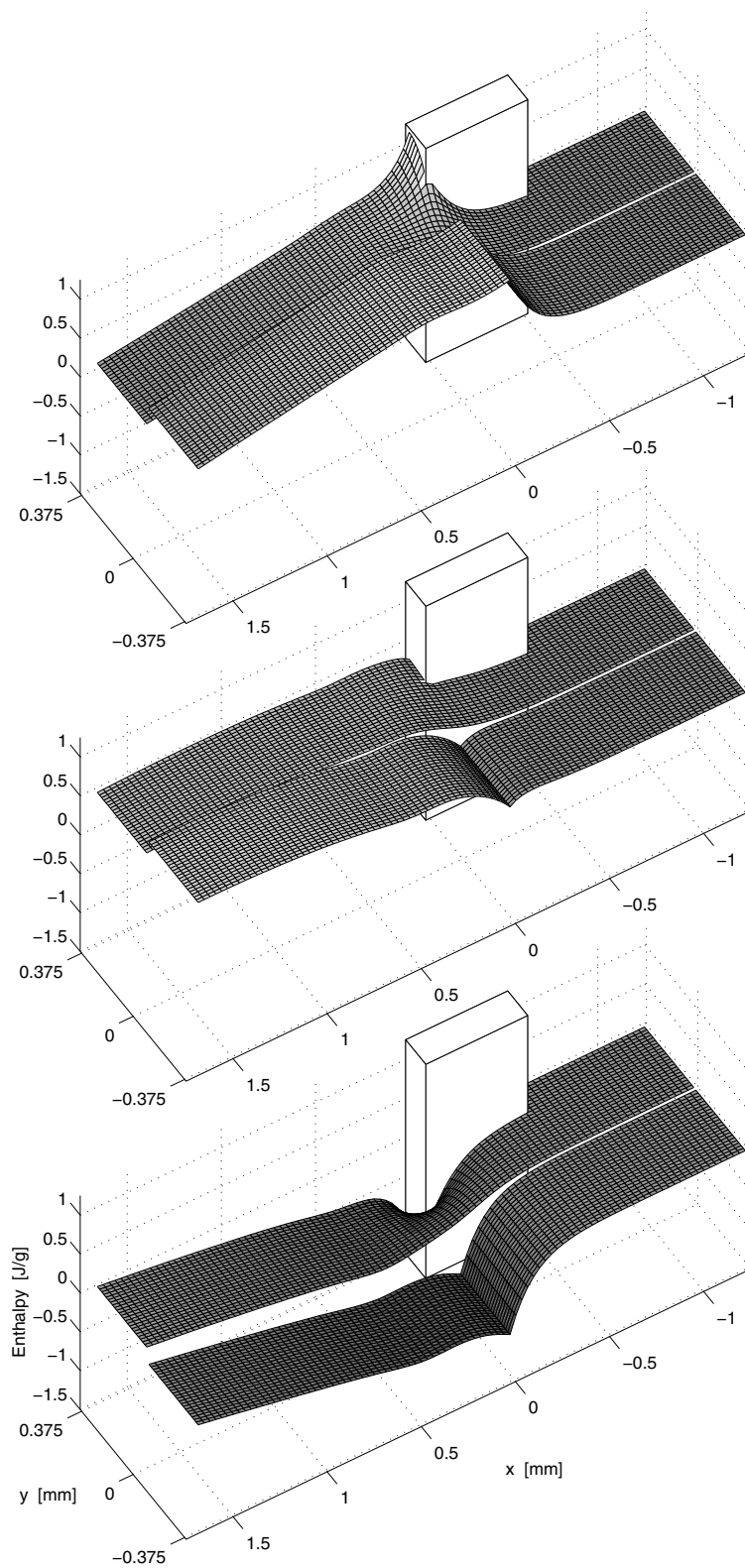
Figure 5.12: Fluctuating enthalpy in the perforated plate for $d = 0.5$ mm and $d = 0$ mm (the one-dimensional case) for three phases in one cycle.
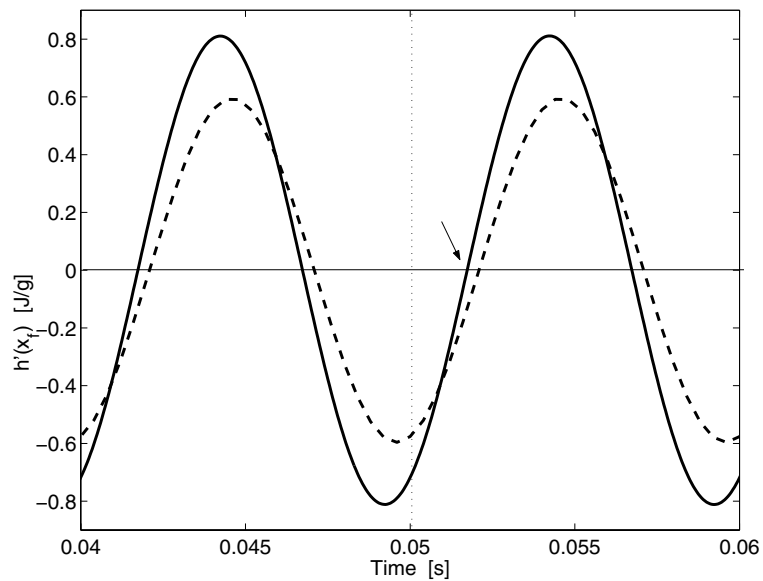
Figure 5.13: Enthalpy fluctuations at the flame front as function of time. Solid line: $d = 0$ mm and dashed line: $d = 0.5$ mm. Vertical dotted line denotes phase zero of the reference inlet velocity fluctuations. The arrow points to phase zero of the enthalpy fluctuations.
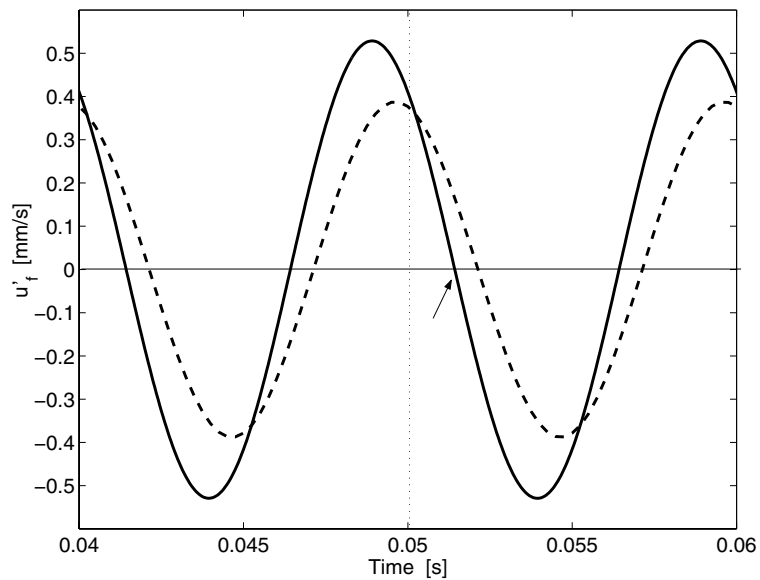
Figure 5.14: Flame velocity fluctuations at the flame front as function of time. Solid line: $d = 0$ mm and dashed line: $d = 0.5$ mm. The vertical dotted line denotes phase zero of the reference inlet velocity fluctuations. The arrow points to phase zero of the flame velocity fluctuations.
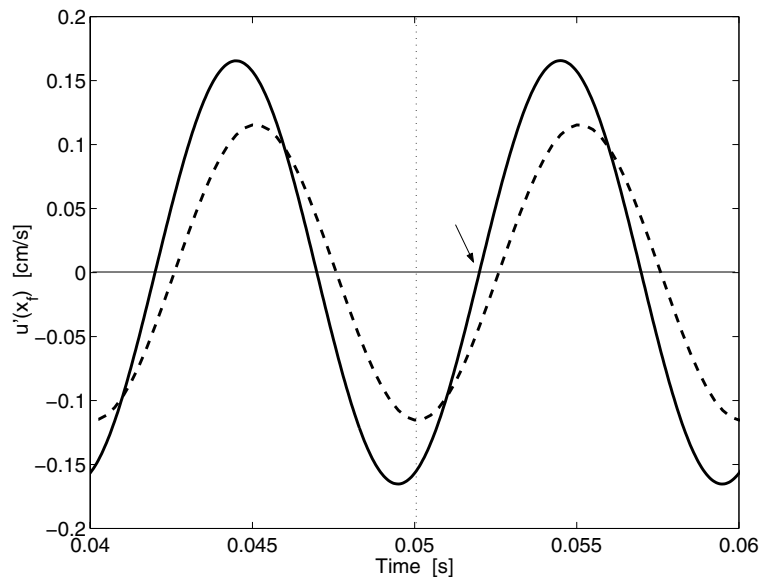
Figure 5.15: Vertical component of gas velocity fluctuations as function of time. Solid line: $d = 0$ mm and dashed line: $d = 0.5$ mm. The vertical dashed line denotes phase zero of the reference inlet velocity fluctuations. The arrow points to phase zero of the velocity fluctuations.
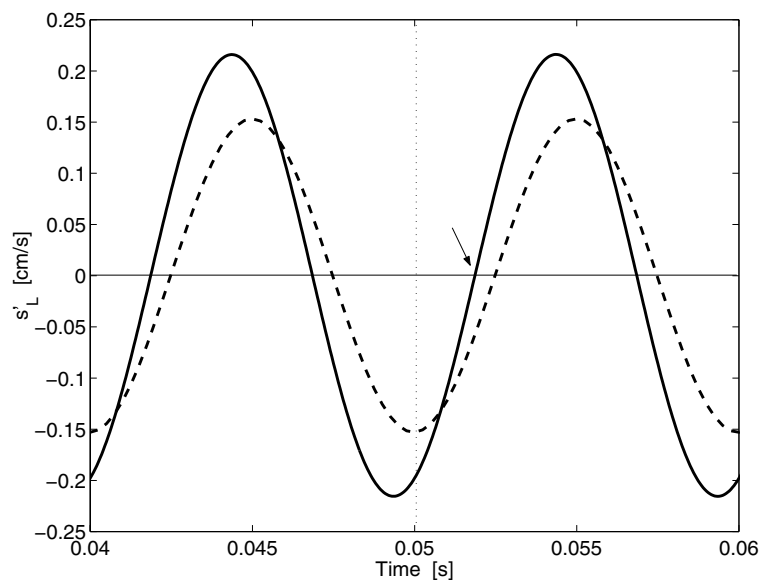
Figure 5.16: Vertical component of mass burning velocity fluctuations as function of time. Solid line: $d = 0$ mm and dashed line: $d = 0.5$ mm. The vertical dotted line denotes phase zero of the reference inlet velocity fluctuations. The arrow points to phase zero of the mass burning velocity fluctuations.

(a)   (b)
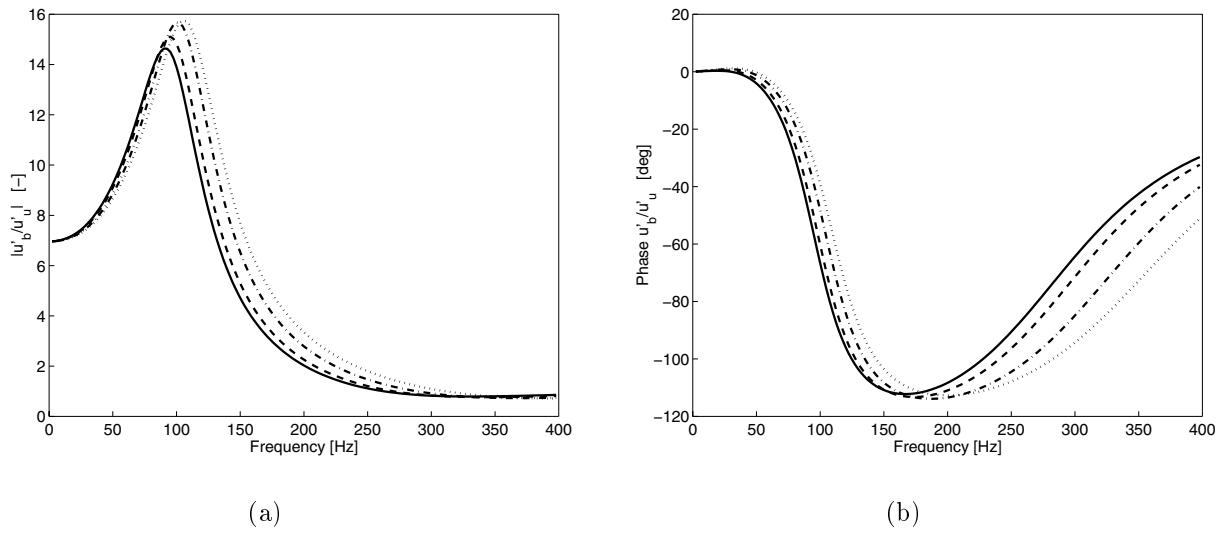
Figure 5.17: Amplitude (a) and phase (b) of the response of an ideally cooled one-dimensional burner-stabilised flame ($\phi = 0.8$, $\bar{u}_u = 15$ cm/s, and $\bar{T}_u = 298$ K), for several porosity values. Solid line: $d/p = 1$, dashed line: $d/p = 0.875$, dash-dotted line: $d/p = 0.8$, and dotted line: $d/p = 2/3$.

(a)   (b)
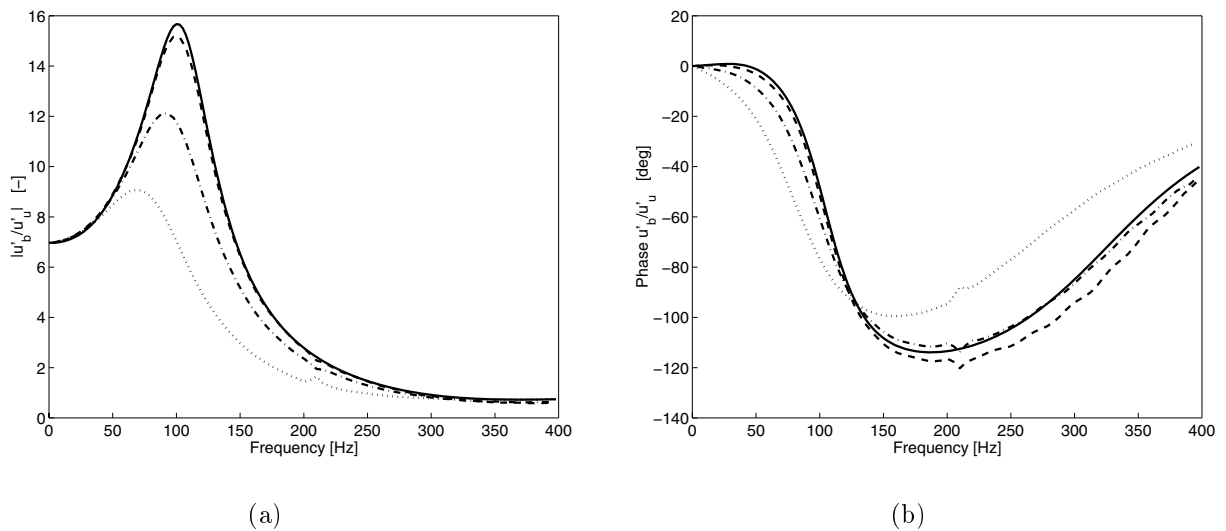
Figure 5.18: Amplitude (a) and phase (b) of response of the outlet velocity for different diameters (dotted line: $d = 1$ mm, dash-dotted line: $d = 0.5$ mm, dashed line: $d = 0.25$ mm and solid line: $d \rightarrow 0$.)
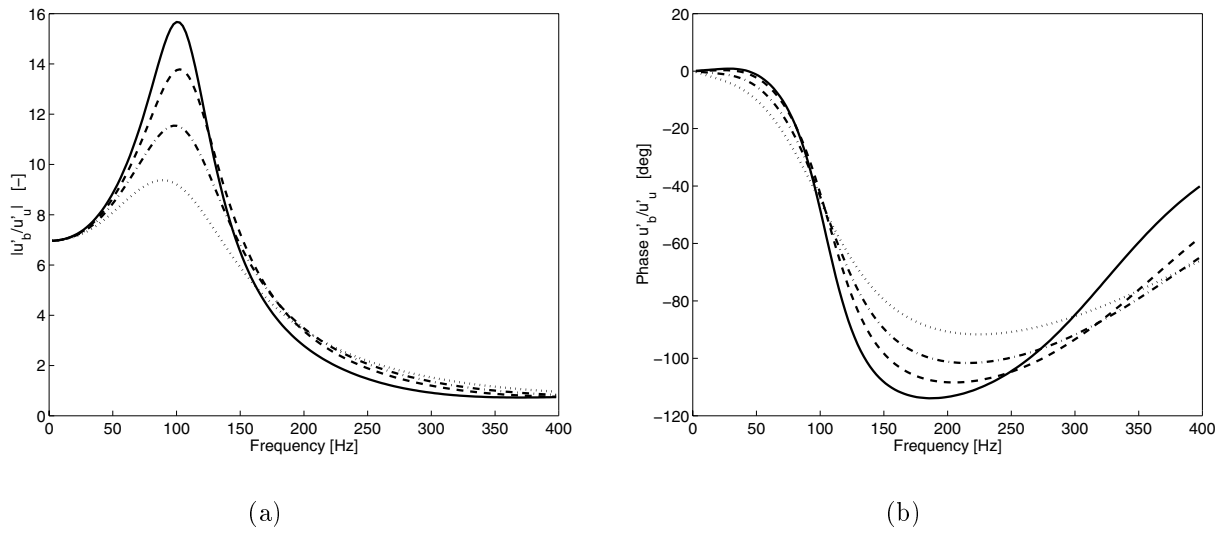
Figure 5.19: Amplitude (a) and phase (b) of the response of the downstream velocity with $\alpha S = \infty$ (solid line), $\alpha S = 5$ W/(cm^{3}s) (dashed line), $\alpha S = 3$ W/(cm^{3}s) (dash-dotted line) and $\alpha S = 1$ W/(cm^{3}s) (dotted line) for a one-dimensional flame with burner porosity $d/p = 2/3$.

Chapter 6

Concluding remarks

In the previous chapter it has been demonstrated that the surface burners, frequently used in central-heating boilers, produce almost one-dimensional flames. The diameter of the perforations in these burners should be chosen small enough in those cases. The choice of diameters pitch ratios in these surface burners is limited, because of flashback and blow off phenomena. It has been demonstrated by one-dimensional simulations that the burner plate has a small influence on the response: the magnitude and frequency of the resonance peak do not differ very much. So, the one-dimensional analytical model in chapter 4 can be used safely to investigate the acoustic behaviour in micro-slit burners. This model is used in the transfer matrix method to determine the acoustic stability of a simplified boiler with micro-slit (or flat) burners. This is presented at the end of this chapter. First, the mechanism for flame resonance is explained.

Mechanism to explain the acoustic behaviour

The mechanism of flame resonance is related to the coupling between the flame position and the heat loss to the burner. As the flame front moves, enthalpy fluctuations emerge at the burner surface, where the temperature is fixed and the mass fraction profile moves with the flame front. These enthalpy fluctuations propagate towards the flame front and are damped. Depending on the flame parameters and frequency, the phase between the enthalpy fluctuations at the flame front and those at the burner surface, can be $\pi/2$. Since the resulting flame temperature fluctuation is coupled to the mass burning rate, these fluctuations are in phase with the flame velocity. In this case the flame movement amplifies itself and shows a resonance peak in the acoustic transfer.
As practical burners do not have infinite conductivity, the burners heat up. The analytical model has been adapted for those cases and shows that the amplification at the resonance frequency is lower. Also the resonance frequency is higher for higher surface temperatures, because the flame stabilises closer to the burner and higher frequencies are needed to establish the $\pi/2$ phase difference.
For flames with increasing activation energies (equivalence ratios greater than 1), the flame may oscillate spontaneously without the presence of an acoustic field. The mechanism is
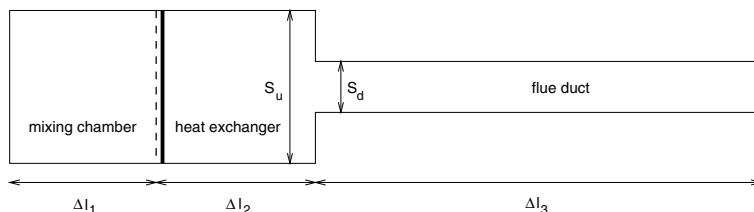
Figure 6.1: The simplified heating device, consisting of a mixing chamber, burner/flame, heat exchanger, and a flue duct. The system is considered one-dimensional and and does not have acoustic radiation losses to the surroundings.

equal to the one described above, but the movement induces temperature fluctuations at the flame front that result in mass burning rate fluctuations, of which the effects are greater than the damping effect in the enthalpy fluctuations. In this case, perturbations will grow in time. It is concluded that the lean methane/air flames used in this thesis are stable and resonance only occurs in combination with the acoustic system wherein they are present. From numerical simulations it was demonstrated that the response of the burner-stabilised flame differs when using detailed and global chemistry. This is mainly caused by the accuracy of the parameters in the global scheme. These parameters are fitted for the burning velocity and flame temperature in the steady-state situation. Qualitatively, both schemes predict all acoustic phenomena observed in the experimental setup.

Stability analysis of a simplified heating boiler

In section 4.2.3 the transfer function of a one-dimensional burner-stabilised flame was derived. Although a stable flame is not a source of sound, it can function as an amplifier in the heating device. Depending on the flame parameters, the flame can either absorb or produce acoustic energy. In case of a flame producing acoustic energy, a distortion is amplified to an acoustic field with large amplitudes. The amplitude in the acoustic field is bounded by the non-linear effects. If an acoustic element exists in the system that absorbs energy, the system is called stable if more energy is absorbed than is produced by the flame. Examples are acoustic radiation to the surroundings at the open ends, or the viscous dissipation in the tubes of the system.

Figure 6.1 shows a model of a simplified heating device. The elements in this system are distinguished as: a mixing chamber, a burner-stabilised flame, a heat exchanger, a flow contraction, and a flue duct. Δl denotes the length of a pipe segment, and S_d, S_u are the cross sectional surfaces. Two relations determine the stability of the system. The first relation is the frequency condition (cf. equation (4.56) for a free flame), which is satisfied for the resonance frequencies of the free system. The system is stable if the imaginary part of the (complex) frequency is positive: the eigensolution is damped in time, as shown in equation (2.40). The real part is the frequency at which the solution oscillates. In case of damping modes, the flame actually weakens the acoustic field. The frequency condition for the configuration in figure 6.1 is given by equation (2.42) with $Z_1 = 0$ (impedance for

Figure 6.2: The stability plot of the simple heating device, as function of the surface temperature T_{surf} and the frequency of the source. In the white regions, the system is potentially stable, whereas the dark regions the system is potentially unstable. The black lines represent three modes (resonance frequencies) of the system, solutions of equation (6.1).

an open end), which yields:

$$
\begin{aligned}
\tan(k\Delta l_1)\tan(k\sqrt{T_{\text{ub}}}\Delta l_3)\frac{S_{\text{u}}}{S_{\text{d}}}\sqrt{T_{\text{ub}}}\mathcal{V} + \\
\tan(k\sqrt{T_{\text{ub}}}\Delta l_2)\left[\tan(k\Delta l_1)\sqrt{T_{\text{ub}}}\mathcal{V} + \tan(k\sqrt{T_{\text{ub}}}\Delta l_3)\frac{S_{\text{u}}}{S_{\text{d}}}\right] - 1 = 0,
\end{aligned}
\tag{6.1}
$$

where $T_{\text{ub}} = \bar{T}_{\text{u}}/\bar{T}_{\text{b}}$, $k = \omega/\bar{c}_{\text{u}}$, and $\mathcal{V}$ is the transfer function of the velocity fluctuations by the flame. The second relation describes the energy production by the driving mechanism at the closed end of the system, but is complex and therefore left to the reader, because it does not add new insight to the matter.

In section 4.2.4 a model is derived for variable surface temperatures. It is interesting to know the effect of the surface temperature on the stability of the system. One of the problems related to central-heating systems is a cold startup. At startup many devices appear to be very noisy and sometimes they become stable after a while. The stability can be visualised by plotting the acoustic energy production as function of the frequency of the external force and the surface temperature. Figure 6.2 shows this stability plot. The values for the dimensions are $\Delta l_1 = 0.3$ m, $\Delta l_2 = 0.3$ m, $\Delta l_3 = 1.0$ m, $S_{\text{u}} = 0.3$ m, and $S_{\text{d}} = 0.06$ m. The other parameters are $T_{\text{ad}} = 2012.5$ K, $T_{\text{a}} = 2 \times 14412$ K (methane flame $\phi = 0.8$), $\bar{T}_{\text{u}} = 300$ K, $\bar{T}_{\text{b}} = 1836.4$ K, $\bar{u}_{\text{u}} = 15$ cm/s, $\bar{\lambda}_{\text{u}} = 2.75 \times 10^{-2}$ J/(K m s), $c_p = 1.286 \times 10^3$ J/(kg K), and $\bar{\rho}_{\text{u}} = 1.13170$ kg/m^3. This particular system is unstable for every burner type covered by the model. The first mode (37.4 Hz) is stable for surface
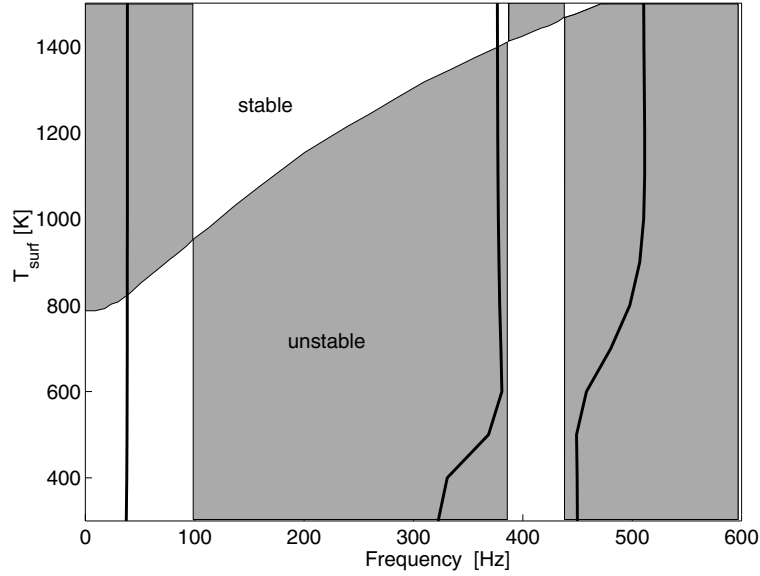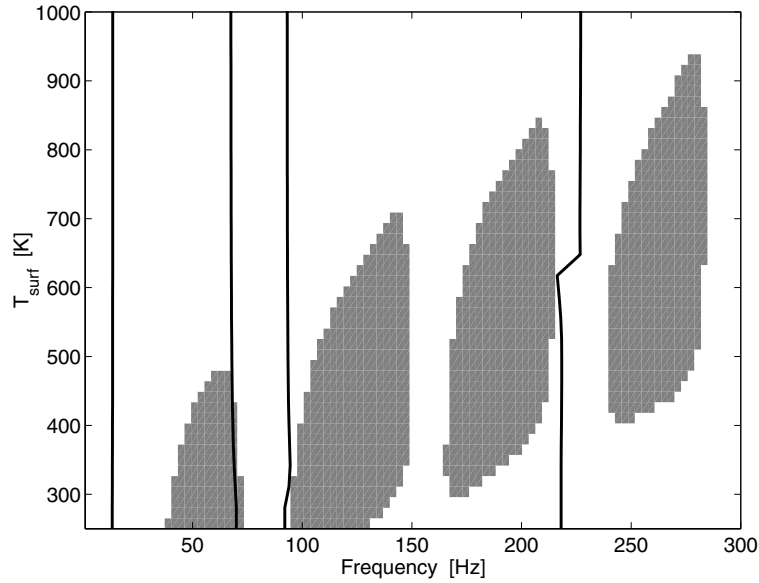
Figure 6.3: The stability plot of a real heating device, as function of the surface temperature T_{surf} and the frequency of the source. In the white regions, the system is potentially stable, whereas the the system is potentially unstable in the dark regions. The black lines represent the modes (resonance frequencies) of the system.

temperatures up to 800 K. For hotter surfaces, the amplitude of this mode will grow in time, and becomes unstable. The second and third modes are more troublesome. For realistic surface temperatures (up to 1200 K), these modes are in the unstable region. The absence of acoustic losses results in the obvious checkerboard appearance. If acoustic losses would be modelled, the regions of instabilities would become smaller, and from experience, the efficiency of the acoustic losses is greater for higher frequencies. In practice it mostly appears that the regions of instability are not present for frequencies higher than 500 Hz. Therefore, these results might not be representative for realistic heating devices. The cold start up phenomenon is not confirmed by figure 6.2 for the lowest mode. The temperature at the turning point (> 1350 K) for the other two modes is far too high for realistic surface temperatures. However, the result shows that surface temperature has a significant influence on the acoustic behaviour of the system. This interpretation above is quasi-steady, the question remains whether cold start up is such a process, of which stability can be abstracted from the stability plots.

Figure 6.3 shows the stability plot of a more realistic heating device [46], where acoustic losses such as friction and radiation were taken into account. Here, it can be seen that the regions of instability are much smaller. All modes, except the second one, are in the stable region. The second mode (at approximately 70 Hz) shows that, the device is unstable for surface temperature from room temperature to 500 K, which is an indication for a cold start up problem in this heating device.

The results from the transfer matrix method should be validated for this device by mea-

surements. Furthermore, parameters such as equivalence ratio, activation energy should be investigated for their influence on the acoustic behaviour of this particular heating device.

Appendix A

Matched asymptotics

Two areas can be distinguished: (1) the acoustic region and (2) the combustion area, as shown in figure A.1. The solutions in these regions match at the boundaries between the regions. In the next sections, we formally determine the leading-order flow equations in these regions, and make a connection between the combustion solution to the solution in the acoustic regions, wherein the burner/flame is situated.

Section A.6 derives the Zeldovich progress variable that simplifies the analyses considerably.

A.1   Combustion zone

The objective of this section is to give insight into the compressible Navier-Stokes equations for a reacting flow at low-Mach numbers, if the flow is affected by acoustic effects. In a burner-stabilised flat flame, we have a characteristic length scale L, let say the flame thickness, and a single-time scale: the time it takes for a particle to travel one length scale. Using an asymptotic analysis, based on single-length and time scales, the equations simplify considerably.

In the analysis, the global chemical behaviour of the mixture is modelled by a single reac-
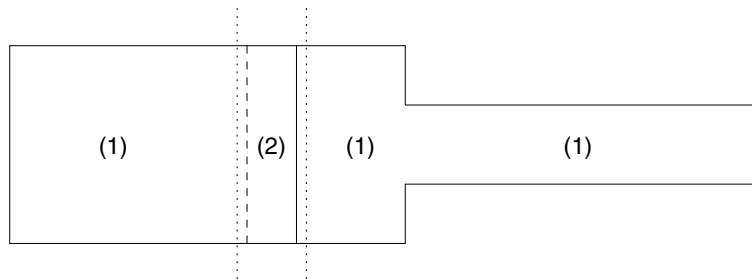

Figure A.1: Simplified boiler configuration, where the flow direction is from left to right. Separate regions are distinguished: (1) acoustic regions and (2) combustion area. The dotted lines denote the boundaries where the solutions are matched.

tion. Furthermore, we assume constant heat capacity $c_p = \bar{c}_p$, equal diffusion coefficients $D_{i\mathrm{m}} \equiv D$, and equal Lewis numbers:

$$Le_i = \frac{\lambda}{\bar{c}_p \rho D_{i\mathrm{m}}} \equiv Le. \tag{A.1}$$

In this case all species are functions of one product species Y and the transport of Y is described by:

$$\frac{\partial \rho Y}{\partial t} + \boldsymbol{\nabla} \cdot (\rho Y \boldsymbol{u}) + \boldsymbol{\nabla} \cdot (\rho \boldsymbol{U} Y) = \dot{\rho}, \tag{A.2}$$

with $\boldsymbol{U}$ the diffusion velocity of the species and $\dot{\rho}$ the production rate.

We introduce the reaction energy ΔH, for which the derivation can be found in detail in section A.6 for a one-step reaction scheme of methane combustion. Since combustion is an exothermic process, $\Delta H > 0$. In general, the energy of reaction depends on the initial and final compositions of the gas mixture. Equation (2.11), together with constant heat capacity, gives:

$$h = \Delta H\, Y + \bar{c}_p T, \tag{A.3}$$

where, for the sake of convenience, we choose $h_{\mathrm{b}} = \bar{c}_p T_{\mathrm{b}}$. The equation of state for a perfect gas is given by:

$$p = \rho R T, \tag{A.4}$$

with R the gas constant. From (2.4), (2.10), and (2.11), another thermodynamic relation is obtained:

$$p = (\gamma - 1)\rho(E - \frac{1}{2}|\boldsymbol{u}|^2 - \Delta H\, Y), \tag{A.5}$$

where $\gamma = c_p/c_v$ is the specific heat ratio.

The compressible flow equations (2.14), (2.17), (A.2), (A.4), and (A.5) are non-dimensionalised with respect to a reference state, denoted by the subscript ∞, e.g. far field or stagnation conditions in the unburnt zone. We non-dimensionalise the equations by using the reference quantities. A characteristic length scale L of the flow, which is in our case the diffusion length $D_{i\mathrm{m}}/u_\infty$, is introduced.

We define the dimensionless quantities by:

$$
\begin{aligned}
&\rho' = \frac{\rho}{\rho_\infty}, & &p' = \frac{p}{p_\infty}, & &\boldsymbol{u}' = \frac{\boldsymbol{u}}{u_\infty}, & &T' = \frac{T}{T_\infty}, \\
&\mu' = \frac{\mu}{\mu_\infty}, & &\lambda' = \frac{\lambda}{\lambda_\infty}, & &\boldsymbol{x}' = \frac{\boldsymbol{x}}{L}, & &t' = \frac{t}{L/u_\infty}, \\
&h' = \frac{h}{p_\infty/\rho_\infty}, & &E' = \frac{E}{p_\infty/\rho_\infty}, & &H' = \frac{H}{p_\infty/\rho_\infty}, & &\boldsymbol{U}' = \frac{\boldsymbol{U}}{D/L}, \\
&\dot{\rho}' = \dot{\rho}\,\frac{L}{\rho_\infty u_\infty}, & &\Delta H' = \frac{\Delta H}{p_\infty/\rho_\infty}.
\end{aligned}
\tag{A.6}
$$

The reference quantities are chosen such that the dimensionless flow quantities remain of order O(1) for any low reference Mach number:

$$M_\infty = \frac{u_\infty}{\sqrt{\gamma p_\infty/\rho_\infty}}. \tag{A.7}$$

To avoid the dependence on γ, we shall work with:

$$M = \sqrt{\gamma} M_\infty. \tag{A.8}$$

Note that

$$\frac{u}{\sqrt{p_\infty/\rho_\infty}} = \frac{u}{u_\infty} M \to 0 \qquad \text{for} \qquad M \to 0 \tag{A.9}$$

and

$$\frac{p}{\rho_\infty u_\infty^2} = \frac{p}{p_\infty}\frac{1}{M^2} \to \infty \qquad \text{for} \qquad M \to 0. \tag{A.10}$$

Using the relations (A.6) in the flow equations, we may write the dimensionless reacting-flow equations as follows (the primes are dropped):

$$\frac{\partial \rho Y}{\partial t} + \boldsymbol{\nabla} \cdot (\rho \boldsymbol{u} Y) + \frac{1}{Re_\infty Le_\infty Pr_\infty} \boldsymbol{\nabla} \cdot (\rho \boldsymbol{U} Y) \;=\; \dot{\rho}, \tag{A.11}$$

$$\frac{\partial \rho}{\partial t} + \boldsymbol{\nabla} \cdot (\rho \boldsymbol{u}) \;=\; 0, \tag{A.12}$$

$$\frac{\partial \rho \boldsymbol{u}}{\partial t} + \boldsymbol{\nabla} \cdot (\rho \boldsymbol{u} \otimes \boldsymbol{u}) + \frac{1}{M^2} \boldsymbol{\nabla} p \;=\; \boldsymbol{G}, \tag{A.13}$$

$$\boldsymbol{U} \;=\; -\frac{1}{Y} \boldsymbol{\nabla} Y, \tag{A.14}$$

where $\boldsymbol{G} = -1/Re_\infty \boldsymbol{\nabla} \cdot \bar{\bar{\boldsymbol{\tau}}} + (1/Fr_\infty^2)\rho(-\boldsymbol{e}_r)$, $Re_\infty = \rho_\infty u_\infty L/\mu_\infty$ is the Reynolds number, $Fr_\infty = U_\infty/\sqrt{gL}$ is the Froude number, $Pr_\infty = \mu_\infty \bar{c}_p/\lambda_\infty$ is the Prandtl number, and $Le = \lambda_\infty/\bar{c}_p\rho_\infty D_{\text{im}}$. Also,

$$\frac{\partial \rho E}{\partial t} + \boldsymbol{\nabla} \cdot (\rho H \boldsymbol{u}) = Q \tag{A.15}$$

with

$$Q = -\frac{M^2}{Re_\infty}\boldsymbol{\nabla} \cdot (\bar{\bar{\boldsymbol{\tau}}} \cdot \boldsymbol{u}) + \frac{M^2}{Fr_\infty^2}\rho(-\boldsymbol{e}_r) \cdot \boldsymbol{u}$$

$$+ \left(\frac{\gamma}{\gamma - 1}\right)\frac{1}{Re_\infty Fr_\infty}\boldsymbol{\nabla} \cdot (\lambda \boldsymbol{\nabla} T) + \frac{1}{Re_\infty Pr_\infty Le_\infty}\boldsymbol{\nabla} \cdot (\rho \Delta H \, \boldsymbol{\nabla} Y),$$

where $\boldsymbol{e}_r$ is a unit vector in the direction of the gravitational field. Assuming $Pr = c_p\mu/\lambda = Pr_\infty$, we obtain $\lambda/\lambda_\infty = \mu/\mu_\infty$, or $\lambda' = \mu'$.

The dimensionless expressions of the total enthalpy per unit mass and the total energy are:

$$H \;=\; h + M^2\frac{1}{2}|\mathbf{u}|^2, \tag{A.16}$$

$$E \;=\; H - \frac{p}{\rho}. \tag{A.17}$$

The dimensionless equations of state for a perfect gas read:

$$p \;=\; \rho T, \tag{A.18}$$

$$h \;=\; \Delta H\, Y + \frac{\gamma}{\gamma - 1}T. \tag{A.19}$$

Using equations (A.5), (A.16) to (A.19), we may express the pressure in terms of the conservative variables ρ, ρY, $\rho\boldsymbol{u}$ and ρE by:

$$p = (\gamma - 1)\left[\rho E - M^2\frac{1}{2}\frac{|\rho\boldsymbol{u}|^2}{\rho} - \Delta H\,\rho Y\right]. \tag{A.20}$$

In single-time scale, single-space scale low Mach number asymptotic analysis, each flow variable is written as a series expansion, e.g. the pressure:

$$p(\boldsymbol{x}, t, M) = p_0(\boldsymbol{x}, t) + Mp_1(\boldsymbol{x}, t) + M^2 p_2(\boldsymbol{x}, t) + \mathrm{O}(M^3). \tag{A.21}$$

The expansions are substituted into the dimensionless governing equations and we can divide the equations into orders of Mach number. The leading-order continuity equation reads:

$$\frac{\partial \rho_0}{\partial t} + \boldsymbol{\nabla} \cdot (\rho\boldsymbol{u})_0 = 0, \tag{A.22}$$

and similarly, the leading-order species equation:

$$\frac{\partial(\rho Y)_0}{\partial t} + \boldsymbol{\nabla} \cdot (\rho\boldsymbol{u}Y)_0 - \frac{1}{Re_\infty Pr_\infty Le_\infty}\boldsymbol{\nabla} \cdot (\rho\boldsymbol{\nabla}Y)_0 = \dot{\rho}_0. \tag{A.23}$$

By expanding the density ρ, we obtain the relations $(\rho\mathbf{u})_0 = \rho_0\mathbf{u}_0$, $(\rho\mathbf{u})_1 = \rho_1\mathbf{u}_0 + \rho_0\mathbf{u}_1$ and $(\rho\mathbf{u})_2 = \rho_2\mathbf{u}_0 + \rho_1\mathbf{u}_1 + \rho_0\mathbf{u}_2$.

The leading-, first- and second-order momentum equation are given by:

$$\boldsymbol{\nabla}p_0 \;=\; 0, \tag{A.24}$$

$$\boldsymbol{\nabla}p_1 \;=\; 0, \tag{A.25}$$

$$\frac{\partial(\rho\boldsymbol{u})_0}{\partial t} + \boldsymbol{\nabla} \cdot (\rho\boldsymbol{u} \otimes \boldsymbol{u})_0 + \boldsymbol{\nabla}p_2 \;=\; \boldsymbol{G}_0, \tag{A.26}$$

with $\boldsymbol{G}_0 = 1/Re_\infty \boldsymbol{\nabla} \cdot \bar{\bar{\boldsymbol{\tau}}}_0 + (1/Fr_\infty^2)\rho(-\boldsymbol{e}_r)$. The leading-order energy equation yields:

$$\frac{\partial(\rho E)_0}{\partial t} + \boldsymbol{\nabla} \cdot (\rho H \boldsymbol{u})_0 = Q_0 \tag{A.27}$$

with

$$Q_0 = \left(\frac{\gamma}{\gamma - 1}\right) \frac{1}{Re_\infty Pr_\infty} \boldsymbol{\nabla} \cdot (\lambda \boldsymbol{\nabla} T)_0 + \frac{\Delta H}{Re_\infty Pr_\infty Le_\infty} \boldsymbol{\nabla}(\rho \boldsymbol{\nabla} Y)_0. \tag{A.28}$$

Since the work done by the viscous and buoyancy forces is of order $\mathrm{O}(M^2)$, the leading-order energy source term Q_0 is governed by heat-conduction and heat release rate only and the Prandtl number Pr_∞ is of order $\mathrm{O}(1)$ and the Froude number squared Fr_∞^2 is of order $\mathrm{O}(Re_\infty Pr_\infty)$, provided that the ratio $(\gamma - 1)/\gamma$ is of order $\mathrm{O}(1)$ in both cases. However, if the Reynolds number Re_∞ is of order $\mathrm{O}(M^2)$, i.e. the reference pressure p_∞ is of order of the viscous force per unit area $\mathrm{O}(\mu_\infty u_\infty/L)$, or if the Froude number Fr_∞ is of order $\mathrm{O}(M)$, i.e. the reference pressure p_∞ is of the order of the hydrostatic pressure $\mathrm{O}(\rho_\infty gL)$, then the work done by the viscous or buoyancy forces, respectively, will also contribute to the leading-order energy source term Q_0. The reaction rate $\dot{\rho}$ is assumed to be $\mathrm{O}(1)$, provided that the mass flow is $\mathrm{O}(1)$.

For the equation of state, the asymptotic expansion yields:

$$\begin{aligned} p_0 &= (\gamma - 1)((\rho E)_0 - \Delta H (\rho Y)_0), & \text{(A.29)} \\ T_0 &= \frac{p_0}{\rho_0}. & \text{(A.30)} \end{aligned}$$

The low-Mach number equations for a reacting flow are governed by the leading-order continuity (A.22), species (A.23) and energy (A.27) equations, together with the second-order momentum equation (A.26) and the leading-order equations of state (A.29) and (A.30).

This analysis shows that certain terms in the governing equations may be neglected to obtain the so-called Combustion Approximation. These equations describe also the 'acoustic' properties of the flame. The acoustic field outside the burner/flame region is analysed in the next section.

A.2 Acoustic zone

Following the general idea of sources being placed in an acoustic field, this section considers the source as a point in a multi-dimensional medium. Other configurations, like line sources or pulsating spheres etc., are a superposition of these point sources. The goal of this section is to recover the wave equation from the equations.

At large distances from the point source (order M^{-1} in terms of the characteristic flame thickness), it is considered that an acoustic field is present. Thus, we write:

$$\hat{\boldsymbol{x}} = M\boldsymbol{x}, \tag{A.31}$$

to scale the acoustic zone to the characteristic length in the compact zone. Time is not rescaled, since for large wave lengths, a typical unit of time can be considered to be comparable to L/u_0, where L is the characteristic flame length and u_0 is the steady flow velocity [33]. A typical frequency for these conditions could be in the region of 200 Hz. We define all quantities as series expansions in Mach number:

$$\phi(\hat{\boldsymbol{x}}, t) = \phi_0(\hat{\boldsymbol{x}}, t) + M\phi_0(\hat{\boldsymbol{x}}, t) + M^2\phi_0(\hat{\boldsymbol{x}}, t), \tag{A.32}$$

which are substituted in equations (A.11), (A.12), (A.13), (A.15) and (A.19). The leading-order equations yield:

$$\frac{\partial(\rho Y)_0}{\partial t} = 0, \tag{A.33}$$

$$\frac{\partial \rho_0}{\partial t} = 0, \tag{A.34}$$

$$\hat{\boldsymbol{\nabla}} p_0 = 0, \tag{A.35}$$

$$\frac{\partial(\rho E)_0}{\partial t} = 0, \tag{A.36}$$

$$p_0 = \rho_0 T_0, \tag{A.37}$$

This means that $\rho_0 = \rho_0(\hat{\boldsymbol{x}})$, $Y_0 = Y_0(\hat{\boldsymbol{x}})$ and constant p_0, since $p_0 = (\gamma - 1)((\rho E)_0 - \Delta H (\rho Y)_0)$ and, via the gas law (A.37), we have $T_0 = T_0(\hat{\boldsymbol{x}})$.
The first-order equations yield:

$$\frac{\partial(\rho Y)_1}{\partial t} + \hat{\boldsymbol{\nabla}} \cdot (\rho \boldsymbol{u} Y)_0 = 0, \tag{A.38}$$

$$\frac{\partial \rho_1}{\partial t} + \hat{\boldsymbol{\nabla}} \cdot (\rho \boldsymbol{u})_0 = 0, \tag{A.39}$$

$$\frac{\partial(\rho \boldsymbol{u})_0}{\partial t} + \hat{\boldsymbol{\nabla}} p_1 = 0, \tag{A.40}$$

$$\frac{\partial(\rho E)_1}{\partial t} + \hat{\boldsymbol{\nabla}}(\rho H \boldsymbol{u})_0 = 0, \tag{A.41}$$

$$p_1 = \rho_1 T_0 + \rho_0 T_1. \tag{A.42}$$

Equation (A.38) describes the convection of species and (A.39) the continuity equation. With use of the leading-order relations we have:

$$\frac{\partial u_0}{\partial t} + \frac{1}{\rho_0}\hat{\boldsymbol{\nabla}} p_1 = 0, \tag{A.43}$$

$$\frac{\partial p_1}{\partial t} + \gamma p_0 \hat{\boldsymbol{\nabla}} \cdot \boldsymbol{u}_0 = 0, \tag{A.44}$$

which are the wave equations. These equations can be combined to $(\partial/\partial t \times$ (A.44) $- \gamma p_0 \hat{\boldsymbol{\nabla}} \times$ (A.43)):

$$\frac{\partial^2 p_1}{\partial t^2} - \hat{\boldsymbol{\nabla}} \cdot (c_0^2 \hat{\boldsymbol{\nabla}} p_1) = 0, \tag{A.45}$$

with $c_0 = \sqrt{\gamma p_0/\rho_0}$, the leading-order speed of sound. Note that c_0 is a function of $\hat{\boldsymbol{x}}$. The work done by the viscous and buoyancy forces does not affect the first-order pressure p_1, unless conditions $Re = \mathrm{O}(M^2)$ or $Fr = \mathrm{O}(M)$, respectively, hold.

If the leading-order speed of sound c_0 is approximated by the ambient speed of sound c_∞ (with the ambient chosen as reference state), equation (A.45) is the basic equation of acoustics to describe propagating pressure disturbances.

A matching procedure connects the leading-order quantities in the acoustic field to the leading-order quantities in the burner/flame region. This procedure is presented in the next section.

A.3 Matching principle

In the previous section we determined the flow equations in the acoustic zone and the burner/flame area. The solutions in these zones must be matched in order to obtain a general solution up to a certain accuracy. The values are matched by the principles of matched asymptotic expansions (Van Dyke [56]). For a one-dimensional flow problem (assuming that the solution is only dependent on x), it can be shown that the following matching conditions must apply on the upstream side of the burner/flame region:

$$
\begin{align}
Y_0^c(-\infty, t) &= Y_0^a, \tag{A.46} \\
p_0^c(t) &= p_0^a, \tag{A.47} \\
u_0^c(-\infty, t) &= u_0^a(0, t), \tag{A.48} \\
p_1^c(t) &= p_1^a(0, t), \tag{A.49} \\
T_0^c(-\infty, t) &= T_0^a(0), \tag{A.50} \\
\rho_0^c(-\infty, t) &= \rho_0^a(0), \tag{A.51}
\end{align}
$$

and the gradients:

$$
\left.\frac{\partial Y_0^c}{\partial x}\right|_{-\infty} = \left.\frac{\partial p_1^c}{\partial x}\right|_{-\infty} = \left.\frac{\partial u_0^c}{\partial x}\right|_{-\infty} = \left.\frac{\partial T_0^c}{\partial x}\right|_{-\infty} = 0, \tag{A.52}
$$

where superscript c denotes values in the burner/flame region, and a those in the acoustic region.

In exactly the same way, matching conditions are applied on the downstream side ($x = +\infty$) of the combustion zone. Together, they form a uniform solution; i.e. the inner-solution in the burner/flame region smoothly changes into the outer-solution in the acoustic region for low Mach numbers.

This illustrates that solutions of the acoustic equations and the combustion equations are related mathematically in a strictly defined way. We investigate the two regions separately. In the acoustic region, the first-order velocity and pressure fluctuations satisfy (A.43) and (A.44), and are obtained analytically. Via the matching principle, these solutions are used in the numerical simulations, where they serve as fluctuating boundary conditions. More

precisely, the leading-order velocity u_0^c is prescribed at the boundary of the numerical domain. The other quantities are constant at that boundary.

All the results are considered to be of leading-order (in Mach number) accuracy, so, for higher order effects you either have to leave the low-Mach number formulation and include a set of higher order equations, or solve the full set of flow equations with the variable pressure.

A.4   Transfer matrix for a compact source

In the previous section, the velocity, pressure, and temperature in the acoustic and the compact zone are coupled for a one-dimensional configuration. Since at low Mach numbers the pressure p_1 is an independent variables, the coupling of the pressure fluctuations on both sides of the flame is unity and the coupling between the velocity fluctuations is a function independent of the pressure, but can still be dependent on the temperature or density fluctuations. In fact, more quantities should be included in the acoustic field: the density and all the mass fractions.

As mentioned in section 3.2, the constraint equation is almost a divergence free velocity constraint $\partial u_0 / \partial x = 0$. With the remark that in the one-dimensional case, the momentum equation uncouples, a set of wave equations for the density, enthalpy, and mass fractions can be defined. All these quantities are constant along lines $\mathrm{d}x/\mathrm{d}t = u_0$. Therefore, density and mass fraction fluctuations emerging from the flame should be matched to the fluctuating quantities in the acoustic zones. Also, density or mixture variations could be present on the unburnt side of the flame.

For a low-Mach number flow, we define the following eight-pole coupling between the acoustic fields, using the dimensionless quantities:

$$
\begin{bmatrix} p_1^{'\mathrm{a}} \\ u_0^{'\mathrm{a}} \\ \rho_0^{'\mathrm{a}} \\ Y_0^{'\mathrm{a}} \end{bmatrix}_{\mathrm{unburnt}}
=
\begin{bmatrix} T_{11} & T_{12} & T_{13} & T_{14} \\ T_{21} & T_{22} & T_{23} & T_{24} \\ T_{31} & T_{32} & T_{33} & T_{34} \\ T_{41} & T_{42} & T_{43} & T_{44} \end{bmatrix}
\begin{bmatrix} p_1^{'\mathrm{a}} \\ u_0^{'\mathrm{a}} \\ \rho_0^{'\mathrm{a}} \\ Y_0^{'\mathrm{a}} \end{bmatrix}_{\mathrm{burnt}} .
\tag{A.53}
$$

The exact expressions for the elements T_{ij} are obtained from the Rankine-Hugoniot equations for a reacting flow in an infinitely thin region (compact zone). Integration of equations (A.22), (A.23), (A.25), and (A.27) for the one-dimensional case gives:

$$
[(\rho u)_0]_{-\infty}^{\infty} = 0, \tag{A.54}
$$

$$
[p_1]_{-\infty}^{\infty} = 0, \tag{A.55}
$$

$$
\left[(\rho u Y)_0 - \frac{1}{Re_\infty Pr_\infty Le_\infty} \left(\rho \frac{\partial Y}{\partial x} \right)_0 \right]_{-\infty}^{\infty} = \int_{-\infty}^{\infty} \dot{\rho}\, \mathrm{d}x \equiv -\frac{Q_{\mathrm{rel},0}}{\Delta H}, \tag{A.56}
$$

$$
\left[(\rho u H)_0 - \frac{\Delta H}{Re_\infty Pr_\infty Le_\infty} \left(\rho \frac{\partial Y}{\partial x} \right)_0 \right]_{-\infty}^{\infty} = \left(\frac{\gamma}{\gamma - 1} \right) \frac{1}{Re_\infty Pr_\infty} \int_{-\infty}^{\infty} \frac{\partial}{\partial x} \left(\lambda \frac{\partial T}{\partial x} \right)_0 \mathrm{d}x
$$
$$
\equiv -Q_{\mathrm{bur},0}, \tag{A.57}
$$

where we conveniently assume that no temperature gradients are present at $x = \infty$. This is an important assumption that is explained in the following.

By using the definition for H_0, the gas law, and substituting (A.56) in (A.57) gives a simple relation that connects the velocity fluctuations to the heat production in a burner-stabilised flame:

$$p_0 \frac{\gamma}{\gamma - 1} [u_0]_{-\infty}^{\infty} = Q_{\mathrm{rel},0} - Q_{\mathrm{bur},0} \tag{A.58}$$

Linearisation of equations (A.54) to (A.57) determines the elements in the transfer matrix. However, a 2x2 matrix connecting the pressure and the velocity fluctuations is sufficient if two additional assumptions are made. First, the linearised equation (A.54), which relates the density fluctuations on both sides of the flame (in short notation):

$$\bar{\rho}_{\mathrm{u}} u_{\mathrm{u}}' + \rho_{\mathrm{u}}' \bar{u}_{\mathrm{u}} = \bar{\rho}_{\mathrm{b}} u_{\mathrm{b}}' + \rho_{\mathrm{b}}' \bar{u}_{\mathrm{b}}, \tag{A.59}$$

The (constant) leading-order density in the acoustic zone implies $u_{\mathrm{b}}'/u_{\mathrm{u}}' = \bar{\rho}_{\mathrm{u}}/\bar{\rho}_{\mathrm{b}}$ and together with (A.58) states that fluctuating heat production of the burner/flame is proportional to the fluctuating velocity:

$$\left(\frac{\gamma}{\gamma - 1} \right) p_0 \left(\frac{\bar{T}_{\mathrm{b}}}{\bar{T}_{\mathrm{u}}} - 1 \right) u_{\mathrm{u}}' = Q_{\mathrm{rel}}' - Q_{\mathrm{bur}}'. \tag{A.60}$$

This is true if there is no mean flow present. In fact, the burner/flame generates density fluctuations that propagate towards the burnt side. Therefore, it is assumed that the density fluctuations vanish by diffusion (it can be shown that the temperature gradients in the constraint provides a diffusion term in the wave equation for the density) before they reach the adjoining element in the acoustic zone (cf. the equilibrium zone in the theory of McIntosh in section C.2). So, the density variations in the burner/flame do not influence the acoustic system. Secondly, it is assumed that the contents in unburnt gas mixture does not vary and that the reactions take place in the compact zone only. Thus, the acoustic system is independent on fluctuations of the mass fractions.

By taking the two assumptions into consideration, the transfer of the burner-stabilised flame is described by a 2x2 matrix:

$$T^{\mathrm{burner/flame}} = \left[\begin{array}{cc} 1 & 0 \\ 0 & \mathcal{V}^{-1} \end{array} \right], \tag{A.61}$$

where $\mathcal{V}$ is a frequency dependent function. Note that for low frequencies the damped density assumption does not hold and the influence of varying density on the pressure and velocity fields depends on the way adjoining acoustic elements couples density (or entropy) to the sound waves. In gas turbines, this coupling is an important mechanism in the acoustic system [27].
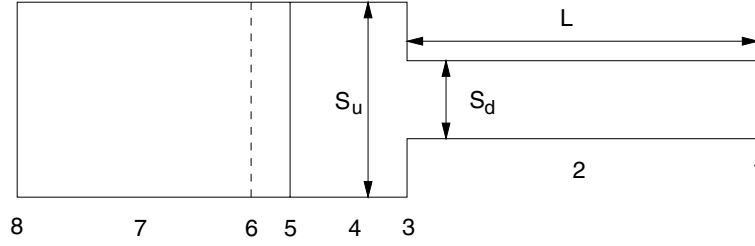
Figure A.2: Simple configuration of a heating system divided into 8 elements.

A.5   Elementary transfer matrices

The derivation of the transfer function of other acoustic elements than the burner/flame system (A.61) will be discussed here. First, the acoustic field is determined in an inviscous stationary medium. In such a medium the pressure and velocity fluctuations satisfy the classical linear one-dimensional wave equations in a stagnant flow:

$$\rho_0 \frac{\partial u'}{\partial t} + \frac{\partial p'}{\partial x} = 0, \tag{A.62}$$

$$\frac{\partial \rho'}{\partial t} + \rho_0 \frac{\partial u'}{\partial x} = 0, \tag{A.63}$$

from which the density is eliminated, yielding:

$$\left[\frac{\partial^2}{\partial t^2} - c_0^2 \frac{\partial^2}{\partial x^2} \right] p' = 0, \qquad \text{with } c_0^2 = \left. \frac{\partial p}{\partial \rho} \right|_s, \tag{A.64}$$

where the derivative in the second expression is taken at constant entropy s. These equations can be obtained using the low-Mach number approximation, as described in section A.2 of the appendix. The fluctuating pressure becomes, neglecting mean flow effects:

$$p'(x,t) = C_1 \exp \left[i\omega(t - \frac{x}{c_0}) \right] + C_2 \exp \left[i\omega(t + \frac{x}{c_0}) \right], \tag{A.65}$$

for which a harmonic time dependence $\exp(i\omega t)$ is assumed. The solution (A.65) represents a superposition of two propagating waves with amplitudes C_1 and C_2 moving in opposite directions with velocity c_0. Equation (A.65) can be rewritten to

$$p'(x,t) = [C_1 \exp(-ik_0 x) + C_2 \exp(ik_0 x)] \exp(i\omega t), \tag{A.66}$$

where $k_0 = \omega/c_0 = 2\pi/\lambda$, k_0 is the wave number of propagation, and λ is the wavelength. From equation (A.62) and using equation (A.66) we obtain the fluctuating velocity:

$$u'(x,t) = \frac{1}{Z_0} [C_1 \exp(-ik_0 x) - C_2 \exp(ik_0 x)] \exp(i\omega t), \tag{A.67}$$

where $Z_0 = \rho_0 c_0$ is the characteristic impedance of the medium.
Upon making use of the wave relations (A.66) and (A.67), a relation can be derived between

the acoustic field $(p_{\mathrm{r}}', u_{\mathrm{r}}')$ at a distance L from the point where the field is given by $(p_{\mathrm{l}}', u_{\mathrm{l}}')$. Assume that position l is located at $x = 0$ and the acoustic field at that location is written as:

$$
\begin{aligned}
p_{\mathrm{l}}' &= A + B, \\
u_{\mathrm{l}}' &= (A - B)/Z_0,
\end{aligned}
$$

with $A = C_1 \exp(\mathrm{i}\omega t)$ and $B = C_2 \exp(\mathrm{i}\omega t)$. The acoustic field at $x = L$ is then equal to:

$$
\begin{aligned}
p_{\mathrm{r}}' &= A \exp(-\mathrm{i}k_0 L) + B \exp(\mathrm{i}k_0 L) \\
&= [(A + B)\cos(k_0 L) - \mathrm{i}(A - B)\sin(k_0 L)] \\
&= [p_{\mathrm{l}}'\cos(k_0 L) - \mathrm{i}Z_0 u_{\mathrm{l}}'\sin(k_0 L)], \qquad\qquad (A.68) \\
u_{\mathrm{r}}' &= [A \exp(-\mathrm{i}k_0 L) - B \exp(\mathrm{i}k_0 L)] \\
&= [\frac{A - B}{Z_0}\cos(k_0 L) - \mathrm{i}\frac{A + B}{Z_0}\sin(k_0 L)] \\
&= [u_{\mathrm{l}}'\cos(k_0 L) - \mathrm{i}\frac{p_{\mathrm{l}}'}{Z_0}\sin(k_0 L)], \qquad\qquad (A.69)
\end{aligned}
$$

which can be written in the matrix form:

$$
\begin{bmatrix} p_{\mathrm{l}}' \\ u_{\mathrm{l}}' \end{bmatrix} = \begin{bmatrix} \cos(k_0 L) & \mathrm{i}Z_0\sin(k_0 L) \\ \frac{\mathrm{i}}{Z_0}\sin(k_0 L) & \cos(k_0 L) \end{bmatrix} \begin{bmatrix} p_{\mathrm{r}}' \\ u_{\mathrm{r}}' \end{bmatrix}. \qquad\qquad (A.70)
$$

This is the transfer matrix for a tube of length L.

For a sudden contraction in a medium without mean flow, we have the following transfer matrix, Munjal [41]:

$$
\begin{bmatrix} p_{\mathrm{l}}' \\ u_{\mathrm{l}}' \end{bmatrix} = \begin{bmatrix} 1 & 0 \\ 0 & \frac{S_{\mathrm{d}}}{S_{\mathrm{u}}} \end{bmatrix} \begin{bmatrix} p_{\mathrm{r}}' \\ u_{\mathrm{r}}' \end{bmatrix}, \qquad\qquad (A.71)
$$

where S_{d} is the cross sectional area of the small tube and S_{u} is the cross section of the other tube, as shown in figure A.2 (element 3). In general, a contraction dissipates acoustic waves.

For a wave propagation through a thin plate, like a perforated burner plate (element 6 in figure A.2), there would be little time lag between the two sides. All medium particles would move with the same velocity, let say, u. Thus, integration of (A.62) over the volume occupied by the flow through the plate gives:

$$
S(p_{\mathrm{l}}' - p_{\mathrm{r}}') = \rho_0 S l \frac{\mathrm{d}u'}{\mathrm{d}t}, \qquad\qquad (A.72)
$$

where S is the cross sectional area of the perforations, and l the thickness of the plate. Condition (A.72) can be written as $p_{\mathrm{l}}' - p_{\mathrm{r}}' = \mathrm{i}\rho_0 l\omega u'$ with $u' = u_{\mathrm{l}}' = u_{\mathrm{r}}'$, which yields the transfer matrix of a burner plate:

$$
\begin{bmatrix} p_{\mathrm{l}}' \\ u_{\mathrm{l}}' \end{bmatrix} = \begin{bmatrix} 1 & Z_{\mathrm{g}} \\ 0 & 1 \end{bmatrix} \begin{bmatrix} p_{\mathrm{r}}' \\ u_{\mathrm{r}}' \end{bmatrix}, \qquad\qquad (A.73)
$$

where $Z_g = i\rho_0\omega l$ is the impedance of the burner plate [49, 41]. This implies that a plate has little resistance to the acoustic field. Note that in practical situations, a burner plate with small perforations absorbs acoustic energy, due to the pressure drop, which is small in our case (see section 5.2, for a slit burner configuration).

At the open termination of a tube acoustic energy is radiated. The following radiation impedance, for the tube terminated without a flange, is posed:

$$Z_{\text{open end}} \approx \left(\frac{k_0^2 S_d^2}{16} + ik_0\delta\right) Z_0, \tag{A.74}$$

with δ the end correction given by $\delta = 0.6133 S_d/2$. δ is obtained by a close empirical fit for $k_0 S_d/2 \ll 0.5$ [41]. At a closed end we have $u' = 0$ by definition, hence, $Z_{\text{closed end}} = \infty$. In section 2.5 it is assumed that no acoustic energy is radiated at the open end, or $Z_{\text{open end}} = 0$.

A.6   Zeldovich progress variable

Introduction of additional restrictive assumptions is useful in the analysis of many problems. The objective of this section is to express the species equations and energy equation in a simplified form. The assumption of equal Lewis numbers allows us to describe all species as function of one tracer species, e.g. that of methane. In the global reaction $CH_4 + 2O_2 \longrightarrow CO_2 + 2H_2O$ the consecutive mass fractions can be described as function of the Zeldovich progress variable Z, which is 1 at the unburnt side and 0 at the burnt side. This variable is closely related to the mass fraction of methane in a lean gas mixture:

$$Y_{CH_4}(Z) = Y_{CH_4,u}Z, \tag{A.75}$$

$$Y_{O_2}(Z) = Y_{O_2,u}Z + [Y_{O_2,u} - 2Y_{CH_4,u}\frac{M_{O_2}}{M_{CH_4}}](1 - Z), \tag{A.76}$$

$$Y_{CO_2}(Z) = \frac{M_{CO_2}}{M_{CH_4}}Y_{CH_4,u}(1 - Z), \tag{A.77}$$

$$Y_{H_2O}(Z) = \frac{M_{H_2O}}{M_{CH_4}}Y_{CH_4,u}(1 - Z), \tag{A.78}$$

$$Y_{N_2} = 1 - Y_{CH_4,u} - Y_{O_2,u}. \tag{A.79}$$

The enthalpy h can also be written in a simplified form. Following the definition (2.11) and assuming that all specific heat capacities are equal ($c_p = \bar{c}_p$), we write:

$$h = \Delta H\, Y_{CH_4} + \bar{c}_p T + h_c, \tag{A.80}$$

with

$$\Delta H = h_{CH_4}^{(0)} + 2h_{O_2}^{(0)}\frac{M_{O_2}}{M_{CH_4}} - h_{CO_2}^{(0)}\frac{M_{CO_2}}{M_{CH_4}} - 2h_{H_2O}^{(0)}\frac{M_{H_2O}}{M_{CH_4}} \quad \text{and} \tag{A.81}$$

$$h_c = h_{CH_4}^{(0)}Y_{CH_4,u} + h_{O_2}^{(0)}Y_{O_2,u} + h_{N_2}^{(0)}Y_{N_2,u} - \Delta H\, Y_{CH_4,u} - \bar{c}_p T_0. \tag{A.82}$$

Appendix B

Numerical model in detail

In this appendix, the numerical model is elaborated. Firstly, some numerical methods are explained that enhance the numerical procedure. Secondly, non-reflecting boundary conditions are derived, using the theory on hyperbolic partial differential equations. These boundary conditions are tested on the Riemann or shock tube problem, from which an analytical solution is available.

In section B.4, the method of abstracting acoustical data is explained.

B.1 Enhanced numerical procedure

In this section numerical methods are described, which are used frequently to enhance the procedure described in chapter 3. More details can be found in the thesis of Van 't Hof [58].

B.1.1 Broyden iteration method

A very good alternative for Newton's method is the Broyden iteration method [40]. This method uses a sequence of matrices B_i^k with approximations of the *inverse* of the Jacobian corresponding to the set of equations in cell i. Each iteration, the matrix B_i^k becomes a better approximation. This method avoids the direct evaluation of the Jacobian, which is in general a CPU-expensive job.

We start with an initial guess for B_i^0 and we update the solution ϕ_i^k similar to the Newton method:

$$\phi_i^{k+1} = \phi_i^k - \lambda\, B_i^k\, F_i(\underline{\phi}^k), \tag{B.1}$$

where λ is a relaxation parameter, and update the matrix $B_i^{k+1} = B_i^k + \delta B$, with:

$$\delta B = B_i^k \frac{(\lambda - 1)F_i(\underline{\phi}^k) + F_i(\underline{\phi}^{k+1})}{\|F_i(\underline{\phi}^k) - F_i(\underline{\phi}^{k+1})\|^2} (F_i(\underline{\phi}^k) - F_i(\underline{\phi}^{k+1}))^T. \tag{B.2}$$
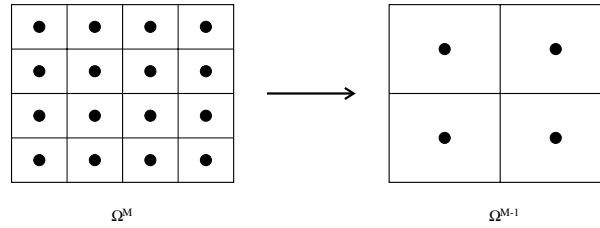
Figure B.1: A coarse grid Ω^{M-1} is constructed from the finer grid Ω^M by removing grid lines.

This matrix update is obtained by requiring that

$$(B_i^k + \delta B)(F_i(\underline{\phi}^k) - F_i(\underline{\phi}^{k+1})) = \phi_i^k - \phi_i^{k+1}, \tag{B.3}$$

so matrix B_i^{k+1} is an improved approximation of the inverse of the Jacobian. There are many ways to construct δB. The idea is to change B_i^k as little as possible and it can be shown that our choice (B.2) is a solution of (B.3) which minimises $\|\delta B\|_2$.

B.1.2   Multi-grid solver

The Gauss Seidel method proposed in section 3.4 is used as a smoother rather than a solver. In some problems, after a few Gauss-Seidel iteration steps, one notices that the residual decreases very little. In general, the small scale fluctuations in the residual are easily smoothed out, while the large scale fluctuations maintain. An improvement of convergence is obtained when using multi-grid methods. For both solving the predictor step (3.20) to (3.23) and solving the Poisson equation (3.26), the convergence increases drastically. In the multi-grid procedure, a number of grids is defined that are successively coarser. After a number of Gauss-Seidel steps on a fine grid, the residual is projected on a coarser grid and a defect is determined on the coarse grid. The solution on the fine grid is improved by the correction of an estimate of the defect. The communication between the grids is realised by restriction and prolongation operators.

The implementation of the different grids varies between different approaches. The simplest form is the successive elimination of all even grid lines in a rectangular grid Ω^M, as shown in figure B.1. The new grid point is defined as the average of the four points on the finer grid. In this case, one obtains grid Ω^{M-1}, in which each grid cell contains the surface of four grid cells from the finer grid. In this way we obtain a series of grids $\Omega^M, \Omega^{M-1}, \ldots, \Omega^1$.

In our case the governing equations are nonlinear and the discretisation yields a nonlinear set of equations on Ω^M:

$$F^M(\underline{\phi}^M) = \underline{f}^M. \tag{B.4}$$

Suppose that after a few iterations a solution $\underline{\phi}^M$ is obtained, then the defect is defined as:

$$\underline{r}^M = \underline{f}^M - F^M(\underline{\phi}^M). \tag{B.5}$$

The correction is solved on Ω^{M-1}:

$$F^{M-1}(\underline{\phi}^{M-1}) = F^{M-1}(R^M \underline{\phi}^M) - \sigma \underline{r}^{M-1}, \qquad (B.6)$$

where R^M is the restriction operator, $\underline{r}^{M-1}$ is the restricted defect $R^M \underline{r}^M$ and σ a relaxation parameter. The approximation $\underline{\phi}^{M-1}$ is used to correct the solution on the finer grid:

$$\underline{\phi}^M := \underline{\phi}^M + P^{M-1}(\underline{\phi}^{M-1} - R^M \underline{\phi}^M), \qquad (B.7)$$

where P^{M-1} is the prolongation operator.

The linear Poisson equation (3.26) (in a short notation: $\mathcal{P}\mathrm{d}p = \underline{\mathcal{C}}$) is also solved using the multi-grid method. The correction $\underline{\Delta\mathrm{d}p}^M$ on the finer grid is calculated from:

$$\mathcal{P}^M \underline{\Delta\mathrm{d}p}^M = \underline{r}^M, \qquad \text{with } \underline{r}^M = \underline{\mathcal{C}}^M - \mathcal{P}^M \underline{\mathrm{d}p}^M. \qquad (B.8)$$

By using the restriction operator R^M we solve on the coarser grid:

$$\mathcal{P}^{M-1} \underline{\Delta\mathrm{d}p}^{M-1} = \underline{r}^{M-1}, \qquad (B.9)$$

such that we can correct the pressure difference $\underline{\mathrm{d}p}^M$ on the finer grid:

$$\underline{\mathrm{d}p}^M := \underline{\mathrm{d}p}^M + P^{M-1} \underline{\Delta\mathrm{d}p}^{M-1}. \qquad (B.10)$$

B.1.3 Least squares extrapolation in time

The multi-grid scheme as described in the previous section is efficient, both with respect to operations and memory use. Still, however, a multi-grid V-cycle is very expensive: it requires a lot of computational effort. Much time can be saved by using the information of previous time steps to obtain a good approximation of $\underline{\phi}^n$ before the multi-grid method is used. Defining the search vectors s_j^n by:

$$\underline{s}_1^n = \underline{\phi}^{n-1} - \underline{\phi}^{n-2}, \qquad \underline{s}_2^n = \underline{s}_1^n - \underline{s}_1^{n-1}, \qquad \underline{s}_3^n = \underline{s}_2^n - \underline{s}_2^{n-1}, \qquad \cdots . \qquad (B.11)$$

We introduce nonlinear extrapolation, given by:

$$\underline{\phi}^n = \underline{\phi}^{n-1} + [\underline{s}_1^n, \cdots, \underline{s}_{N_k}^n]\alpha + \mathrm{O}(\Delta t^{N_k+1}), \qquad (B.12)$$

where α is a vector chosen in such a way that the residual is minimised in the two-norm. The number of search vectors denoted by N_k, is chosen small, e.g. $N_k = 3$. The vector α is approximated by the least squares solution of the linearisation of problem:

$$F(\underline{\phi}^n) = 0. \qquad (B.13)$$

With the residual function F from (B.13), we can calculate the matrix M^n, given by:

$$M^n = \left[F(\underline{\phi}^{n-1} + \underline{s}_1^n) - F(\underline{\phi}^{n-1}), \cdots, F(\underline{\phi}^{n-1} + \underline{s}_{N_k}^n) - F(\underline{\phi}^{n-1}) \right]. \qquad (B.14)$$

Now the vector α is found from:

$$\alpha = -((M^n)^{\mathrm{T}} M^n)^{-1} (M^n)^{\mathrm{T}} F(\underline{\phi}^{n-1}).\tag{B.15}$$

It must be noted that, if N_k is not small enough, the current extrapolation method becomes very inefficient, and suffers from round-off errors. Van 't Hof [58] did not encounter these problems with $N_k \leq 3$. In this study, the current form was chosen because it deals with nonlinearities in a correct way, and because it is very flexible with respect to the definition of search vectors $\underline{s}_j$.

B.2   Hyperbolic partial differential equations

Consider a set of n quasi-linear first-order Partial Differential Equations in two independent variables $x \in \Omega \subset \mathbb{R}$ and t. In a short notation, these equations read:

$$P(x,t,\phi)\frac{\partial \phi}{\partial t} + Q(x,t,\phi)\frac{\partial \phi}{\partial x} = r(x,t,\phi),\tag{B.16}$$

with $\phi, r \in \mathbb{C}^n$ and $P, Q \in \mathbb{C}^{n \times n}$ and suppose that P^{-1} exists. We may classify this system of equations following [28] and [60] as:

Definition B.2.1 *The system of equations (B.16) is called*

1. *strictly hyperbolic when all eigenvalues of $P^{-1}Q$ are real and distinct;*

2. *strongly hyperbolic when all eigenvalues of $P^{-1}Q$ are real and the matrix is nonsingular;*

3. *weakly hyperbolic or parabolic when the eigenvalues are real, but the matrix is singular;*

4. *elliptic when all eigenvalues are strictly imaginary.*

Problems with mixed eigenvalues are not classified, but are present in, for example, the transport equations for reacting flows. In the next subsection we derive the wave-equivalent of a hyperbolic PDE of the form (B.16).

B.2.1   Characteristics and invariants

We will take a closer look at the strong hyperbolic equations. We write $P^{-1}Q = S\Lambda S^{-1}$ with l_i the rows of matrix S^{-1}, $i = 1, \cdots, n$, and Λ a diagonal matrix. If we define $\hat{r} = P^{-1}r$ we write:

$$S^{-1}\frac{\partial \phi}{\partial t} + \Lambda S^{-1}\frac{\partial \phi}{\partial x} = S^{-1}\,\hat{r},\tag{B.17}$$

or

$$l_i \cdot \frac{\partial \phi}{\partial t} + \lambda_i l_i \cdot \frac{\partial \phi}{\partial x} = l_i \cdot \hat{r}, \quad i = 1, \cdots, n. \tag{B.18}$$

If we use w, defined as $\mathrm{d}w_i = l_i \cdot \mathrm{d}\phi - l_i \cdot \hat{r}\mathrm{d}t$ then (B.18) is written as:

$$\frac{\partial w_i}{\partial t} + \lambda_i \frac{\partial w_i}{\partial x} = 0, \quad i = 1, \cdots, n. \tag{B.19}$$

We see that the curves $\frac{\mathrm{d}x}{\mathrm{d}t} = \lambda_i$ are the (basic) characteristics, because w_i is constant along paths $x(t)$ satisfying $\frac{\mathrm{d}x}{\mathrm{d}t} = \lambda_i$. The quantities w_i are referred to as the characteristic variables or Riemann variables.

B.2.2   Posing boundary conditions

From the previous section we know the path (and its direction in the x, t-plane) along which Riemann variables are preserved. Following the ideas of [21, 55], we are able to pose conditions at the inflow and outflow boundaries of our domain. Hedstrom proposed that the Riemann variables w_i of the incoming waves must be prescribed:

$$\frac{\partial w_i}{\partial t} = f_i(t). \tag{B.20}$$

For a 'nonreflective' boundary, we state that the incoming waves are not present or $\frac{\partial w_i}{\partial t} = 0$. This means that:

$$l_i \cdot \frac{\partial \phi}{\partial t} - l_i \cdot \hat{r} = 0, \tag{B.21}$$

at such a boundary. This results in a boundary condition for the different Riemann variables with index i:

$$l_i \cdot \frac{\partial \phi}{\partial t} + g_i - l_i \cdot \hat{r} = 0, \tag{B.22}$$

with

$$g_i = \begin{cases} \lambda_i l_i \cdot \frac{\partial \phi}{\partial x} & \text{for outgoing characteristics} \\ 0 & \text{for incoming characteristics} \end{cases}. \tag{B.23}$$

In this study we want to simulate sound waves by defining a source at one of the boundaries. We prescribe the Riemann variables belonging to incoming characteristics as: $\frac{\partial w_i}{\partial t} = f_i(t)$, with $f_i(t)$ a given (harmonic) function. Then $w_i =$ constant propagates with the propagation speed λ_i into the domain. We have:

$$l_i \cdot \frac{\partial \phi}{\partial t} - l_i \cdot \hat{r} = f_i(t), \tag{B.24}$$

for these incoming characteristics.

In general, we may combine (B.22) and (B.24) as follows:

$$S^{-1}\frac{\partial \phi}{\partial t} + \Gamma S^{-1}\frac{\partial \phi}{\partial x} = S^{-1}r + F, \tag{B.25}$$

at the different boundaries, with Γ a diagonal matrix defined by $\Gamma_{ii} = \lambda_i$ for the outgoing characteristics, and $\Gamma_{ii} = 0$ for incoming characteristics. F is a vector containing the $F_i = f_i$.

B.2.3   Euler equations for one-dimensional reactive flows

The boundary conditions are to be situated far from the flame where diffusion effects can be neglected and no reactions take place ($\dot{\rho} \approx 0$).

In this case, the transport equations, as formulated in chapter 2 reduce to the Euler equations:

$$\frac{\partial \rho Y}{\partial t} + \frac{\partial \rho u Y}{\partial x} = 0, \tag{B.26}$$

$$\frac{\partial \rho}{\partial t} + \frac{\partial \rho u}{\partial x} = 0, \tag{B.27}$$

$$\frac{\partial \rho u}{\partial t} + \frac{\partial \rho u^2}{\partial x} + \frac{\partial p}{\partial x} = 0, \tag{B.28}$$

$$\frac{\partial \rho E}{\partial t} + \frac{\partial \rho u H}{\partial x} = 0, \tag{B.29}$$

$$p = \rho R T, \tag{B.30}$$

where $\rho E = \rho H - p$, $H = h + \frac{1}{2}u^2$, $E = e + \frac{1}{2}u^2$ and $R = R_{\text{univ}}/\bar{M}$. We now derive a differential equation for $\phi = [Y^{\text{T}}, \rho, u, T]^{\text{T}}$ by eliminating the pressure using (B.30), where we have generalised the mass fractions of the species with $Y = [Y_1, \ldots, Y_{N-1}]^{\text{T}}$. Then the system can be written in the form of (B.16):

$$P(\phi)\frac{\partial \phi}{\partial t} + Q(\phi)\frac{\partial \phi}{\partial x} = \vec{r}(\phi), \tag{B.31}$$

with

$$P = \begin{bmatrix} \rho I & Y & 0 & 0 \\ 0 & 1 & 0 & 0 \\ 0 & u & \rho & 0 \\ \rho \left(\frac{\partial e}{\partial Y}\right)^{\text{T}} & H - RT & \rho u & \frac{\rho R}{\gamma-1} \end{bmatrix}, \tag{B.32}$$

and

$$Q = \begin{bmatrix} \rho u I & uY & \rho Y & 0 \\ 0 & u & \rho & 0 \\ \left(\frac{\partial p}{\partial Y}\right)^{\mathrm{T}} & u^2 + RT & 2\rho u & \rho R_M \\ \rho u \left(\frac{\partial h}{\partial Y}\right)^{\mathrm{T}} & Hu & \rho(u^2 + H) & \rho u c_p \end{bmatrix}, \tag{B.33}$$

with I the unity matrix. The eigenvalues of

$$P^{-1}Q \equiv S\Lambda S^{-1} \tag{B.34}$$

are $\lambda_i = \Lambda_{ii} = u, \cdots, u, u, u - c$ and $u + c$, with $c^2 = \gamma p/\rho$ defined as the speed of sound. Thus, according to the definition B.2.1, we have a strongly hyperbolic system. The transformation matrices S and S^{-1} for the Euler equations are given by, respectively:

$$S = \begin{bmatrix} I & 0 & 0 & 0 \\ 0 & \rho & \rho & \rho \\ 0 & 0 & -c & c \\ -\frac{T}{p}\left(\frac{\partial p}{\partial Y}\right)^{\mathrm{T}} & -T & (\gamma - 1)T & (\gamma - 1)T \end{bmatrix}, \tag{B.35}$$

and

$$S^{-1} = \begin{bmatrix} I & 0 & 0 & 0 \\ -\frac{1}{\rho c^2}\left(\frac{\partial p}{\partial Y}\right)^{\mathrm{T}} & \frac{\gamma-1}{\gamma}\frac{1}{\rho} & 0 & -\frac{1}{\gamma T} \\ \frac{1}{2\rho c^2}\left(\frac{\partial p}{\partial Y}\right)^{\mathrm{T}} & \frac{1}{2\gamma\rho} & -\frac{1}{2c} & \frac{1}{2\gamma T} \\ \frac{1}{2\rho c^2}\left(\frac{\partial p}{\partial Y}\right)^{\mathrm{T}} & \frac{1}{2\gamma\rho} & \frac{1}{2c} & \frac{1}{2\gamma T} \end{bmatrix}. \tag{B.36}$$

r equals zero due the assumptions at the boundaries. The eigenvectors of the corresponding eigenvalues are:

$$\mathrm{d}w_i = \mathrm{d}Y_i, \tag{B.37}$$

$$\mathrm{d}w_N = -\frac{1}{c_p}\mathrm{d}s, \tag{B.38}$$

$$\mathrm{d}w_{N+1} = \frac{1}{2\rho c^2}\mathrm{d}p - \frac{1}{2c}\mathrm{d}u, \tag{B.39}$$

$$\mathrm{d}w_{N+2} = \frac{1}{2\rho c^2}\mathrm{d}p + \frac{1}{2c}\mathrm{d}u, \tag{B.40}$$

where the entropy s is defined as $T\mathrm{d}s = p\mathrm{d}(1/\rho) + c_v\mathrm{d}T$.

These Riemann variables are, in the homogeneous case, the quantities that are preserved along paths in the x, t-plane with $\mathrm{d}x/\mathrm{d}t = \lambda_i$.

The boundary conditions are derived from the Riemann variables following section B.2.2. In case of a source, for example at the left boundary, we prescribe the incoming Riemann variable w_{N+2} (corresponding to eigenvalue $\lambda_{N+2} = u + c$) as:
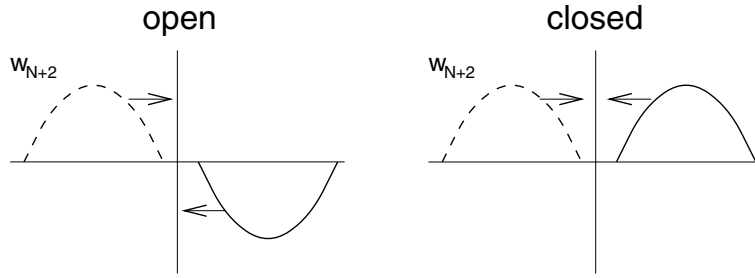
$$\frac{\partial w_i}{\partial t} = f_i(t). \tag{B.41}$$

Figure B.2: Open and closed boundaries

Here, we pose the harmonic input signal:

$$f_{N+2}(t) = A\omega\cos(\omega t), \tag{B.42}$$

with ω the frequency of the signal and A a dimensionless amplitude. Other examples of boundary conditions are the open and closed ends, which are $p' = 0$ and $u' = 0$, respectively. We can construct those boundary conditions from the Riemann variables. Figure B.2 shows the two cases. For a closed end we pose that the amplitude of the outgoing sound waves is equal to the amplitude of the incoming waves, or,

$$\frac{\partial w_{N+2}}{\partial t} = \frac{\partial w_{N+1}}{\partial t}. \tag{B.43}$$

For an open end we pose that the incoming waves are of the same amplitude as the outgoing wave, with opposite sign:

$$\frac{\partial w_{N+2}}{\partial t} = -\frac{\partial w_{N+1}}{\partial t}. \tag{B.44}$$

In the same way we can define half-reflecting/half-open ends by introducing reflection coefficients.

B.3   Exact solution of Riemann problem

The shock tube or Riemann problem has an exact solution to the full set of one-dimensional Euler equations containing a shock wave, a contact discontinuity and an expansion wave. The initial conditions are the following:

$$
\begin{aligned}
u = u_{\mathrm{L}}, \qquad p = p_{\mathrm{L}}, \qquad c = c_{\mathrm{L}}, \qquad &\text{for} \qquad x < 0,\ t < 0, \\
u = u_{\mathrm{R}}, \qquad p = p_{\mathrm{R}}, \qquad c = c_{\mathrm{R}}, \qquad &\text{for} \qquad x > 0,\ t < 0,
\end{aligned}
\tag{B.45}
$$

where $p_{\mathrm{R}} < p_{\mathrm{L}}$ and the membrane is located at $x = 0$. We will assume that the regions contain the same gas at the same temperature.

At time $t = 0$ the membrane is removed from the tube and a pressure discontinuity
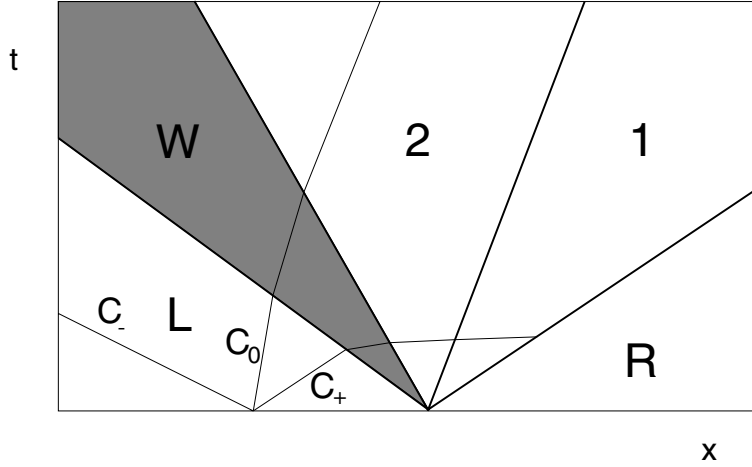
Figure B.3: Solution in x, t-plane of the Riemann problem, wherein the grey area is the expansion wave. The thin lines are the characteristics C_0, C_+ and C_-, along which the corresponding Riemann variables are constant.

propagates to the right, and simultaneously, an expansion wave propagates to the left. In addition, a contact discontinuity that separates the two gas regions propagates to the right in the tube. This is illustrated in figure B.3, which also shows the characteristics describing the path along which information is transported (see section B.2.1). We will distinguish four regions: region R contains the undisturbed gas at low pressure. It is separated by a shock wave from region 1 which represents the disturbed low-pressure gas. The contact discontinuity separates the disturbed high-pressure region 2, which in turn has been disturbed by an expansion wave W propagating to the left into the undisturbed high-pressure region L. The velocities of the discontinuities are constant since they propagate in a uniform gas.

The shock between regions R and 1 holds the normal shock relations. One has, as function of the pressure ratio $P \equiv p_1/p_R$:

$$\frac{\rho_1}{\rho_R} = \frac{1 + \alpha P}{\alpha + P}, \qquad \text{with} \quad \alpha = \frac{\gamma + 1}{\gamma - 1}, \tag{B.46}$$

$$M = \frac{C - u_R}{c_R} = (1 + \alpha P)^{\frac{1}{2}} \sqrt{\frac{\gamma - 1}{2\gamma}}, \tag{B.47}$$

$$\frac{u_1 - u_R}{c_R} = (P - 1)\frac{1}{\gamma M}, \tag{B.48}$$

and

$$\frac{c_1^2}{c_R^2} = P\frac{\alpha + P}{1 + \alpha P}. \tag{B.49}$$

The quantity C is the propagation speed of the shock in region R and M the Mach number. The contact discontinuity allows a density change but the pressure and velocity are continuous. Therefore, the contact discontinuity propagates with a velocity equal to u_1. Over the discontinuity the jump conditions

$$p_2 = p_1, \qquad u_2 = u_1, \tag{B.50}$$

have to be satisfied.

The expansion wave is formed by the characteristics with slope $u - c$ and information between the regions L and 1 is transported along the C_+ and C_0 characteristics. Along C_0 the entropy is constant or

$$\frac{p_L}{\rho_L^{\gamma}} = \frac{p_2}{\rho_2^{\gamma}} \tag{B.51}$$

using the isentropic relation. Along C_+ the Riemann variable

$$\frac{\gamma - 1}{2} u_L + c_L = \frac{\gamma - 1}{2} u_2 + c_2 \tag{B.52}$$

is constant.

From (B.52), we obtain a relation between u_1 and p_1:

$$u_1 - u_L = \frac{2}{\gamma - 1} c_L \left[1 - \left(\frac{p_1}{p_L} \right)^{\frac{\gamma - 1}{2\gamma}} \right], \tag{B.53}$$

using the conditions for the contact discontinuity (B.50), (B.51), and the isentropic relation

$$\frac{c_2}{c_L} = \left(\frac{\rho_2}{\rho_L} \right)^{\frac{\gamma - 1}{2}}. \tag{B.54}$$

Elimination of u_1 in equation (B.53) by using the shock relations (B.47) and (B.48) leads to an implicit relation for the pressure ratio P:

$$\sqrt{\frac{\gamma - 1}{2\gamma}} \frac{P - 1}{(1 + \alpha P)^{1/2}} = \frac{c_L}{c_R} \left[1 - \left(P \frac{p_R}{p_L} \right)^{\frac{\gamma - 1}{2\gamma}} \right] + \frac{u_L - u_R}{c_R}. \tag{B.55}$$

Finally, the continuous evolution of the variables in the expansion wave has to be determined. The information from the left region is transported along the characteristics C_0 and C_+, which means that

$$\frac{p_W}{\rho_W}^{\gamma} = \frac{p_L}{\rho_L}^{\gamma}, \tag{B.56}$$

and

$$\frac{\gamma - 1}{2} u_W + c_W = \frac{\gamma - 1}{2} u_L + c_L. \tag{B.57}$$

In addition, the expansion wave is constructed by the C_- characteristics with $\mathrm{d}x/\mathrm{d}t = u_W - c_W$. By eliminating c_W using (B.57) each characteristic is defined by:

$$\frac{\mathrm{d}x}{\mathrm{d}t} = \frac{\gamma+1}{2}u_W - c_L - \frac{\gamma-1}{2}u_L. \tag{B.58}$$

Using that the Riemann variable $\frac{1}{2}(\gamma-1)u_W - c_W$ is constant along the characteristics, (B.58) can be integrated. In region W, the velocity u_W, speed of sound c_W and pressure p_W become:

$$u_W \quad = \quad \frac{2}{\gamma+1}\left(\frac{x}{t} + c_L + \frac{\gamma-1}{2}u_L\right), \tag{B.59}$$

$$c_W \quad = \quad u_W - \frac{x}{t}, \tag{B.60}$$

$$p_W \quad = \quad p_L \left(\frac{c_W}{c_L}\right)^{\frac{2\gamma}{\gamma-1}} \tag{B.61}$$

$$\text{for} \qquad \frac{\gamma+1}{2}u_L - c_L - \frac{\gamma-1}{2}u_L < \frac{x}{t} < \frac{\gamma+1}{2}u_1 - c_L - \frac{\gamma-1}{2}u_L.$$

By calculating the pressure ratio P all quantities are determined. The temperature can be determined by using the perfect gas law $p = \rho RT$, where R is the gas constant. In figure 3.6 in section 3.5.1, the pressure distribution at a certain time is shown. The temperature, density and velocity are shown at a time $t = 6 \times 10^{-3}$ sec after removing the membrane in figures B.4 to B.6, respectively. As in figure 3.6, the discontinuities are smoothened by artificial diffusion.

B.4 Obtaining acoustical data

In the study of the acoustics in a burner/flame system, frequency dependent results must be obtained from the simulations, where the flame is perturbed with an external sinusoidal source.

One way to proceed is to do one simulation for each frequency. This procedure is time consuming. Instead of using one frequency at a time, we can use broad-band signals. These signals contain a broad spectrum of frequencies. Examples of these signals are shown in figure B.7: block and sweep signals. Another example is noise, which mostly contains high frequency signals. However, high frequency simulations need even more time and spatial resolution, so noise is not useful in this study. The block signal is of greatest interest, because it is easy to implement, and analytically, the spectrum contains all frequencies. The sweep has also a wide range spectrum. The signal is a sinusoidal wave, with the frequency varying in time. The simplest form of frequency change is a linear function that varies the frequency from a low frequency to a high frequency. This input signal is also used in practical burner applications, in which the response of real life devices is determined.

Figure B.4: Temperature profile in the tube from the numerical simulation (solid line), compared with the exact solution (dashed line) at $t = 6 \times 10^{-3}$ s.
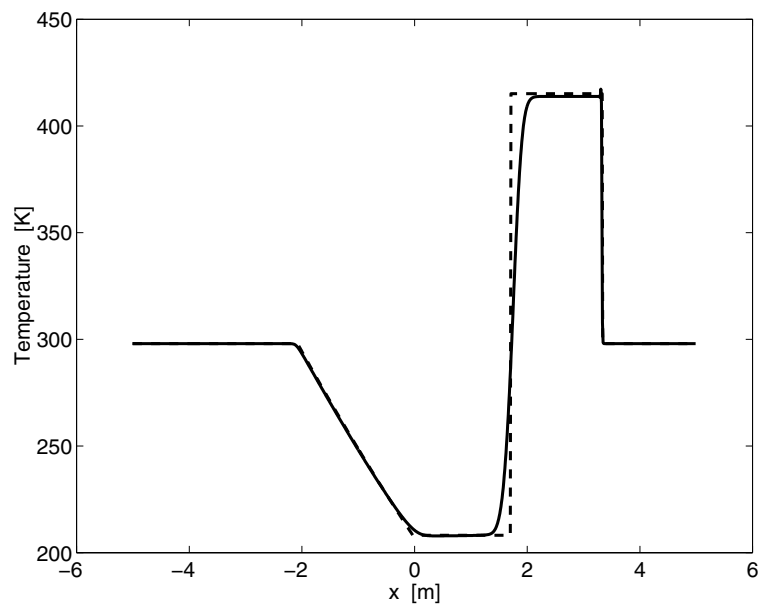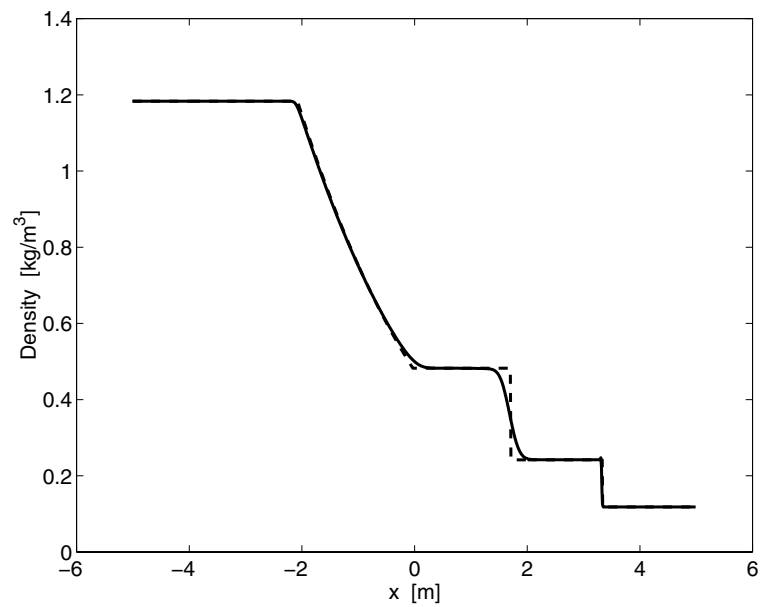

Figure B.5: Density profile in the tube from the numerical simulation (solid line), compared with the exact solution (dashed line) at $t = 6 \times 10^{-3}$ s.
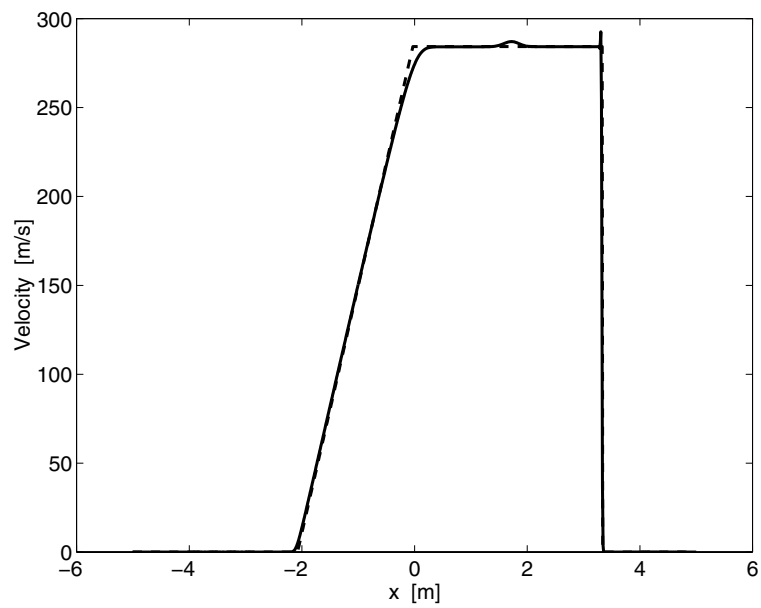
Figure B.6: Flow velocity in the tube from the numerical simulation (solid line), compared with the exact solution (dashed line) at $t = 6 \times 10^{-3}$ s.
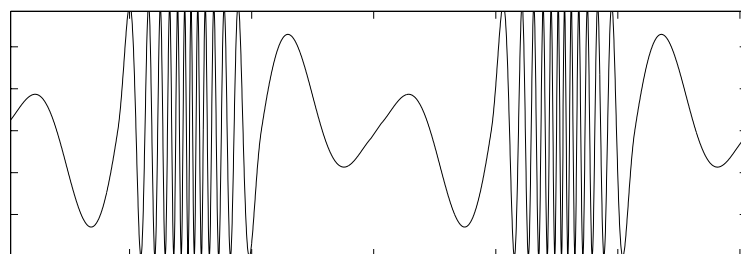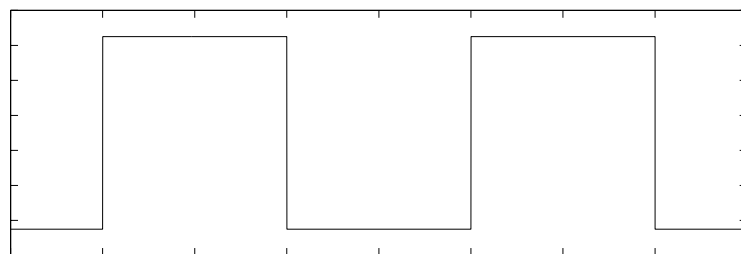
Figure B.7: Examples of broad-band signals: (a) sweep, (b) block signal.

In the case of a linear response the input signal and the output signals are processed using standard discrete Fourier transforms. From the simulations the input and output signals are sampled in time. The frequency dependent response is simply the division of the discrete Fourier transforms of the samples of the output signal and the samples of the input signal.

Appendix C

Other analytical models

Numerous investigations have been performed on heat-driven and combustion-driven flames. An extensive review can be found in [44].

In early theoretical studies on burner/flame systems, the flame response was based on simple phenomenological models. The response was looked upon as a source of heat, which is related to the mass flow input. Section C.1 gives an example of an investigation that treats the flame, when placed inside a tube, as a black box. The more fundamental theory is given in section C.2. This theory considers the species and flow equations to describe the flame/burner system in detail.

C.1 Analytical model by Dowling

The method to determine resonance frequencies used by Dowling [14], considers the exact profiles for the acoustic field inside a tube system (see figure C.1) with and without a mean flow. Dowling's aim was to investigate the effects of mean flow, drag inside the heating element, and heat input distributed over a finite length, on the frequency of the thermoacoustic oscillation. Another focus of investigation was the effect of the form of coupling between the heat input and the unsteady flow.

An unsteady heat source is placed at a single plane $x = b$, across which the mean temperature jumps from $\bar{T}_1$ to $\bar{T}_2$. The inhomogeneous wave equation which describes the pressure
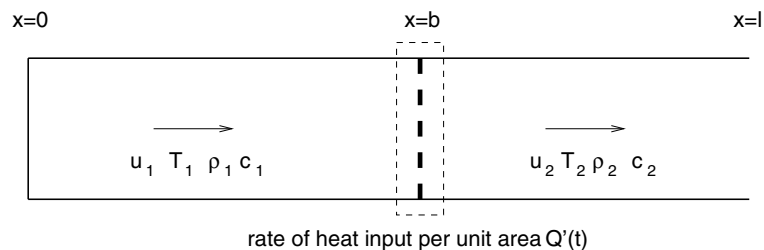

Figure C.1: The tube with closed and open ends used by Dowling.

125

perturbation generated by an unsteady heat input $q'(\boldsymbol{x}, t)$ is given by [14]:

$$\frac{1}{\bar{c}^2} \frac{\partial^2 p'}{\partial t^2} - \bar{\rho} \boldsymbol{\nabla} \cdot \left(\frac{1}{\bar{\rho}} \boldsymbol{\nabla} p' \right) = \frac{\gamma - 1}{\bar{c}^2} \left(\frac{\partial q'}{\partial t} \right). \tag{C.1}$$

It is assumed that the unsteady heat input is concentrated at the plane $x = b$, and described by $q'(\boldsymbol{x}, t) = Q'(t)\delta(x - b)$, where δ denotes the Dirac δ-function. On both sides of the plane two different states are present, each with a different temperature, density and speed of sound. The solution on both sides is described by equations (A.65) and (A.67), and an additional jump condition over the plane $x = b$ is derived, which relates the heat input to the acoustic field. This basically is the transfer matrix of the heat input zone.

The acoustic modes in the system satisfy an implicit dispersion relation. Dowling uses one-dimensional Green's functions to obtain this relation. The Green's function, denoted as $G(x|x_0)$, satisfies the harmonic pulse response of the wave equation,

$$\bar{\rho} \bar{c}^2 \frac{\mathrm{d}}{\mathrm{d}x} \left(\frac{1}{\bar{\rho}} \frac{\mathrm{d}G}{\mathrm{d}x} \right) + \omega^2 G = -\bar{c}_p (\gamma - 1) \delta(x - x_0), \tag{C.2}$$

and the boundary conditions. $G(x|x_0)$ is derived by adding Heaviside functions to the solution of the homogeneous equation.

Writing $q'(\boldsymbol{x}, t) = \hat{q}(x) \exp(\mathrm{i}\omega t)$, the solution of equation (C.1) is then given by $p(\mathbf{x}, t) = \hat{p}(x) \exp(\mathrm{i}\omega t)$, where

$$\hat{p}(x) = \frac{\mathrm{i}\omega}{\bar{c}_p} \int G(x|x_0) \hat{q}(x_0) \, \mathrm{d}x_0. \tag{C.3}$$

For $\hat{q}(x_0) = \hat{Q} \delta(x_0 - b)$, we have:

$$\hat{p}(0) = \mathrm{i}\omega \hat{Q} G(0|b), \tag{C.4}$$

with

$$G(0|b) = -\frac{\bar{c}_1 \bar{c}_2}{\omega} \frac{\sin(\beta)}{\bar{T}_1 \bar{c}_2 \sin(\alpha) \sin(\beta) - \bar{T}_2 \bar{c}_1 \cos(\alpha) \cos(\beta)}, \tag{C.5}$$

$$\alpha = \frac{\omega b}{\bar{c}_1}, \qquad \beta = \frac{\omega(l - b)}{\bar{c}_2}. \tag{C.6}$$

In summary, a Green's function can be a useful tool in the investigation of thermoacoustic oscillations as well. However, it is not sufficient to simply investigate the Green's function alone. Also, the form of the coupling between the heat input and the flow should be considered. Thermoacoustic instability mostly involves coupling between the heat input and the flow. The unsteady heat input occurs as a response to fluctuations in the pressure. This can be expressed in the phenomenological form:

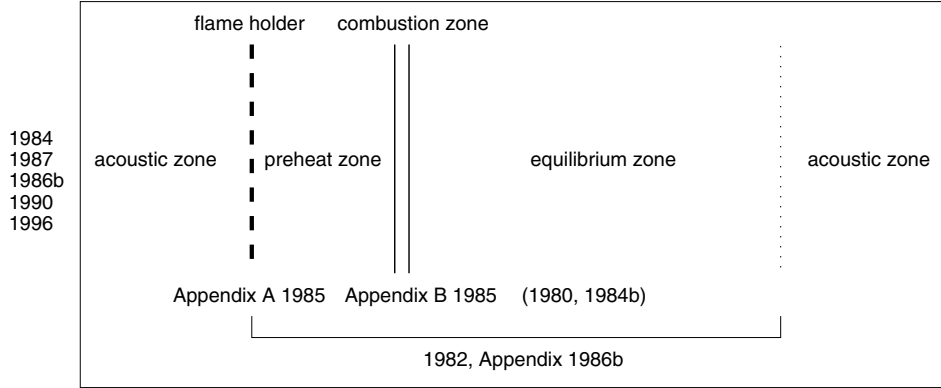$$\hat{Q} = Z(\omega)\hat{p}(0), \tag{C.7}$$

Figure C.2: The areas of the configuration, which are used in the papers by McIntosh *et al.* on the stability of burner-stabilised premixed flames. The figures correspond to the year of the published paper that investigates the stability of or provides relations for a particular part of the configuration.

for some function $Z(\omega)$. Substituted in equation (C.4) leads to:

$$\hat{p}(0)[1 - i\omega Z(\omega)G(0|b)] = 0. \tag{C.8}$$

The frequency ω satisfying (C.8) are the resonance frequencies of the system.

If the heat input responds to the flow, the oscillation frequency is shifted in comparison to the frequencies obtained by assuming a specified source.

Dowling shows that mean flow effects are found to be significant. With a mean stagnation temperature rise $\bar{T}_2/\bar{T}_1$ of a factor six, the frequency of thermoacoustic oscillations for an inlet Mach number of 0.15 can be reduced to half its value with no mean flow. The results also show that for Mach numbers lower than 0.05 the mean flow effects are negligible. For flows used in this thesis the mean flow Mach number is of order $O(10^{-4})$ (see also the validation of the low-Mach number assumption in section 3.5.3).

The drag force exerted by a grid or flame holder with a blockage ratio of 50% or less is found to have a negligible effect on the frequency of thermoacoustic oscillations for Mach numbers less than 0.1. In the calculations on the two-dimensional slit-burner configuration in this thesis, the blockage ratio is 33%. This means that no drag force effects are expected in our case.

C.2 Analytical model by McIntosh & Clark

Figure C.2 shows the way the one-dimensional domain for a burner-stabilised one-dimensional flame is divided in the work done by McIntosh & Clark. Five zones are distinguished. Two acoustic zones far up- and downstream, the pre-heat zone, the combustion zone and the equilibrium zone. The dashed line in figure C.2 is the burner plate or flame holder, on which the flame stabilises. Staying in the context of transfer functions, McIntosh & Clark

derived relations that connect the fluctuating quantities in up- and downstream regions. In figure C.2 the references can be found, where these relations are derived and investigated. In 1980 (Clark *et al.* [6]), the static stability of the one-dimensional flame is analysed. They introduced Large Activation Energy Asymptotics (LAEA) to solve the stationary flame equations. The asymptotic analysis shows that the length of the combustion zone is $O(\Theta^{-1})$ compared to the flame zone, which is $O(\Theta^{-1})$. Θ is the dimensionless activation energy. In 1982, McIntosh *et al.* [38] studied the response of the flame on mass flow and gas composition variations. The resulting equations showed that $O(1)$ changes in either mass flux or composition produce similar (i.e. $O(1)$) changes in flame position, but very small changes (i.e. $O(\Theta^{-1})$) in flame temperature. The results reveal 'peak frequencies' for which the oscillations (i.e. response) are at a maximum. Furthermore, near these peaks the phase of the oscillations is rapidly changing with frequency, and the peak frequency lies close to the frequencies where the phase difference between the temperature oscillations and inlet velocity fluctuations is $\pi/2$. This is also the case for the response of the mass burning velocity (see figure 4.3 in our model).

In 1984 (McIntosh & Clark [39]), a second-order model in Θ^{-1} is derived, and in the same year, results of this model are used for studying the one-dimensional burner-stabilised flame placed in an acoustic field. A transfer function for the velocity fluctuations is derived. Using this relation, the stability of a flame placed in a tube with infinite length was investigated (McIntosh [31]).

In the 1985 paper [32], McIntosh studied the cellular instability of stabilised flames. This investigation extended the theory to two-dimensional problems. Jump conditions for the quantities through the combustion zone are derived. Also, the effect of the burner on the acoustic field is given. It is assumed that, within the burner material, the flow obeys Darcy's law, which links the pressure gradient with the flow velocity.

In 1986 and 1987 (McIntosh [33, 34]) the one-dimensional flame is placed in a tube with finite upstream length. The stability analysis takes into account acoustic forcing and feedback. The appendix of the 1986 paper gives a clear derivation of the transfer function for the velocity fluctuations.

Finally, recent papers (McIntosh [35] and McIntosh *et al.* [37]) applied the theory to the Rijke tube configurations and compared them with experiments.

Although the work of Clark & McIntosh largely covers the acoustic description of burner-stabilised one-dimensional flames, it is theoretically complex and not easily understood. The model presented in this thesis is based on assumptions that simplify the relations considerably. A summary of the differences and the resulting transfer function is given below.

McIntosh's theory is applicable for arbitrary Lewis numbers. The model in this thesis assumes unit Lewis numbers. Derivation of an extension of our model to arbitrary Lewis numbers is not easy, because the enthalpy equation cannot be easily solved for non-unit Lewis numbers. The diffusion of the mass fraction enters the equation, which couples the species equation to the enthalpy equation. For this reason, the enthalpy fluctuations are dependent on the mass fraction variations in the entire domain (pre-heat, combustion, and equilibrium zones).

McIntosh switches to the density-weighted coordinate x_1 in the same way as done in this thesis (cf. section 4.2.2). As mentioned above, the equations are linearised provided that the order of perturbations ϵ satisfies:

$$\Theta^{-1} \gg \epsilon \gg Ma^2. \tag{C.9}$$

In this thesis, the infinitely thin combustion zone assumption can be interpreted as taking a very large activation energy. This is applied in the analysis before linearisation. McIntosh linearises before applying LAEA. In his paper [39] he argued that $O(\epsilon^2)$ terms should be included in case of linearising afterwards. Furthermore, this method can then be valid for ϵ within a fairly tight band:

$$1 \gg \epsilon \gg \Theta^{-1/2}. \tag{C.10}$$

After linearisation, McIntosh applies the Combustion Approximation on the equations. The values and gradients in the burner/flame region and the acoustic zones are matched up to leading-order terms, following the principles of matched asymptotic expansions, as in this thesis.
The resulting equations are solved for harmonic solutions. In the acoustic zones the classic acoustic solution is obtained, and the linear solutions in the burner/flame region eventually gives, by using the jump conditions, the relation connecting the fluctuating velocities:

$$u_{\mathrm{b}}' = -\frac{1}{T_{01}} \mathcal{V} u_{\mathrm{u}}', \tag{C.11}$$

where u_{u}' and u_{b}' are the upstream and downstream fluctuating velocities, respectively. $T_{01} = \bar{T}_{\mathrm{u}}/\bar{T}_{\mathrm{b}}$ is the ratio of the cold upstream temperature to the initial flame temperature, and $\mathcal{V}$ is the transfer function. For unit-Lewis numbers this transfer function yields (McIntosh [37]):

$$\mathcal{V} \approx -T_{01} - \frac{(1 - T_{01}) \left(\frac{1}{2} + r\right) \exp\left(-\left(\frac{1}{2} + r\right) x_{1,\mathrm{f}}\right)}{2 T_{01} \left(r \exp(-2 x_{1,\mathrm{f}}) + \frac{w}{\Theta(1 - T_{01})}\right)}, \qquad r = \sqrt{w + \frac{1}{4}}, \tag{C.12}$$

where $x_{1,\mathrm{f}}$ is the steady dimensionless flame stand-off distance or adiabaticity, given by:

$$x_{1,\mathrm{f}} = \ln\left(\frac{T_{\mathrm{ad}} - \bar{T}_{\mathrm{u}}}{T_{\mathrm{ad}} - \bar{T}_{\mathrm{b}}}\right), \tag{C.13}$$

w being the dimensionless complex dimensionless frequency:

$$w = \mathrm{i}\omega \frac{D}{\bar{u}_{\mathrm{u}}^2}, \tag{C.14}$$

where D is the species mass diffusion coefficient at the cold inlet. A complex equation for the amplification of the acoustic pressure was obtained by relating equations describing

emitted and incident upstream and emitted downstream waves through the transfer function. From this equation, the effect of a finite upstream tube length was predicted.

An example of the application of this transfer function in a stability analysis is studied in McIntosh *et al.* [37]. In this paper, the stability of two Rijke tube configurations is investigated. The first one is the Rijke tube model with acoustical open ends (see figure 1.2). When the wave equations and the open tube conditions are applied along with the velocity transfer function and a jump condition that takes into account the effect of the flame holder on the acoustic field, the following frequency condition emerges:

$$\mathcal{V}\frac{\cosh(\omega l_1)}{\sinh(\omega l_1)} - \sqrt{T_{01}}\frac{\cosh(\omega l_2\sqrt{T_{01}})}{\sinh(\omega l_2\sqrt{T_{01}})} + \sqrt{T_{01}}Z_\mathrm{g}\frac{\cosh(\omega l_1)\cosh(\omega l_2\sqrt{T_{01}})}{\sinh(\omega l_1)\sinh(\omega l_2\sqrt{T_{01}})} = 0, \qquad \text{(C.15)}$$

where Z_g is the impedance of the flame holder (cf. equation (A.73)):

$$p_2' - p_1' = \gamma Z_\mathrm{g}u_1'. \qquad \text{(C.16)}$$

In a good approximation $Z_\mathrm{g} \approx \mathrm{i}X_\mathrm{g}$, X_g being a measure for the blockage in the tube.

The Rayleigh criterion (1.1) is satisfied for this type of burner when [36]:

$$\mathrm{phase}(\mathcal{V}) \equiv \cot\left(\frac{\mathrm{Im}(\mathcal{V})}{\mathrm{Re}(\mathcal{V})}\right) > 0. \qquad \text{(C.17)}$$

Results show that the loci of $\mathrm{phase}(\mathcal{V}) = 0$ match exactly with the loci of $\mathrm{Re}(\omega) = 0$ when the frequency is plotted against the adiabaticity. This indicates that the criterion (C.17) is applicable to a wide range of Rijke tube configurations, such as the simple configuration as used by Dowling (see figure C.1).

When the upstream end of the tube is acoustically closed, then the equivalent condition (C.15) is given by:

$$\mathcal{V} - \sqrt{T_{01}}\frac{\cosh(\omega l_1)\cosh(\omega l_2\sqrt{T_{01}})}{\sinh(\omega l_1)\sinh(\omega l_2\sqrt{T_{01}})} + \sqrt{T_{01}}Z_\mathrm{g}\frac{\cosh(\omega l_2\sqrt{T_{01}})}{\sinh(\omega l_2\sqrt{T_{01}})} = 0. \qquad \text{(C.18)}$$

The Rayleigh criterion (C.17) is still the criterion for resonance, so the global significance of the frequency-adiabaticity plot is unchanged in this case as well. Thus, as long as the adiabaticity is known, one can predict whether a certain frequency will be resonant or not. The dependence on the activation energy is not very significant, so the chemistry of the combustion is not very crucial in these results. Effectively, for a given frequency the resonance prediction is only dependent on the amount of heat loss. In order to get an estimate of the frequency of oscillation, it is necessary to consider the complete solution of equations (C.15) or (C.18). Results show a good comparison with experimental results, where $X_\mathrm{g} = 0$ was taken in the model [37].

Appendix D

An analytical two-dimensional model

A theoretical model for almost flat flames is presented in this appendix.

In y-direction the solution is periodical (one period is the pitch between two perforations as shown in figure D.1) and the flow fluctuations are harmonic. Like in the one-dimensional situation, the entire mass fraction profile is assumed to be rigid and moves in x-direction only. The presence of the plate does not change the profile in time, or equivalently the plate is thin enough that gas diffuses to the unburnt gas easily. In x-direction density-weighted coordinates are used. Furthermore, some assumptions of constant velocity and density are made to be able to obtain analytical solutions. Also the approximations of constant heat capacity $c_p = \bar{c}_p$ and constant $\rho\lambda$ are made. The following two-dimensional model will prove that under some strict assumptions (two-dimensional) flat flames can be approximated by one-dimensional flames.

We start with the formulation of the two-dimensional enthalpy equation:

$$\rho\frac{\partial J}{\partial t} + \rho u\frac{\partial J}{\partial x} + \rho v\frac{\partial J}{\partial y} - \frac{\partial}{\partial x}\left(\frac{\lambda}{c_p}\frac{\partial J}{\partial x}\right) - \frac{\partial}{\partial y}\left(\frac{\lambda}{c_p}\frac{\partial J}{\partial y}\right) = 0. \tag{D.1}$$

The new coordinate system is:

$$\psi(x, y, t) = \frac{1}{\bar{\rho}_u}\int_0^x \rho(x', y, t)\,\mathrm{d}x', \tag{D.2}$$
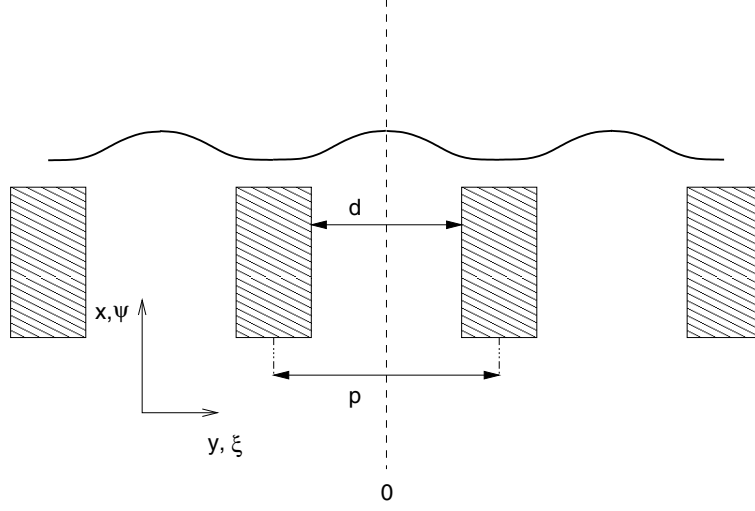
$$\xi(x, y, t) = y, \tag{D.3}$$

$$\tau(x, y, t) = t. \tag{D.4}$$

We obtain the transformed derivatives:

$$\frac{\partial}{\partial x} = \frac{1}{\bar{\rho}_u}\rho\frac{\partial}{\partial \psi}, \tag{D.5}$$

$$\frac{\partial}{\partial y} = \frac{1}{\bar{\rho}_u}\int_0^x \frac{\partial\rho}{\partial y}\,\mathrm{d}x'\frac{\partial}{\partial \psi} + \frac{\partial}{\partial \xi}, \tag{D.6}$$

Figure D.1: Perforated plate with diameter d and pitch p.

$$\frac{\partial}{\partial t} = -\frac{1}{\bar{\rho}_{\mathrm{u}}} \left(\rho u(x,y,t) - \rho u(0,y,t) \right) \frac{\partial}{\partial \psi}$$
$$-\frac{1}{\bar{\rho}_{\mathrm{u}}} \int_0^x \frac{\partial}{\partial y}(\rho v)\,\mathrm{d}x' \frac{\partial}{\partial \psi} + \frac{\partial}{\partial \tau}. \tag{D.7}$$

In short notation, using

$$H = \int_0^x \frac{\partial \rho}{\partial y}\,\mathrm{d}x' \qquad \text{and} \qquad W = \frac{1}{\bar{\rho}_{\mathrm{u}}} \int_0^x \frac{\partial}{\partial y}(\rho v)\,\mathrm{d}x', \tag{D.8}$$

the enthalpy equation (D.1) is written as:

$$\bar{\rho}_{\mathrm{u}} \frac{\partial J}{\partial \tau} + (W + \rho u(0,\xi,\tau)) \frac{\partial J}{\partial \psi} + \rho v \left(H \frac{\partial}{\partial \psi} + \frac{\partial}{\partial \xi} \right) J - \frac{\bar{\lambda}_{\mathrm{u}}}{\bar{c}_p} \frac{\partial^2 J}{\partial \psi^2}$$
$$-\frac{\bar{\rho}_{\mathrm{u}}}{\rho} \frac{1}{\bar{c}_p} \left(H \frac{\partial}{\partial \psi} + \frac{\partial}{\partial \xi} \right) \lambda \left(H \frac{\partial}{\partial \psi} + \frac{\partial}{\partial \xi} \right) J = 0. \tag{D.9}$$

With the assumption that ρ (as well as λ) is constant in the y-direction, v is approximately zero (H, W, and $\partial \bar{J}/\partial y$ are zero), a differential equation for the enthalpy fluctuations can be derived. Linearisation gives:

$$\bar{\rho}_{\mathrm{u}} \frac{\partial J'}{\partial \tau} + \bar{\rho}\bar{u}(0,\xi) \frac{\partial J'}{\partial \psi} - \frac{\bar{\lambda}_{\mathrm{u}}}{\bar{c}_p} \frac{\partial^2 J'}{\partial \psi^2} - \frac{\bar{\lambda}_{\mathrm{u}}}{\bar{c}_p} \frac{\partial^2 J'}{\partial \xi^2} = 0. \tag{D.10}$$

We recognise the one-dimensional enthalpy equation with an additional second-order derivative, which dissipates the enthalpy waves in ξ-direction. By using the periodical nature (period p, where p is the pitch of a slit) of the problem, we construct a solution J' of (D.10), which has the form:

$$J'(\psi,\xi,\tau) = \exp(\omega\tau)\hat{J}(\psi,\xi) = \exp(\omega\tau) \sum_{n=-\infty}^{\infty} \hat{J}_n(\psi) \exp\left(\frac{2\pi n \xi \mathrm{i}}{p} \right), \tag{D.11}$$

or identically,

$$J'(\psi, \xi, \tau) = \exp(\omega\tau) \left[\hat{J}_0(\psi) + 2 \sum_{n=1}^{\infty} \hat{J}_n(\psi) \cos\left(\frac{2\pi n\xi}{p}\right) \right]. \tag{D.12}$$

The easiest way to proceed is using (D.11) to determine the differential equations for each $\hat{J}_n$:

$$\omega\bar{\rho}_{\mathrm{u}}\hat{J}_n + \bar{\rho}\bar{u}(0,\xi)\frac{\partial \hat{J}_n}{\partial \psi} - \frac{\bar{\lambda}_{\mathrm{u}}}{\bar{c}_p}\frac{\partial^2 \hat{J}_n}{\partial \psi^2} + \frac{\bar{\lambda}_{\mathrm{u}}}{\bar{c}_p}\hat{J}_n\left(\frac{2\pi n}{p}\right)^2 = 0, \tag{D.13}$$

These equations need boundary conditions at $\psi = 0$, like in the one-dimensional case. This boundary condition is also a sum of harmonic functions:

$$\hat{J}_{2D}(\xi) = \hat{J}(0,\xi) = \sum_{n=-\infty}^{\infty} \hat{J}_n(0) \exp\left(\frac{2\pi n\xi\mathrm{i}}{p}\right). \tag{D.14}$$

In this model we assume that the mass fraction profile is one-dimensional, so movement of the profile will cause an enthalpy fluctuation at the burner plate. In the true one-dimensional case, these fluctuations will take place where the temperature is fixed. In a slit-burner these effects only take place at the walls, and mainly at the outflow side of the burner plate. We assume that *all* heat is lost through this wall and that the heat that is lost through the wall inside the burner plate is negligible. If the slit has a diameter d, the total amount of heat at the outflow wall is a factor $p/(p-d)$ higher than in the case that the flame could lose its heat over the entire pitch width.

As in the one-dimensional model, the flame position $\psi_{\mathrm{f}}(\tau)$ is related to the enthalpy fluctuations (or temperature fluctuations) at the flame front. The model assumes that fluctuation appears at the outflow side of the burner plate only:

$$\hat{J}_{2\mathrm{D}}(\xi) = \hat{\mathcal{F}}\, 1_{[d/2,p/2]}(\xi), \tag{D.15}$$

with the block function defined as

$$1_{[d/2,p/2]}(\xi) = \begin{cases} 1 & \text{if } \xi \in [d/2, p/2] \\ 0 & \text{elsewhere}, \end{cases} \tag{D.16}$$

and $\hat{\mathcal{F}}$ the Fourier components of a homogeneous boundary condition (is independent on ξ). This is a strong condition, because the heat loss varies over the burner plate.

The integral of $\hat{J}_{2\mathrm{D}}(\xi)$ over the burner plate, in particular in the limit $p \to 0$, results in the one-dimensional boundary condition (which is notated as $\hat{J}_{1\mathrm{D}}$). We must have:

$$\frac{2}{p} \int_0^{p/2} \hat{J}_{2\mathrm{D}}(\xi)\,\mathrm{d}\xi = \frac{2}{p} \int_0^{p/2} \hat{\mathcal{F}}\,\mathrm{d}\xi = \hat{J}_{1\mathrm{D}}. \tag{D.17}$$

This implies that:

$$\hat{\mathcal{F}} = \frac{p}{p-d}\hat{J}_{1D}, \tag{D.18}$$

which means that it is assumed that all heat loss is concentrated on this boundary.
The boundary condition for $\hat{J}$ is written as a sum over the Fourier components $\hat{J}_n(0)$:

$$\hat{J}_{2D}(\xi) = \frac{p-d}{p}\hat{\mathcal{F}} - \frac{2}{\pi}\sum_{n=1}^{\infty}\frac{1}{n}\sin\left(\frac{n\pi d}{p}\right)\cos\left(\frac{2n\pi\xi}{p}\right)\hat{\mathcal{F}}. \tag{D.19}$$

The two-dimensional boundary condition J_{2D} is then determined by considering the movement of the rigid two-dimensional mass fraction profile (it is also assumed to be independent in ξ-direction).
With the boundary conditions and differential equations we construct the solution. For each mode we have:

$$\hat{J}_n(\psi) = \hat{J}_n(0)\exp\left(\frac{\psi}{2\delta}\left\{1 - \sqrt{1 + 4\left[\hat{\omega} + \delta^2\left(\frac{2n\pi}{p}\right)^2\right]}\right\}\right), \tag{D.20}$$

with $\hat{J}_n(0,\xi)$ the terms appearing in (D.19). The total solution reads:

$$\begin{aligned}
\hat{J}(\psi,\xi) = {}&\frac{p-d}{p}\exp\left(\frac{\psi}{2\delta}(1 - \sqrt{1 + 4\hat{\omega}})\right)\hat{\mathcal{F}} \\
&-\frac{2}{\pi}\sum_{n=1}^{\infty}\frac{1}{n}\sin\left(\frac{n\pi d}{p}\right)\cos\left(\frac{2n\pi\xi}{p}\right) \\
&\times\exp\left(\frac{\psi}{2\delta}\left\{1 - \sqrt{1 + 4\left[\hat{\omega} + \delta^2\left(\frac{2n\pi}{p}\right)^2\right]}\right\}\right)\hat{\mathcal{F}}.
\end{aligned} \tag{D.21}$$

From (D.21), we exactly know how the enthalpy fluctuations, induced by the (one-dimensional) mass fraction profile, propagate towards the flame front. The mass fraction is a one-dimensional quantity, so a homogeneous stand-off distance is defined as in a one-dimensional flame. The global fluctuation at the flame front ψ_f' is related to the average flame temperature fluctuations. This is the integral of the enthalpy at $\psi = \bar{\psi}_f$, where $Y = 0$, divided by half the pitch p:

$$\frac{2}{p}\int_0^{p/2}\hat{J}(\bar{\psi}_f,\xi)\,\mathrm{d}\xi = \hat{J}_{1D}, \tag{D.22}$$

which is equal to the result of the one-dimensional case.
The conclusion from this is that under the strict assumptions made, the model indicates that a burner-stabilised flame with half the pitch p and diameter d induces enthalpy fluctuations at the flame front that are a factor $(p-d)/p$ of the one-dimensional case. This

is true for each p, provided that p/d is constant. So perforations have a damping effect in the entire frequency domain.

The diffusive term in the ξ-direction causes the enthalpy to fluctuate at the flame front in the centre of the slit, but with lower amplitudes. The overall fluctuation is determined by integrating over the flame front. This relation is then used to determine the mass burning rate fluctuations and the flame velocity. Integration of (D.21) over the flame front cancels out all higher modes ($n > 0$) terms and we obtain the true one-dimensional enthalpy fluctuation distribution at the flame front again. This result is not dependent on p.

The complete analysis in chapter 5 showed remarkable phase differences between the one- and two-dimensional model. So, apparently some of the assumptions made on the way heat is transferred to the burner are too strong. In future research, the two-dimensional influences need to be analysed further.

Bibliography

[1] R. Bird, W. Steward, and E. Lightfoot. *Transport phenomena*. John Wiley & Sons, New York, 1960.

[2] H. Bosscha and P. Riesse. *Pogg Ann Phys Chem*, 108:653, 1859.

[3] P. Bouma. *Methane-Air Combustion on Ceramic Foam Surface Burners*. PhD thesis, Eindhoven University of Technology, 1997.

[4] J. Buckmaster and G. Ludford. *Theory of Laminar Flames*. Cambridge Univ. Press, 1982.

[5] S. Candel and T. Poinsot. Interactions between acoustics and combustion. *Proceedings of the Institute of Acoustics*, 10:103–153, 1988.

[6] J. Clark and A. McIntosh. The influence of a flameholder on a plane flame, including its static stability. *Proc R Soc Lond*, 372:367–392, 1980.

[7] F. Culick. Combustion instabilities in liquid-fueled propulsion system, an overview. *AGARD-CP-450*, 1988.

[8] L. de Goey, L. Somers, W. Bosch, and R. Mallens. Modeling of the small scale structure of flat burner-stabilized flames. *Comb Sci and Tech*, 104:387–400, 1995.

[9] L. de Goey and J. ten Thije Boonkkamp. A mass-based definition of flame stretch for flames with finite thickness. *Comb Sci Tech*, 122:399–405, 1997.

[10] L. de Goey and J. ten Thije Boonkkamp. A flamelet description of premixed laminar flames and the relation with flase stretch. *Comb Flame*, 119:253–271, 1999.

[11] R. de Lange. *Modeling of Premixed Laminar Flames*. PhD thesis, Eindhoven University of Technology, 1992.

[12] C. Dieteren. Response of axisymmetric laminar premixed flames to an acoustic field. Master's thesis, Eindhoven University of Technology, 1997.

[13] G. Dixon-Lewis. Flame structure and flame reaction kinetics ii. transport phenomena in multi component systems. *Proc Roy Soc Am*, 307:111, 1968.

[14] A. Dowling. The calculation of thermo-acoustic oscillations. *Journal of Sound and Vibration*, 180:557–581, 1995.

[15] ed. M.D. Smooke. Reduced kinetic mechanisms and asymptotic approximations. *Lecture notes in Physics*, 1991.

[16] F. Egolfopoulos, D. Zhu, and C. Law. Experimental and numerical determination of laminar flame speeds: Mixtures of C_2-hydrocarbons with oxygen and nitrogen. *Twenty-Third Symposium (International) on Combustion*, page 471, 1990.

[17] M. Fleifil, A. Annaswamy, Z. Ghoneim, and A. Ghoniem. Response of a laminar premixed flame to flow oscillations. *Comb Flame*, 106:487–510, 1996.

[18] M. Ghilani and B. Larrouturou. Upwind computation of steady planar flames with complex chemistry. *Mathematical Modelling and Numerical Analysis*, 25:67, 1991.

[19] T. Gielen. PhD thesis, Eindhoven University of Technology, 2001.

[20] G. Groot. The acoustic response of two-dimensional laminar flames. Master's thesis, Eindhoven University of Technology, 1999.

[21] G. Hedstrom. Nonreflecting boundary conditions for nonlinear hyperbolic systems. *J Comp Physics*, 30:222–237, 1979.

[22] B. Higgins. *J Natural Phil Chem Arts*, 1:129, 1802.

[23] J. Hirschfelder, C. Curtis, and R. Bird. Molecular theory of gases and liquids. *Advances in Reactor Computations*, page 24, 1983.

[24] W. Hoffmans. Akoestische overdrachtsmatrix van een vlam uitgaande van een generiek model voor de vlamresponsie. *TNO-rapport TU Delft*, TPD-HAG-RPT-970169, 1998.

[25] R. Issa. Solution of the implicitly discretized fluid flow equations by operator-splitting. *J Comp Phys*, 62:40–65, 1985.

[26] W. Kaskan. The dependence of flame temperature on mass burning velocity. *6th (Int) Symposium on Combustion*, pages 134–143, 1956.

[27] J. Keller. Thermoacoustic oscillations in combustion chambers of gas turbines. *AIAA J*, 33:2280–2287, 1995.

[28] H. Kreiss and J. Lorenz. *Initial-Boundary Value Problems and the Navier-Stokes Equations*. Academic Press, 1989.

[29] G. Laufer. *Introduction to Optics and Lasers in Engineering*. Cambridge University Press, Cambridge, 1996.

[30] R. Mallens. *Stabilisation of Laminar Premixed Methane/Air Flames.* PhD thesis, Eindhoven University of Technology, 1996.

[31] A. McIntosh. On the coupling of an anchored flame with an acoustic field. *Proceedings of the Institute of Acoustics*, 6:277–298, 1984.

[32] A. McIntosh. On the cellular instability of flames near porous-plug burners. *J Fluid Mech*, 61:43–75, 1985.

[33] A. McIntosh. The effect of upstream acoustic forcing and feedback on the stability and resonance behaviour of anchored flames. *Comb Sc Tech*, 49:143–167, 1986.

[34] A. McIntosh. Combustion-acoustic interaction of a flat flame burner system enclosed within an open tube. *Comb Sci Tech*, 54:217–236, 1987.

[35] A. McIntosh. On flame resonances in tubes. *Comb Sc Tech*, 69:147–152, 1990.

[36] A. McIntosh. Some comments on the rayleigh creterion for combustion associated acoustic resonance. In *Proceedings of the Joint meeting of the British and German sections of the Combustion Institute*, pages 323–326, 1993.

[37] A. McIntosh. A model of heat transfer in rijke tube burners. *Comb Sc Tech*, 113-114:273–289, 1996.

[38] A. McIntosh and J. Clark. Resonant response of a flat flame near a flame-holder. *Flames, Lasers and Reactive Sytems: AIAA Progress in Astroacoustics and Aeronautics*, 88:3–37, 1982.

[39] A. McIntosh and J. Clark. Second order theory of unsteady burner-anchored flames with arbitrary lewis number. *Comb Sci Techn*, 38:161–196, 1984.

[40] J. Mohamed and J. Walsh. *Numerical algorithms.* Clarendon, Oxford, 1986.

[41] M. Munjal. *Acoustics of Ducts and Mufflers.* John Wiley & Sons, Inc., New York, 1987.

[42] A. Putnam. *Combustion-driven oscillations in Industry.* Amarican Elsevier Publishing Company, New York, 1971.

[43] A. Putnam and W. Dennis. Burner oscillations of the gauze-tone type. *J Acoust Soc Am*, 29:716–725, 1954.

[44] R. Raun, M. Beckstead, J. Finlinson, and K. Brooks. A review of rijke tube burners and related devices. *Prog Energy Combust Sci*, 19:313–364, 1987.

[45] J. L. Rayleigh. *Nature*, 18:319, 1878.

[46] M. Remie. Stabiliteitsanalyse van een cv-ketel voor lage gassnelheden. Technical report, University of Technology Eindhoven, faculty Mechanical Engineering, 2001.

[47] P. Rijke. *Phil Mag*, 17:419, 1859.

[48] Y. Saad. *Iterative methods for sparse linear systems*. PWS Publishing Company, 1995.

[49] H. Schimmer and D. Vortmeyer. Acoustic oscillation in a combustion system with a flat flame. *Comb Flame*, 28:17–24, 1977.

[50] H. Schlichting. *Boundary-layer Theory*. McGraw-Hill Book Company, Inc., New York, sixth edition, 1968.

[51] K. Schreel, R. Rook, and L. de Goey. The acoustic response of a burner-stabilized flat burner. In *Eurotherm Seminars Proceedings*, volume 67, pages 2167–2177, 2000.

[52] L. Somers. *The Simulation of Flat Flames with Detailed and Reduced Chemical Methods*. PhD thesis, Eindhoven University of Technology, 1994.

[53] C. Sondhauss. *Pogg Ann Phys Chem*, 79:1, 1850.

[54] G. Thiart. Finit difference scheme for the numerical solutions of fluid flow and heat transfer problems on non-staggered grids. *Numerical heat transfer, part B*, 17:81, 1990.

[55] K. Thompson. Time dependent boundary conditions for hyperbolic systems. *J Comp Physics*, 68:1–24, 1987.

[56] M. van Dyke. *Perturbation methods in fluid mechanics*. Parabolic Press, 1975.

[57] A. van Maaren. *One-step chemical reaction parameters for premixed laminar flames*. PhD thesis, Eindhoven University of Technology, 1994.

[58] B. van 't Hof. *Numerical Aspects of Laminar Flame Simulations*. PhD thesis, Eindhoven University of Technology, 1998.

[59] F. Williams. *Combustion Theory*. Addison-Wesley Publishing Company, Redwood city, second edition, 1985.

[60] E. Zauderer. *Partial Differential Equations of Applied Mathematics*. Wiley-Interscience, 1983.

Summary

Central heating devices are equipped with modulating burners. These devices are sometimes unstable and give rise to noise problems. In order to predict instabilities, TNO-TPD developed a tool based on the transfer matrix method wherein the acoustic system is one-dimensional and divided into acoustic elements. Each element couples the pressure and velocity fluctuations on both sides. In this thesis, the element for the burner/flame is investigated numerically and theoretically. The burner is a perforated plate, which can be looked upon as a one-dimensional configuration if the diameter of the perforations is small enough. An important question is how small the diameter must be to guarantee this.

In chapter 1, an introduction to thermoacoustics is given. For example, the Rijke tube is a well-known configuration, where heat is added to the gas by a heated gauze. If this gauze is placed in the lower half of the vertical tube, the sound is sustained. This phenomenon is explained by the memory effect of the boundary layers at the gauze. The Rayleigh-criterion states that a phase shift exists between the pressure and heat transfer in such a way that acoustic energy is added to the field. A burner-stabilised flame shows similar phenomena as the heated gauze. In a flame heat is released by the chemical reaction, but heat is lost to the burner. There exists a phase difference between the net heat and the pressure fluctuations via mass flow variations. Also flame resonance may occur in the burner/flame. Under circumstances, the flame amplifies sound waves up to levels above the normal gas expansion factor, due to the temperature difference.

In chapter 2, the governing equations are presented. This model describes reacting flows by transport equations and thermodynamic relations. These equations are simplified by the low-Mach number Combustion Approximation. Also, the burner-plate configuration is defined, together with an approximation of the flow through a porous burner. The acoustics in the central heating device can be described by the one-dimensional wave equation. This equation is the basis of the transfer matrix method, which is explained at the end of chapter 2.

Chapter 3 describes the numerical method. Due to the Combustion Approximation, the density can be eliminated from the system, which yields an expansion equation. Numerically, this equation cannot be solved easily. A pressure correction method is applied to the set of discretised equations. To solve this set efficiently, multi-grid, time-extrapolations and Broyden iteration methods are implemented. In principle, one method suffices for the one- and two-dimensional simulations, but in the one-dimensional case, the iteration matrix is tri-diagonal and the pressure is uncoupled completely, which means that the equations can

be solved very efficiently by using an essentially different method.

In chapter 4, phenomena like flame resonance are explained by an analytical model. The basis of this model is that the motion of the flame, e.g. the mass fraction profile, is described by the G-equation. The flame is assumed rigid and moves with a flame velocity, which is the difference between the gas velocity and the mass burning velocity. When the flame moves, the enthalpy fluctuations emerge at the burner plate. These fluctuations propagate towards the flame, which result in temperature fluctuations at the flame front. Here, the fluctuations influence the amount of fuel being burnt, because the mass burning rate is directly coupled to the temperature via the Zeldovich number. If a phase difference between the enthalpy fluctuations and the flame velocity exists the movement might amplify itself, causing flame resonance. This movement can also occur spontaneously, which is called flame instability. Both the response on fluctuating mass flow and spontaneous oscillations are investigated.

Chapter 5 is a numerical analysis of the two-dimensional flat flames. The diameter of the perforations in the plate is an important parameter. The limit of the diameter to zero is believed to render the one-dimensional acoustic response of burner-stabilised flames, which is shown in this chapter. Below a certain diameter, geometrically, the flame can be considered as flat. However acoustically, a damping effect can be observed indirectly. The resonance peak found in the one-dimensional simulations are higher than in the two-dimensional case. The gas inside the burner cannot be cooled ideally, so the flame stabilises closer to the burner. However, this does not explain all observed differences. The lower resonance peak is probably related to the lower magnitude of the enthalpy fluctuations at the perforated plate. From time dependent simulations it is shown that enthalpy fluctuations are highest at the centre of the plate segments. The fluctuations at the walls inside the burner do not contribute to the total enthalpy fluctuations. When the diameter decreases, all heat at the centre of the flow can be transferred more easily and the maximum distance of the flame front to the walls of the burner becomes smaller.

In chapter 6, the response of the burner/flame on acoustic fluctuations is used to determine the stability of a simplified heating device. The influence of burner surface temperature on the acoustic behaviour is investigated. Many noise problems in practical burners occur at start-up, when the burner is cold, and disappear when normal burner surface temperatures are reached. However, the results show that the simplified system do not resolve the observed problems occurring in real central heating systems. Our analysis confirms the important role of burner surface temperature in the acoustic behaviour of the heating device, but should be investigated further at different systems before recommendations for practical burner design can be made.

Samenvatting

Centrale verwarmingsketels zijn vervaardigd met traploos instelbare branders. In sommige gevallen zijn deze systemen instabiel en kunnen geluidsproblemen optreden. Om deze instabiliteiten te voorspellen heeft TNO-TPD een computer programma ontwikkeld dat gebaseerd is op de overdrachtsmatrixmethode. In dit model wordt de akoestiek als eendimensionaal beschouwd en het systeem wordt verdeeld in akoestische elementen. Elk element koppelt de druk- en snelheidsfluctuaties aan beide uiteinden. In dit proefschrift wordt het element voor de brander/vlam theoretisch en numeriek onderzocht. De brander is een geperforeerde plaat die als een eendimensionale configuratie beschouwd mag worden als de diameter van de perforaties klein genoeg zijn. Het is belangrijk te weten hoe klein de diameter moet zijn.

In hoofdstuk 1 wordt er een inleiding gegeven over thermo-akoestiek. Als voorbeeld wordt de Rijke-buis genoemd. In deze buis wordt warmte afgegeven aan het gas door een verwarmd gaasje. Als dit gaasje op een kwart aan de onderkant van de de buis wordt geplaatst, zal er een aanhoudende toon hoorbaar zijn. Dit fenomeen wordt uitgelegd aan de hand van een geheugen effect van de grenslagen in de stroming door het gaasje. Het Rayleigh-criterium zegt dat er een bepaalde fasedraaiing tussen de druk en de warmteafgifte bestaat, zodanig dat akoestische energie toegevoegd wordt aan het gas. Voor een brander/vlam in een buis vertoont een vergelijkbare akoestisch gedrag. In een vlam wordt het gas opgewarmd door verbranding en gekoeld door warmteverlies aan de brander. Onder bepaalde omstandigheden versterkt de vlam geluid bovenop de normale gas expansie door temperatuursverschillen.

In hoofdstuk 2 wordt het theoretische model gepresenteerd. Dit model beschrijft het reagerende mengsel met transportvergelijkingen en thermo-dynamische relaties. Deze vergelijkingen kunnen worden vereenvoudigd door gebruik te maken van het lage Mach getal. Hier wordt tevens de geometrie van de poreuze brander en de stroming door deze brander beschreven. De akoestiek wordt beschreven door de eendimensionale golfvergelijking. Deze vergelijking is de basis van de overdrachtmatrixmethode die uitgelegd wordt aan het eind van dit hoofdstuk.

Hoofdstuk 3 beschrijft het numerieke model. Door de lage-Machgetal benadering kan de dichtheid geëlimineerd worden en de continuïteitsvergelijking wordt een expansievergelijking. Numeriek kan deze vergelijking niet eenvoudig opgelost worden. Een drukcorrectiemethode wordt toegepast op de vergelijkingen en onder andere een multi-grid methode helpt bij het iteratief oplossen ervan. In principe kan één code ontwikkeld worden om

een- en meerdimensionale problemen op te lossen, maar door gebruik te maken van de tri-diagonale iteratie matrix en ontkoppeling van de druk kan het eendimensionale probleem op een andere manier zeer efficiënt opgelost worden.

In hoofdstuk 4 worden fenomenen, zoals resonantie, uitgelegd aan de hand van een theoretisch model. De basis van dit model is dat de beweging van de vlam, in het bijzonder het massafractie profiel, beschreven wordt door de G-vergelijking. Er wordt verondersteld dat de vlam star beweegt. Wanneer de vlam beweegt ontstaan enthalpiefluctuaties aan de uitlaat van de brander. Deze fluctuaties verplaatsen zich naar de vlam, welke temperatuurfluctuaties veroorzaken in het vlamfront. Hier beïnvloeden de fluctuaties de verbranding. Als er een fasedraaiing bestaat tussen de enthalpiegolven en de vlamsnelheid, dan is het mogelijk dat de vlam deze beweging versterkt en vlamresonantie veroorzaakt. Deze versterkte vlambewegingen kunnen ook spontaan optreden, dat vlaminstabiliteit wordt genoemd. Resonantie en vlaminstabiliteiten worden aan de hand van het model onderzocht.

Hoofdstuk 5 is een numerieke analyse van tweedimensionale vlakke vlammen. De diameter van de perforaties in de branderplaat is een belangrijke parameter. Onderzocht moet worden of de limiet van de diameter naar nul de eendimensionale brander-gestabiliseerde vlammen vertaalt. De stationaire limiet is al onderzocht en dat dit ook geldt voor het akoestisch gedrag wordt in dit hoofdstuk aangetoond. Het blijkt dat de stationaire vlakke vlam eerder als eendimensionaal opgevat wordt in vergelijking tot het akoestische gedrag, dat een demping vertoont in de vlamresonantie. Het verschil met de eendimensionale vlam is dat het gas niet ideaal gekoeld kan worden, zodat de vlam dichterbij de brander stabiliseert. Echter, dit verklaart niet alle verschillen. De afgezwakte resonantie moet gezocht worden in een gemiddeld kleinere amplitude van de enthalpiefluctuaties op de branderplaat. Uit tijdsafhankelijke simulaties is gebleken dat de fluctuaties op hun hoogst zijn in het midden van de plaatsegmenten en de fluctuaties die ontstaan op de wanden binnen in de plaat geven een verwaarloosbare bijdrage aan het totaal. Naarmate de diameter kleiner wordt kan de vlam beter zijn warmte afstaat aan de brander omdat de gemiddelde afstand van de vlam naar de brander kleiner wordt.

Tot slot, in hoofdstuk 6 wordt de responsie van de brander/vlam gebruikt om de stabiliteit van een sterk vereenvoudigd systeem te bepalen. De oppervlaktetemperatuur wordt onderzocht op zijn invloed op het akoestisch gedrag van het systeem. Het opwarmen van een ketel bij een koude start geeft in ketels geluidsproblemen, die verdwijnen als de brander op temperatuur komt. Echter, de resultaten geven aan dat het vereenvoudigde systeem niet dit gedrag vertoont.

Nawoord

Bijna vier en half jaar werk staat in dit boekje beschreven. Dit kon ik natuurlijk niet alleen en ik wil hierbij graag iedereen bedanken die een bijdrage heeft geleverd.

Ten eerste Philip de Goey, zijn gedrevenheid en goede ideeën, die geleid hebben tot het analytische model en het fysische inzicht. Hij was de opvolger van Bart Somers, die mij in aanraking liet komen met chem1D, waaraan ik met alle plezier gesleuteld heb. Ten tweede mijn kamergenoten Karel en Jeroen, buren Gemmeke en Happy en alle koffie- en theedrinkers van de afdeling voor de nodige afleiding en aanspreekpunten. En Koen, voor de experimenten die hij gedaan heeft.

Verder wil ik René Parchen van TNO-TPD bedanken voor zijn inbreng in het akoestische gedeelte van mijn proefschrift en het tot stand komen van de 'stage' in Delft.

Als laatste wil ik Mirjam bedanken voor haar steun tijdens de laatste loodjes.

Stellingen

behorende bij het proefschrift

Acoustics in Burner-Stabilised Flames

van

Ronald Rook

1. Brander-gestabiliseerde vlammen vertonen een resonerend gedrag als er een fasedraaiing van $\frac{1}{2}\pi$ bestaat tussen fluctuaties in de vlamtemperatuur en het warmteverlies naar de brander.

   Dit proefschrift.

2. Akoestisch gezien kunnen plaatbranders met voldoende kleine perforaties als eendimensionale branders gemodelleerd worden.

   Dit proefschrift.

3. Een globale beschrijving van de chemie in een brander-gestabiliseerde vlam is voldoende om het fenomeen vlamresonantie te voorspellen.

   Dit proefschrift.

4. Grote breinen zijn (net als grote regeringen) niet in staat simpele dingen op een simpele manier te doen.

   Donald Hebb (1958)

5. Het is niet mogelijk onderscheid te maken tussen handelen met voorkennis en het hebben van goed inzicht in het bedrijfseconomisch handelen.

6. Net als bewustzijn komt taal uitsluitend voort uit de behoefte en de noodzaak van omgang met andere mensen.

7. Met het aanbieden van ruimtereisjes steken de Russen de Amerikanen naar de kroon op het gebied van commercialisering.

8. Daar de genotsbeleving zich meer aan ons opdringt dan geluksbeleving, hebben we vooral in geval van genot de neiging om ons af te vragen of het misschien 'wat meer' zou kunnen zijn. Deze neiging vernietigt uiteindelijk ons vermogen om van wat ook maar te genieten.

   Henk Vos (1996)

9. Het relativerend vermogen van een perfectionist is nihil.

10. Demonstranten die aanwezig zijn bij de Eurotoppen zijn voetbalsupporters zonder clubpas.